SAPIENZA
UNIVERSITÀ DI ROMA

Facoltà di Scienze Matematiche, Fisiche e Naturali

Scuola di dottorato "Vito Volterra" in Scienze della Terra

XXXI ciclo

Integrating seismological data, DInSAR measurements and numerical modelling to analyse seismic events: the M_w 6.5 Norcia earthquake case-study

Ph.D. Student:

Emanuela Valerio

Tutor:

Prof. Carlo Doglioni

Co-tutor:

Prof. Eugenio Carminati

2018

Niente nella vita va temuto, dev'essere solamente compreso.
Ora è tempo di comprendere di più, così possiamo temere di meno.

Marie Curie

Table of contents

List of Figures

List of Tables

Abstract

This Ph.D. thesis is focused on the detailed analysis of seismic sequences and on the application of a multidisciplinary approach based on the integration of several geophysical and geodetic techniques. In the context of a more general study of seismic sequences, we focus this work on the analysis and comparison of five extensional and five compressional seismic sequences to understand the differences between these two tectonic settings in terms of aftershocks duration. In fact, aftershocks number decay through time, depending on several parameters peculiar to each seismogenic regions, including mainshock magnitude, crustal rheology, and stress changes along the fault. However, the exact role of these parameters in controlling the duration of the aftershock sequence is still unknown. Here, by using two methodologies, we show that the tectonic setting primarily controls the duration of aftershocks. On average and for a given mainshock magnitude, (i) aftershock sequences are longer and (ii) the number of earthquakes is greater in extensional than in compressional tectonic settings. We suggest as possible explanation that this difference can be related to the different type of energy dissipated during earthquakes; in detail, (i) a joint effect of gravitational forces and pure elastic stress release governs extensional earthquakes, whereas (ii) pure elastic stress release controls compressional earthquakes. Accordingly, normal faults operate in favour of gravity, preserving inertia for a longer period and seismicity lasts until gravitational equilibrium is reached. Vice versa, thrusts act against gravity, exhaust their inertia faster and the elastic energy dissipation is buffered by the gravitational force. Hence, for seismic sequences of comparable magnitude and rheological parameters, aftershocks last longer in extensional settings because gravity favours the collapse of the hangingwall volumes. The occurrence of the 2016 Central Italy seismic sequence furnishes a test-bed for a detailed analysis of a normal fault earthquake. Therefore, we analyse also the M_w 6.5 Norcia (Central Italy) earthquake to add another extensional seismic sequence to the previously examined case-studies. The results of this analysis show that, with respect to the other considered extensional seismic sequences, also the M_w 6.5 Norcia seismic sequence present the same behaviour about the aftershocks temporal and spatial evolution. Moreover, we decide to take into account the M_w 6.5 Norcia mainshock as case-study

for the application of a multidisciplinary approach, in order to understand the kinematics and the role of gravity during nucleation processes of extensional events. In particular, we investigate the M_w 6.5 Norcia earthquake by exploiting seismological data, DInSAR measurements and a numerical modelling approach. In particular, we first take into consideration the relocated hypocentres with $0.1 \leq M_w \leq 6.5$ that occurred between August 24th and November 29th, 2016, recorded by the INGV seismometric network; the projection onto sections and the subsequent analysis of the considered hypocentres allow us to identify the geological structures that were involved during earthquake nucleation process. Then, we retrieve the vertical component (uplift and subsidence) of the displacements affecting the hangingwall and the footwall blocks of the seismogenic faults identified, at depth, through the hypocentres distribution analysis; to do this, we combine the DInSAR measurements obtained from coseismic SAR data pairs collected by the ALOS-2 sensor from ascending and descending orbits. The achieved vertical deformation map displays three main deformation patterns: (i) a major subsidence that reaches the maximum value of about 98 cm near the epicentral zones nearby the town of Norcia; (ii) two smaller uplift lobes that affect both the hangingwall (reaching maximum values of about 14 cm) and the footwall blocks (reaching maximum values of about 10 cm). Also GPS measurements were used to compare the displacements recorded next to the epicentral area. Starting from this evidence, we compute the rock volumes affected by uplift and subsidence phenomena, highlighting that those involved by the retrieved subsidence are characterized by significantly higher deformation values than those affected by uplift (about 14 times). In order to provide a possible interpretation of this volumetric asymmetry, we extend the analysis by running a 2D numerical model based on the finite element method, implemented in a structural-mechanic framework and exploiting the available geological and seismological data. Modelling results are compared with the ground deformation measurements retrieved from the multi-orbit ALOS-2 DInSAR analysis. In the modelling approach, we test the effects of different geometries, by considering two different scenarios: the first is based on including only a single SW-dipping fault, the second includes a main SW-dipping fault and an antithetic zone. In this context, the model characterized by the occurrence of an antithetic zone presents the retrieved best fit coseismic surface deformation pattern. This result allows us to interpret the subsidence

and uplift phenomena caused by the M_w 6.5 Norcia earthquake as the result of the gravitational sliding of the hangingwall along the main fault plane and of the frictional force acting in the opposite direction, consistently with the double couple fault plane mechanism.

Riassunto

Questa tesi di dottorato è incentrata sull'analisi dettagliata di sequenze sismiche e sull'applicazione di un approccio multidisciplinare basato sull'integrazione di diverse tecniche geofisiche e geodetiche. Nel contesto di uno studio più generale delle sequenze sismiche, abbiamo concentrato il lavoro sull'analisi ed il confronto di dieci sequenze sismiche (cinque estensionali e cinque compressive), al fine di comprendere le differenze tra questi due ambienti tettonici in termini di durata degli aftershocks. Infatti, il numero di aftershocks decade nel tempo in funzione di vari parametri che risultano essere peculiari di ogni area sismogenetica; tra questi si possono annoverare la magnitudo del mainshock, la reologia crostale e le variazioni dello stress lungo la faglia. Tuttavia, il ruolo esatto svolto da questi parametri nel controllo della durata delle sequenze di aftershocks non è ancora noto. Utilizzando due diverse metodologie, abbiamo evidenziato che l'ambiente tettonico gioca un ruolo primario nell'influenzare la durata degli aftershocks. In media e per una data magnitudo del mainshock, (i) le sequenze di aftershocks sono più lunghe e (ii) il numero di terremoti è maggiore negli ambienti tettonici estensionali rispetto a quelli compressivi. Una possibile spiegazione consiste nel fatto che questa differenza possa essere correlata al diverso tipo di energia dissipata durante i terremoti; in dettaglio, (i) un effetto congiunto di forza gravitazionale e di energia elastica governerebbe i terremoti estensionali, mentre (ii) il rilascio di pura energia elastica controllerebbe i terremoti compressivi. Infatti, le faglie normali operano a favore della gravità, preservando così l'inerzia per un periodo più lungo, e la sismicità dura fino a quando l'equilibrio gravitazionale non viene nuovamente raggiunto dal sistema. Viceversa, i thrusts agiscono contro la gravità, esauriscono la loro inerzia più velocemente e la dissipazione di energia elastica viene controbilanciata dalla forza gravitazionale. Quindi, per sequenze sismiche con magnitudo e parametri reologici paragonabili, gli aftershocks durano più a lungo negli ambienti estensionali poiché la gravità favorisce il collasso dei volumi di hangingwall. Il verificarsi della sequenza sismica del Centro Italia nel 2016 ha fornito un banco di prova per un'analisi dettagliata di un altro terremoto estensionale. Per questo motivo, abbiamo analizzato il terremoto di Norcia (M_w 6.5; Italia Centrale) per aggiungere un'altra sequenza sismica estensionale ai casi

di studio precedentemente esaminati. I risultati di questa analisi mostrano che anche la sequenza sismica di Norcia presenta lo stesso comportamento delle altre sequenze estensionali in termini di evoluzione temporale e spaziale degli aftershocks. Inoltre, abbiamo deciso di prendere in considerazione il terremoto di Norcia come caso di studio per l'applicazione di un approccio multidisciplinare, al fine di cercare di comprendere la possibile cinematica e il ruolo della gravità durante i processi di enucleazione degli eventi estensionali. In particolare, abbiamo investigato il terremoto di Norcia, ricorrendo all'utilizzo di dati sismologici, di misure DInSAR e della modellazione numerica. In particolare, abbiamo prima di tutto preso in considerazione gli ipocentri rilocalizzati con $0.1 \leq M_w \leq 6.5$, verificatisi tra il 24 agosto e il 29 novembre 2016 e registrati dalla rete sismometrica INGV; la proiezione su sezioni e la successiva analisi degli ipocentri considerati hanno consentito di comprendere quali strutture geologiche siano state coinvolte durante il processo di enucleazione del terremoto. In seguito, abbiamo analizzato la componente verticale (sollevamento e subsidenza) dei displacements che hanno interessato i blocchi di hangingwall e di footwall della faglia sismogenetica, precedentemente identificata in profondità mediante l'analisi della distribuzione ipocentrale; per fare ciò, abbiamo utilizzato le misure DInSAR ottenute dalla combinazione delle coppie di dati SAR cosismici acquisite dal sensore ALOS-2 lungo orbite ascendenti e discendenti. La mappa di deformazione verticale ottenuta mostra tre aree di deformazione principali: (i) una maggiore subsidenza che raggiunge il valore massimo di circa 98 cm in prossimità delle zone epicentrali vicine alla città di Norcia; (ii) due piccoli lobi di sollevamento che interessano sia il blocco di hangingwall (dove raggiunge valori massimi di circa 14 cm) sia quello di footwall (dove raggiunge valori massimi di circa 10 cm). Partendo da queste evidenze, abbiamo calcolato i volumi di roccia interessati dai fenomeni di sollevamento e subsidenza, evidenziando che quelli coinvolti dal fenomeno di subsidenza sono caratterizzati da valori di deformazione significativamente più alti di quelli affetti da sollevamento (circa 14 volte). Al fine di fornire una possibile interpretazione di questa asimmetria volumetrica, abbiamo esteso l'analisi elaborando un modello numerico 2D basato sul metodo degli elementi finiti, implementandolo in un quadro strutturale-meccanico e sfruttando i dati geologici e sismologici disponibili. I risultati della modellazione sono stati poi confrontati con le misure della deformazione del suolo ottenute dall'analisi DInSAR. Nel corso della

realizzazione del modello numerico, abbiamo collaudato gli effetti di geometrie diverse, considerando in particolare due scenari: il primo si basa su una singola faglia immergente a sud-ovest, il secondo su una faglia principale immergente a sud-ovest e una fascia antitetica. In questo contesto, il modello caratterizzato dalla presenza della fascia antitetica fornisce il miglior fit quando confrontato con il pattern cosismico di deformazione superficiale. Questo risultato consente di interpretare i fenomeni di subsidenza e sollevamento causati dal terremoto di Norcia come il risultato di un collasso gravitazionale del blocco di hangigwall lungo la faglia principale e della forza frizionale che agisce in direzione opposta, consistentemente con il meccanismo di doppia coppia lungo il piano di faglia.

Chapter 1

Introduction

Earthquakes are a mechanism accommodating large-scale motion of the Earth's plates; most of them are associated with activities on faults and the strongest events typically occur at plate boundaries (i.e., subduction zones and areas of continental collision; Stein and Wysession, 2009). However, large events also occur in plate interiors but with a much lower frequency (Turcotte and Schubert, 2014). During an earthquake, slip on the fault generates seismic waves and causes ground motions in a very short time period (i.e., within seconds to minutes).

Earthquakes are part of a process known as *seismic cycle*, which describes the crustal deformation of a fault zone in four different periods: *interseismic*, *preseismic*, *coseismic* and *postseismic* (Scholz, 2002). During the interseismic stage, which describes the long-term crustal movement between seismic events along the same fault, steady motion occurs away from the fault but the fault itself is locked, although some aseismic creep can possibly occur on it. Immediately prior to rupture, there is the preseismic stage that can be associated with small earthquakes (foreshocks) or other possible precursory phenomena. The earthquake (or mainshock) itself marks the coseismic phase, during which rapid motion on the fault generates seismic waves. The coseismic displacement refers to the deformation during an earthquake event within seconds to minutes, depending on the size of the earthquake; the amount and the spatial distribution of coseismic deformation relay on the magnitude and depth of the event as well as the geologic setting of the area. Finally, a postseismic phase occurs after the earthquake; the postseismic displacement refers to the deformation process after an earthquake until it falls back to the background level as before the earthquake (e.g., Lay and Wallace, 1995). During this phase, aftershocks, generally characterized by magnitudes smaller than the mainshock (the total energy released by the aftershocks is usually less than 10% of that of the mainshock; Lay and Wallace, 1995), nucleate for months to years until the fault settles into its interseismic behaviour again, allowing the release of the remaining seismic energy (Savage, 1983). Their

occurrence rate decreases with time, typically following a pattern known as the Omori's law, named for Fusakichi Omori's observation of the 1891 Nobi earthquake in Japan (Omori, 1894) and later modified by Utsu (1961):

$$n(t) = \frac{k}{(c+t)^p} \quad (1.1)$$

where $n(t)$ is the number of aftershocks by time t after the mainshock; k, c and p are constants. The value of c is typically positive close to zero, and p close to 1. Hence, the number of aftershocks drops nearly hyperbolically with time (Figure 1.1). The values of these constants are obtained by fitting to the data for each aftershock sequence. It has been observed that the largest aftershock is usually about 1 magnitude unit smaller than the mainshock, independent of the mainshock magnitude. This is known as Bath's law (Bath, 1965; Richter, 1958). However, because the data selection is retrospective and subjective, the size of aftershocks can vary substantially for different earthquake sequences.

Like all earthquakes, the size distribution of aftershocks follows the Gutenberg–Richter law (Gutenberg and Richter, 1954):

$$logN(M) = a - bM \quad (1.2)$$

where $N(M)$ is the number of earthquakes of magnitude $\geq M$, a and b are constants. This relationship plots as a straight line with slope b, whose value, often referred to as the *b*-value, is typically in the range of 0.8–1.2. For $b = 1$, the number of earthquakes increases by a factor of 10 for every unit drop. The *b*-value varies in time and space even for the same fault. Some studies have suggested that the *b*-values can be used as a stress indicator, with lower *b*-values often associated with higher stresses (Schorlemmer et al., 2005).

Because most aftershocks occur on or near the rupture surface, they are thought to result from incomplete rupture and heterogeneous slip (e.g., Bullen and Bolt, 1947). Most of the aftershocks occur on or near the mainshock fault plane, so their locations are used to distinguish between the fault and auxiliary planes and to estimate the fault area (Stein and Wysession, 2009); they nucleate soon after the mainshock and decay with time in a quasi-hyperbolic manner. The decay of aftershocks typically obeys the Omori-

Utsu law (Omori, 1894; Utsu, 1961; Figure 1.1), reflecting stress readjustment that follows the stress changes due to the mainshock.

This notion is consistent with some case studies that found aftershocks concentrated around the perimeter of the rupture zone or around asperities within the rupture zone where most of the coseismic slip occurred (Beroza, 1991; Scholz, 2002). The main causes of aftershocks are thought to include mainshock-induced changes of frictional properties of the fault zone and stress perturbations. Laboratory experiments indicate that frictional properties change with the duration of stationary contact and the instantaneous sliding velocity (Scholz, 2002). A constitutive relationship based on such results, known as the rate-and-state law (Dieterich, 1979; Ruina, 1983), can explain the time-dependent changes of seismic rates that are consistent with the Omori's law (Dieterich, 1994). Stress perturbations may arise from creep recovery of rocks in the immediate areas of the fault (Benioff, 1951), viscous relaxation from the lower crustal and upper mantle (Lieber and Braslau, 1965; Stein and Liu, 2009), and pore-elastic effects (Scholz, 2002). In particular, the changes of the Coulomb static stress resulted from the mainshock have been shown to cause spatial migration of seismicity and trigger earthquakes (Parsons, 2002; Stein, 1999). Other causes may include dynamic triggering (Gomberg and Johnson, 2005) and pore fluid flow (Miller et al., 2004; Nur and Booker, 1972).

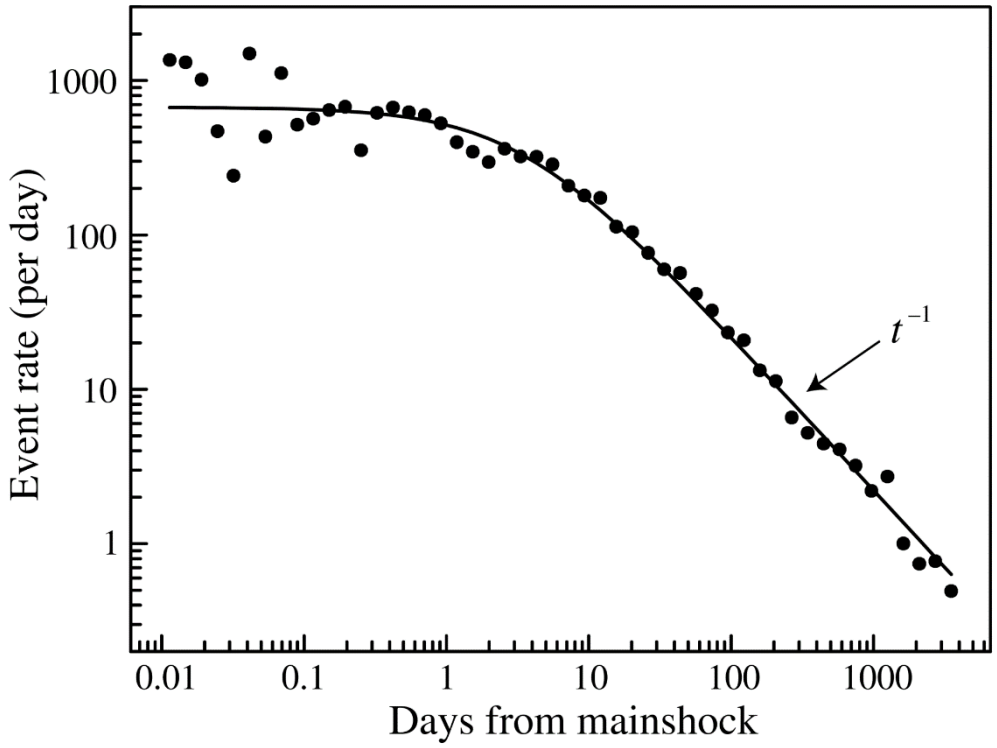

Figure 1.1. Example of the Omori's law. Aftershock rate for the 1994 Northridge, California, earthquake as a function of time after the mainshock. The line shows the Omori's law prediction for K = 2230, c = 3.3 days, and p = 1 (modified from Shearer, 2009).

The interval of earthquake cycles is largely controlled by the fault zone properties, tectonic setting, influence from the change of loading stress, etc. In particular, as regards the tectonic setting, it is well known that earthquakes nucleate within extensional, compressional or strike-slip environments.

Extension in continental crust is accompanied by a substantial amount of active seismogenic faults, often producing large earthquakes; extensional regimes are quite varied, ranging from rifts to broad extensional regions to incipient zones of back-arc spreading (Scholz, 2002). Large normal faulting earthquakes occur in these zones and typically nucleate at depths of 6–15 km on faults dipping between 30° and 60° (Jackson, 1987). Examples of extensional settings can be located in the Basin and Range (western USA; e.g., Parsons, 2006), the Gulf of Corinth (Greece; e.g., Taylor et al., 2011), Central and Southern Apennines (Italy; e.g., Doglioni, 1991), the East African Rift (Eastern Africa; e.g., Chorowicz, 2005), the Taupo volcanic zone (New Zealand; e.g., Rowland and Sibson, 2001), the Baikal Rift Zone (South-eastern Russia; e.g., Zhao et al., 2006). Moreover, extensional faulting events can also nucleate along divergent margins, in correspondence with mid-oceanic ridges, which can be considered seismically active; in particular, these seismic events are located on the flanks close to the ridge crest and are driven by isostatic uplift of the depressed central rift valley; these events seldom exceed M_s 6.5 (e.g., Scholz, 2002). Moderate earthquakes have been occurred in extensional environments, such as the 1995 M_w 6.2 Aigion earthquake (Greece; e.g., Bernard et al., 1997), the 1997 M_w 5.9 Athens earthquake (Greece, e.g., Papadimitriou et al., 2002), the 2009 M_w 6.3 L'Aquila earthquake (Central Italy; e.g., Castaldo et al., 2018) and the 2016 M_w 6.5 Norcia earthquake (Central Italy; e.g. Cheloni et al., 2017).

Compressional tectonics takes place in correspondence of subduction zones, where oceanic lithosphere is thrust under the adjacent continental or oceanic lithosphere and this subduction process allows the development of orogenic belts (e.g., Ruff and Kanamori, 1980). The well-known Pacific Ring of Fire can be taken as an example for this kind of compressional environments (e.g., Uyeda and Kanamori, 1979). Furthermore, compressional tectonics affects the lithosphere during collision processes between continental plates (as the collision between the Arabian and Eurasian plates and between the Indian and Eurasian plates, associated with the Zagros and the Himalayan fold-thrust-belts, respectively; e.g., Yin and

Harrison, 2000; Alavi, 2007) and/or between a continent and an island arc leads to the formation of orogenic belts (such as that which formed the Island of Taiwan; e.g., Sibuet and Hsu, 1997). The most disruptive earthquakes occurred in compressional environments, such as the 1960 M_w 9.5 Valdivia earthquake (Chile; e.g. Hu et al., 2004), the 2004 M_w 9.3 Sumatra earthquake (Indonesia; Stein and Okal, 2005), the 2011 M_w 9.0 Tohoku-Oki earthquake (Japan; e.g., Ozawa et al., 2011), the 2015 M_w 8.0 Gorkha earthquake (Nepal; e.g., Castaldo et al., 2017).

Strike-slip tectonics occurs in regions where a state of shear is prevailing. Areas of strike-slip tectonics are associated with continental and oceanic transform boundaries and with lateral ramps in areas of extensional or compressional tectonics. In correspondence with continental boundaries, transform faults are located within continental plates; this category includes some of the best known examples of strike-slip structures such as such as the San Andreas Fault (western USA; e.g., Fialko, 2006), the Dead Sea Transform (Russia; e.g., Girdler, 1990), the North Anatolian Fault (Turkey; e.g., Şengör et al., 2005) and the Alpine Fault (New Zealand; e.g., Leitner et al., 2001). In case of oceanic boundaries, mid-ocean ridges are broken into different segments that offset from each other by transform faults; the active part of the transform links the two ridge segments. Some of these transforms can be very large, such as the Romanche fracture zone, whose active portion extends for about 300 km (e.g., Bonatti et al., 1994). Moreover, in the specific case of lateral ramp, major lateral offsets between large extensional or thrust faults are normally connected by diffuse or discrete zones of strike-slip deformation which allow transfer of the overall displacement between the structures. In correspondence with these strike-slip environments, medium-high magnitude earthquakes have nucleated over the centuries, such as the 1992 M_w 7.3 Landers earthquake (California, USA; e.g., Fialko, 2004), the 1999 M_w 7.5 Izmit earthquake (Turkey, Reilinger et al., 2000), the 2002 M_w 7.9 Denali earthquake (Alaska, USA; e.g., Dreger et al., 2004) and the 2010 M_w 7.1 Darfield earthquake (New Zealand; e.g. Quigley et al., 2012).

During seismic events within extensional, compressional and/or strike-slip tectonic settings, the relative motion of the rock blocks produces a displacement across the involved seismogenic fault. Both thrust faults and normal faults are also known as dip–slip faults because the displacement along the fault

takes place on a dipping plane, whereas a strike-slip fault is a fault along which the displacement is strictly horizontal. Displacements on faults accommodate a substantial portion of the regional and local strain in the continental crust. The displacement on the fault during the earthquake occurs in a few seconds and can be measured from the surface rupture (Kanamori and Brodsky, 2004).

The coseismic displacement is related to several peculiar characteristics of the considered fault (i.e., friction along the fault planes, fault length, fault dip) and to the entity of the seismogenic rock volumes involved in the earthquake nucleation process. The larger the volume, the bigger the coseismic displacement (Doglioni et al., 2015a). The dimension of the seismogenic volume, in turn, is influenced by the depth of the brittle-ductile transition (BDT) and the rock volume size also conditions the earthquake magnitude: the deeper the BDT, the larger the volume and the higher the earthquake magnitude. Therefore, friction controls fault dip, and fault dip determines the vertical component of the coseismic displacement, plus the depth of the BDT constrains the maximum volume involved. The higher these parameters, the larger the earthquake magnitudes. The role of the rock volume and the deformation processes that affect these blocks during earthquake nucleation are widely recognized (e.g., Thompson and Parsons, 2016; Thompson and Parsons, 2017).

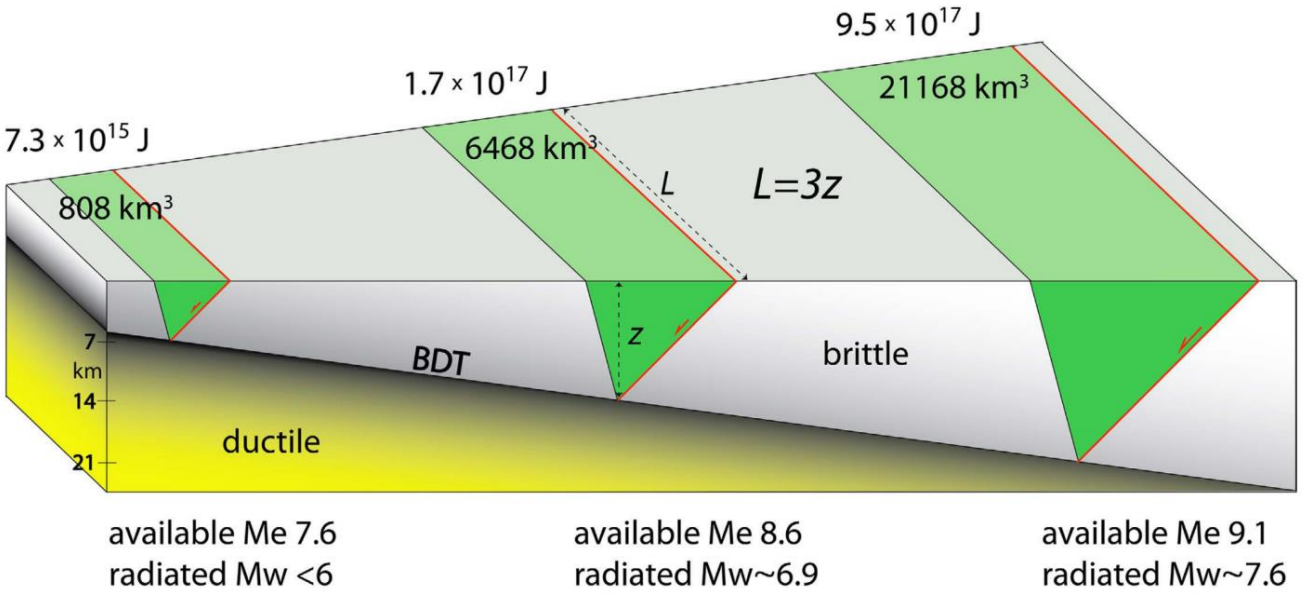

Figure 1.2. Coseismic volumes. Three cases of 45° dipping normal faults, with BDT and hypocentre depths at 7, 14 and 21 km. This sketch clearly shows the relationship between the fault length, the BDT depth, the rock volume size, the earthquake magnitude and the coseismic displacement (modified from Doglioni et al., 2015a).

To understand the process of fault zone activities in the earthquake cycle as well as the connection to the long-term tectonic loadings, we rely on precise and dense observations of crustal deformation in space and time. Modern technology in seismology and remote sensing allows us to record the deformation history during and after earthquakes. In seismology, strong motion and broadband seismic sensors can detect acceleration and velocity in a very wide range of frequency. In remote sensing, the global positioning system (GPS) measurements are used to observe the surface displacement in 3D with centimetre-scale accuracy. Overall, the uncertainty of GPS is generally less than 1 cm in horizontal and about three times higher in vertical. For active tectonic studies, GPS is used for coseismic static displacement, postseismic deformation measurement with time, interseismic deformation, and plate motions (i.e. secular motion). Another technique, the Interferometric Synthetic Aperture Radar (InSAR), has been developed since early 1990s (Massonnet, 1992). A SAR interferogram can detect a map of surface displacement in line of sight (LOS) with tens of metres resolution and sub-centimetre accuracy between two SAR image acquisitions. InSAR has been widely used for observing crustal deformation including co-, post-, and interseismic displacement, volcanic deformation, land subsidence, and glacial movement. Understanding the earthquake source process is one of the most important topic; indeed, the earthquake source describes the dimension, depth, and the mechanism of the earthquake.

Furthermore, together with the modern seismological and remote sensing techniques, it is possible to resort to numerical modelling, to understand and simulate the earthquake nucleation processes. Indeed, it is known that most of the geological processes occur at timescales and depths such that they cannot be observed directly; moreover, direct measurements of some parameters, such as stress, strain rate, composition, temperature, pressure, are limited to few rock samples. The high complexity of geological situations and the partial data that can be obtained from direct or indirect observation has led structural geologists to simulate natural phenomena in order to better understand and predict them. Such modelling process requires to simplify the observed or interpreted phenomena and consists in trying to reproduce them by some appropriate method. The first method which has been used for simulating geological processes is the so-called analogue modelling; by using this approach, it is possible to define models at

reduced geometric and time scales. Such models behave in an analogue way than their corresponding idealised reality, thus they allow to apprehend physical processes at reasonable scales (Hubbert, 1937). In all these models, the displacements field is obtained either by direct visualisation (through transparent boundaries), by destructive methods or by X-ray tomography; unfortunately, no information is obtained on the stress field (Simpson, 2017). However, a very interesting aspect of these models comes from their relatively easy use, their natural finite strain "formulation" and their ability to treat three dimensional problems. These methods allow to reconstruct the initial configuration from the interpreted currently structures, and therefore to validate an interpretation from a geometrical point of view. Despite the high interest of such method, its main disadvantage lies in the fact that the obtained solution does not necessarily verify mechanical equilibrium. In order to overcome this deficiency, numerical models which verify the physical equilibrium of the solution have been applied to geological problems. This modelling has been allowed with the development of approached numerical methods such as the finite element method (e.g., Barnichon, 1998). This method has originally been developed to solve continuum mechanics problems encountered in aeronautics and civil engineering; subsequently, this method has been applied to study geological problems such as folding (e.g., Parrish et al., 1976) or petroleum related structural problems (e.g., Nieuwland and Walters, 1993). By using numerical models, it is possible to know the distribution and variations of such parameters within a computational domain. Numerical modeling uses mathematical models to describe the physical conditions of geological scenarios using numbers and equations (Ismail-Zadeh and Tackley, 2010). Therefore, numerical modelling has become an indispensable tool for Earth scientists to understand and make predictions about the evolution through time and space of complex geological systems together with laboratory experiments and field and geophysical observations. In fact, nowadays, numerical modelling is used to study rock mechanics, thermal history of rocks, movements of tectonic plates and the Earth's mantle; also fluids flow, earthquakes nucleation and volcanic eruptions can be simulated using numerical methods. Both qualitative and quantitative understanding of a variety of geological processes can be developed via these experiments.

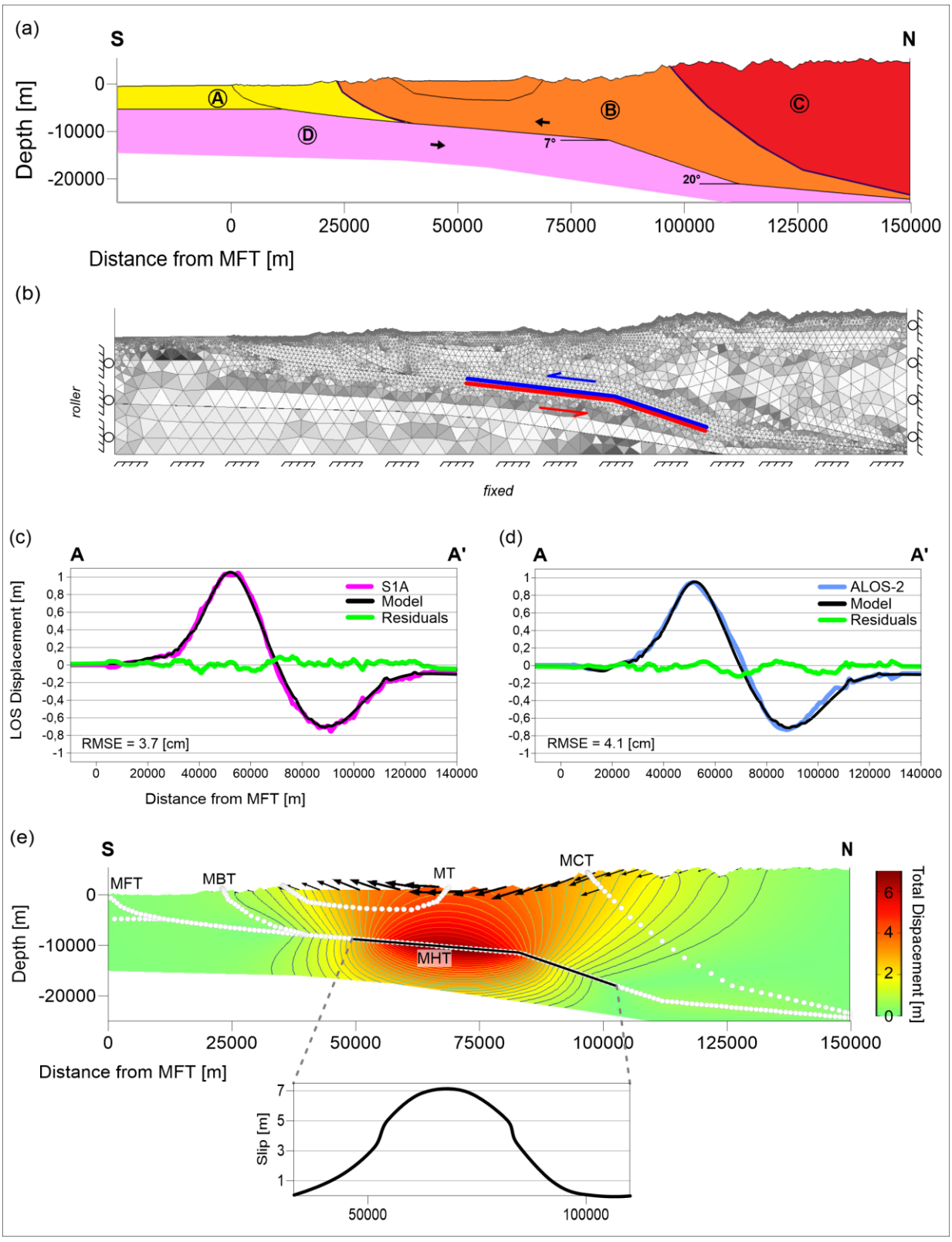

Figure 1.3. Numerical modelling example: the M_w 7.8 Gorkha earthquake (Nepal, 2015). (a) Simplified geological cross-section in the FE environment; (b) Discretized numerical domains with the boundary conditions. (c-d) Comparison between the (c) S1A (magenta line) and (d) ALOS-2 (blue line) DInSAR measurements and the corresponding LOS-projected results of the FE model (black lines). (e) Image and contour lines of the retrieved displacements, modelled along the considered 2D section (modified from Castaldo et al., 2017).

The principal topic of this Ph.D. thesis is the integration of seismological data, geodetic measurements and numerical modelling to analyse seismic events; in particular, due to the occurrence of the 2016-2017 Central Italy seismic sequence, we take into account as a case-study the October 30th, 2016 M_w 6.5 Norcia earthquake. Moreover, we focus my research on the analysis and comparison of extensional and compressional seismic sequences to understand the differences between these two tectonic settings in terms of aftershocks duration (see Chapter 2). To perform this analysis, we employ two different approaches to determine both the duration and the number of events of the selected aftershock sequences. This study reveals that, irrespective of the magnitude, the average duration of aftershock sequences within extensional tectonic settings is longer than that of aftershock sequences within compressional tectonic settings; furthermore, extensional aftershock sequences comprise more seismic events than those within compressional earthquakes. We propose that the type of energy released during the earthquakes, in turn related to the tectonic setting, controls the different duration of seismic sequences: on one hand, a combination between gravitational forces and pure elastic stress release governs extensional earthquakes; on the other hand, pure elastic stress release controls compressional earthquakes. This comparative analysis of aftershock seismic sequences is useful in understanding the mid-term behaviour of an ongoing seismic sequence within different tectonic settings and can provide useful inputs to improve seismic hazard assessment. This work has been published in *Scientific Reports* in 2017 (Valerio et al., 2017). In particular, for the realization of this work I have run the calculations, contributed to the set-up of the analysis, assessment of the results and interpretation, prepared the figures and written the paper, being supported by the co-authors in the analysis and discussion of results.

The occurrence of the seismic sequence that suddenly struck the Central Italy since August 2016 allows us to apply the two abovementioned approaches to the M_w 6.5 Norcia earthquake. As the other examined extensional seismic sequences, this event also present a longer aftershocks sequence duration with respect to the considered compressional seismic sequences. Starting from this analysis, we select the M_w 6.5 Norcia earthquake to apply a multidisciplinary approach by integrating several geodetic (DInSAR measurements and GPS data), relocated hypocentres distribution and structural data in a finite element

model. Specifically, to measure the crustal deformation associated with the 30 October 2016 M_w 6.5 Norcia earthquake nucleation (i.e., coseismic phase), we use multi-orbit and multi-temporal DInSAR (Differential Interferometric Synthetic Aperture Radar) measurements and we also consider available GPS data; indeed, these geodetic data can provide ground velocity and deformation maps with a sub-centimetric accuracy. This level of accuracy makes the interferometric methods very suitable and useful for the study of tectonic processes, such as earthquakes nucleation.

In a second step, we take into account the relocated hypocentres with $0.1 \leq M_w \leq 6.5$, occurred between August 24th and November 29th, 2016 and recorded by the INGV seismometric network. The spatial and temporal distribution of the seismicity allows to individuate the seismogenic faults activated during the seismic sequence and their geometrical properties. Moreover, after the analysis of the tectonic alignments highlighted by earthquakes spatial distribution, we also compare the literature information available for these seismogenic fault and this Apennine sector.

As last step of my work, we perform a physically-based numerical modelling of the observed vertical ground deformation retrieved via DInSAR Interferometry. In particular, we integrate in the numerical environment the a priori available geological and structural framework and the seismicity distribution of the seismogenic area, to take into account the mechanical heterogeneity and the active alignments that characterize the upper crust in the Apennines chain. To simulate the possible structural frameworks of the investigated area, we define two possible opposite scenarios: (i) a single SW-dipping fault and (ii) a single SW-dipping fault with an antithetic zone. All the employed techniques, the available data and the achieved results are thoroughly presented in Chapter 3. DInSAR data processing and analysis and numerical modelling were developed in collaboration with the Istituto per il Rilevamento Elettromagnetico dell'Ambiente (IREA-CNR, Naples). This work has been published on *Remote Sensing* (Valerio et al., 2018). In particular, for the realization of this work I have analysed DInSAR data, run the calculations, developed numerical modelling, contributed to the set-up of the analysis, assessment of the results and interpretation, prepared the figures and written the paper. My co-authors contributed in the analysis and discussion of results. Moreover, in addition to DInSAR measurements, also GPS data were used to

investigate the ground displacements caused by the earthquake nucleation; this analysis is thoroughly reported in Cheloni et al. (2017) and I am a co-author of this work. In particular, I have contributed realizing some sections in which the relocated hypocentres were projected; this analysis was performed by employing specific software and was useful to identify the geological structures involved during the mainshocks.

The results obtained by the integration of the abovementioned employed techniques are extensively discussed in Chapter 4. Finally, in Chapter 5 the studies performed during this Ph.D. are summarized and suggestions for future work are reported.

To sum up, in this Ph.D. thesis we: a) examine seismic sequences nucleated in different tectonic settings to understand the behaviour of the aftershocks over time; b) investigate the ground deformation pattern generated by the 30 October M_w 6.5 Norcia earthquake, also considering the available GPS measurements; c) analyse the relocated hypocentres distribution in order to identify the involved seismogenic faults and their geometrical characteristics; d) integrate all the geodetic, seismological and structural information in a finite element modelling.

The approaches used in this Ph.D. thesis can improve the understanding of the mid-term behaviour of an ongoing seismic sequence within different tectonic setting and the knowledge about earthquakes kinematics; both analysis can furnish valid inputs to enhance seismic hazard assessment within active seismogenic areas.

Chapter 2

Duration of aftershock seismic sequences

2.1. Introduction

Every day, moderate-to-large magnitude earthquakes release seismic energy stored within the Earth's crust. This energy is accumulated for tens or thousands of years during the inter-seismic phase and released instantaneously (i.e., within seconds) through an earthquake (i.e., the mainshock) during the co-seismic phase (Dahlen, 1977; Scholz, 2002; Kanamori and Brodsky, 2004; Gentili and Di Giovambattista, 2017). After the mainshock, the energy release continues (for months to years) during the post-seismic phase in the form of aftershocks, generally characterized by magnitudes smaller than the mainshock (Savage, 1983). A worldwide earthquake analysis using data from the Global Harvard Centroid-Moment-Tensor (CMT) Catalog (Dziewonski et al., 1981; Ekström et al., 2012) shows that earthquakes within compressional tectonic settings are characterized by higher magnitude values (up to 9.5) than those within extensional tectonic settings (generally up to 7 with few exceptions; Figure 2.1b). Schorlemmer et al. (2005) calculated the b-value of the Gutenberg-Richter law:

$$logN = a - bM \tag{2.1}$$

where N is the number of events within a certain range of magnitude, a and b are two constants and M is the minimum magnitude. Their estimated b-value is equal to 1.1 for extensional and to 0.9 for compressional tectonic settings. Large earthquakes affect smaller crustal volumes in extensional tectonic settings than in compressional settings; this was proposed as the main reason for the occurrence of smaller magnitude earthquakes in rift zones (Doglioni et al., 2015). Few studies have focused on the control of the tectonic setting on the duration of aftershock sequences. A better understanding of the processes ruling the decay of aftershock with time (aftershocks decay) is fundamental to better constrain seismic hazard during

ongoing seismic sequences. Within a seismic sequence, seismological observations indicate that the aftershocks decay follows the Omori-Utsu law (Omori, 1894; Utsu, 1961):

$$n(t) = \frac{k}{(c+t)^p} \tag{2.2}$$

where k and c are constants, t is the time and p indicates the decay rate. The aftershocks decay also depends on several parameters peculiar to each seismogenic region, such as the tectonic setting (i.e., extensional, strike-slip, compressional regimes), the stress changes along fault, the structural heterogeneities, and the crustal rheology (Shaw, 1993; Utsu and Ogata, 1995; Shcherbakov et al., 2004). However, the geological and seismotectonic parameters that control the aftershocks decay during seismic sequences are still unclear (Utsu and Ogata, 1995).

In this chapter, we focus on how the tectonic setting controls the aftershocks decay within seismic sequences. In particular, we analyse data from international catalogues with two different methods, comparing the aftershock sequences following five extensional settings mainshocks and five compressional settings mainshocks (Figure 2.1a; Table 2.1). The average duration of aftershock sequences is longer, and the number of events is larger within extensional tectonic settings with respect to compressional tectonic settings. We propose an interpretation of these different behaviours in terms of differences in the orientation of forces acting during earthquake nucleation processes in the two settings.

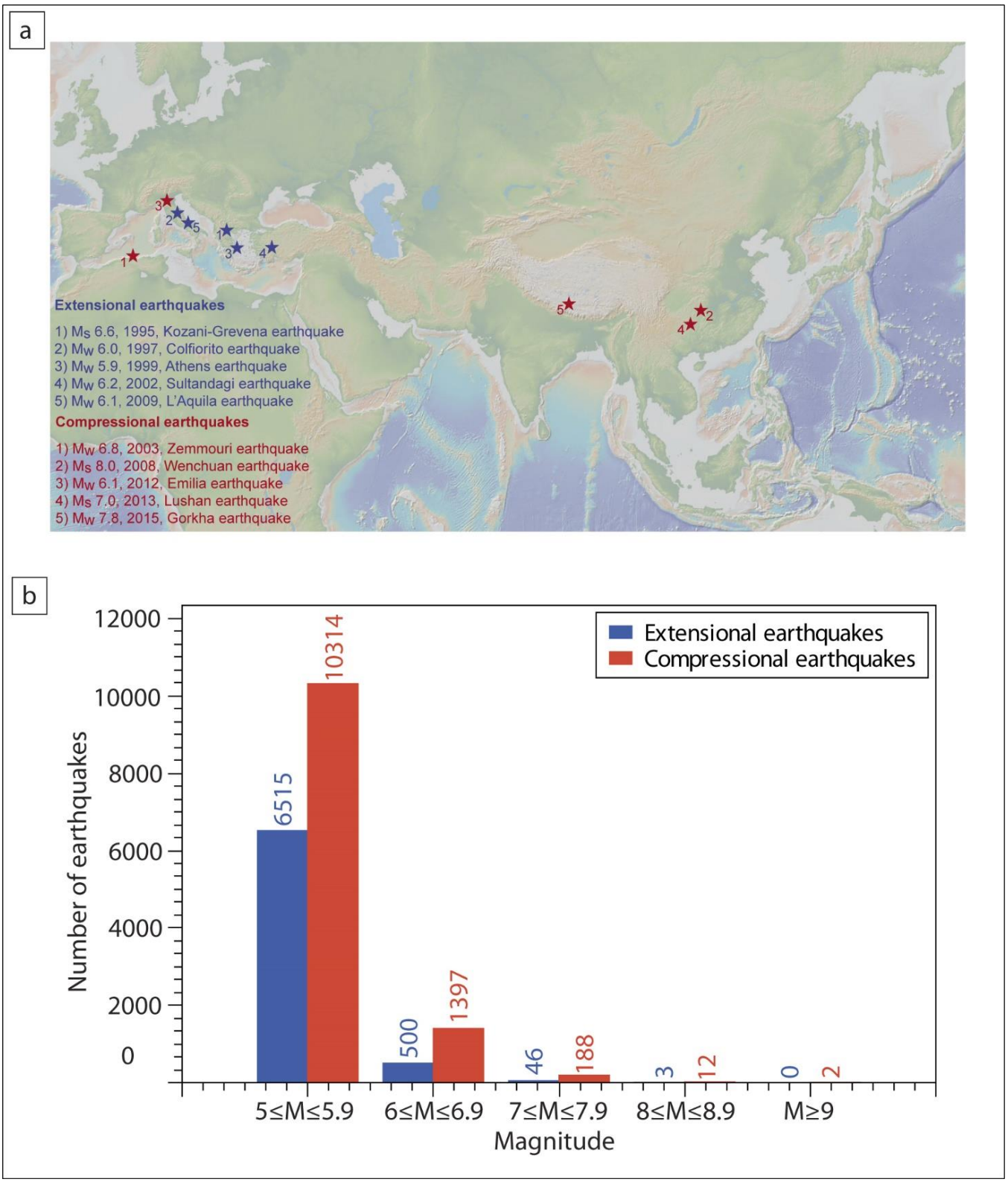

Figure 2.1. Earthquakes general information. (a) Geographic location of the ten analysed case studies. Extensional earthquakes are shown in blue: 1) the M_s 6.6 Kozani-Grevena earthquake (1995, Greece), 2) the M_w 6.0 Colfiorito earthquake (1997, Central Italy), 3) the M_w 5.9 Athens earthquake (1999, Greece), 4) the M_w 6.2 Sultandagi earthquake (2002, Turkey), and 5) the M_w 6.3 L'Aquila earthquake (2009, Central Italy). Compressional earthquakes are shown in red: 1) the M_w 6.8 Zemmouri earthquake (2003, Algeria), 2) the M_s 8.0 Wenchuan

earthquake (2008, China), 3) the M_w 6.1 Emilia earthquake (2012, Northern Italy), 4) the M_s 7.0 Lushan earthquake (2013, China), and 5) the M_w 7.8 Gorkha earthquake (2015, Nepal); the map was obtained by using the software GeoMapApp (www.geomapapp.com; Ryan et al., 2009). (b) Histogram of the world earthquakes occurrence versus magnitude from 1976 to the present, in both extensional and compressional tectonic settings. Extensional compressional earthquakes are indicated in blue and red, respectively. We used the Global Harvard Centroid-Moment-Tensor (CMT) Catalog (Dziewonski et al., 1981; Ekström et al., 2012) and selected seismic events (1976 to present) occurred down to 40 km depth and within the 5–10 magnitude range. To classify seismic events as thrust or normal events, we used the tension axis plunge and the null axis plunge values. This is consistent with the CMT Catalog report, which indicates that thrust faults have large plunge (>45°) of tension axis, strike-slip faults have large plunge of null axis, and extensional faults have small plunge (<45°) for both tension and null axes.

2.2. Materials and Methods

2.2.1. Collected data

In order to achieve comparable and homogeneous seismic sequences, we adopted the following criteria during the selection of earthquake sequences:

(i) presence of local and well-distributed seismometric stations to avoid the occurrence of spatial gaps within the seismic sequence;

(ii) existence of complete seismological catalogues to avoid the occurrence of temporal lacks within the seismic sequence;

(iii) maximum hypocentral depth of 40 km (i.e., crustal earthquakes), thus excluding deeper subduction-related earthquakes;

(iiii) mainshocks of M>5.5 to obtain representative aftershock sequences.

We selected the following seismic sequences within extensional tectonic settings: Italian Central Apennines (1997, Colfiorito earthquake, M_w 6.0 and 2009, L'Aquila earthquake, M_w 6.3); Greece (1995, Kozani-Grevena earthquake, M_s 6.6, and 1999, Athens earthquake, M_w 5.9); central-western Turkey (2002, Sultandagi earthquake, M_w 6.2; Figure 2.1a and Table 2.1). Within compressional tectonic settings, we analysed earthquakes occurred within the following fold-and-thrust belts: Algerian Tell (2003, Zemmouri earthquake, M_w 6.8); Italian Northern Apennines (2012, Emilia earthquake, M_w 6.1); Nepalese Himalaya (2015 Gorkha earthquake, M_w 7.8); Chinese Sichuan Province (2008, Wenchuan earthquake, M_s 8.0, and 2013, Lushan earthquake, M_s 7.0; Figure 2.1a and Table 2.1). We used seismic data presented in following catalogues: the INGV Earthquake Centre (National Institute of Geophysics and Volcanology, Italy, http://iside.rm.ingv.it, to analyse the 1997 Colfiorito, 2009 L'Aquila and 2012 Emilia sequences); the CENC (China Earthquake Network Center, China, http://www.csi.ac.cn/sichuan/ index080512001.htm, to analyse the 2008 Wenchuan sequence, 2013 Lushan sequence and 2015 Gorkha sequences); the KOERI (Kandilli Observatory and Earthquake Research Institute, Turkey, http://www.koeri. boun.edu.tr, to analyse the 2002 Sultandagi sequence) and the NOA (National Observatory of Athens, Greece, http://www.gein.noa.gr, to analyse the 1995 Kozani-Grevena and the 1999 Athens sequences). We

compared these data with those from the ISC (International Seismological Centre; http://www.isc.ac.uk) catalog. Specifically, in case of the 2003 Zemmouri sequence (Algeria), we only used seismological data included in the ISC catalogue because, at the moment, a local Algerian seismological catalogue is unavailable.

Earthquake	Occurrence	Magnitude	M_0 (N*m)	Aftershocks sequence duration		Number of aftershocks	
				Tangents method	Mandelbrot method	Tangents method	Mandelbrot method
Extensional earthquakes							
Kozani-Grevena earthquake	13rd May 1995	M_s 6.6	$7.6*10^{18}$ (Meyer et al., 1996)	~300 days	~350 days	989	998
Colfiorito earthquake	26th September 1997	M_w 6.0	$1.2*10^{18}$ (Ekström et al., 1997)	~330 days	~330 days	2119	2119
Athens earthquake	7th September 1999	M_w 5.9	$1.0*10^{18}$ (Papadimitriou et al., 2002)	~300 days	~400 days	281	295
Sultandagi earthquake	3rd February 2002	M_w 6.2	$2.4*10^{18}$ (Ergin et al., 2009)	~500 days	~540 days	922	944
L'Aquila earthquake	6th April 2009	M_w 6.3	$3.9*10^{18}$ (Cheloni et al., 2010)	~515 days	~560 days	915	925
Compressional earthquakes							
Zemmouri earthquake	21st May 2003	M_w 6.8	$2.89*10^{19}$ (Delouis et al.,2004)	~100 days	~165 days	400	423
Wenchuan earthquake	12th May 2008	M_s 8.0	$9.4*10^{20}$ (Zhang et al., 2009)	~230 days	~230 days	1859	1859
Emilia earthquake	20th May 2012	M_w 6.1	$1.81*10^{18}$ (Pondrelli et al., 2012)	~110 days	~120 days	782	784
Lushan earthquake	20th April 2013	M_s 7.0	$1.01*10^{19}$ (Liu et al., 2013)	~35 days	~35 days	122	122
Gorkha earthquake	25th April 2015	M_w 7.8	$7.55*10^{20}$ (Feng et al., 2015)	~130 days	~130 days	786	786

Table 2.1. Case studies. List of ten case studies divided according to the fault kinematics. In this table we also reported earthquake characteristics (fault kinematics, occurrence, magnitude, seismic moment M_0), the results obtained for each seismic sequence by using two different methods (e.g., the Tangents method and the Mandelbrot method) and the number of aftershocks occurred with $M \geq 2.5$.

2.2.2. Methods to determine the duration of aftershocks

In addition to the classical Omori law analysis performed to verify the completeness of the used seismic catalogues (results are reported in Figures A1 and A2 and Table A1 of the Appendix), we employed two novel approaches to determine the duration and the number of events of the selected aftershock sequences:

i) **Tangents method.** We used the QtiPlot software to elaborate a statistical-descriptive analysis of seismic sequences. We adopted a completeness (threshold) magnitude (M_c) of 2.5 as, below this threshold, the number of recorded seismic events strongly depends on the sensitivity of the seismic network, which varies from place to place. The adoption of a completeness magnitude, chosen on the basis of the minimum magnitude reported in each catalogue, allowed us to remove the seismic noise. The methodology is based on the comparison of the curves representing the cumulative number of earthquakes for each seismic sequence versus the days elapsed from the mainshock (Figure 2.2). In principle, the lower the completeness magnitude, the greater the completeness of the curve. The corresponding curves present an initial non-linear increase followed by a linear one (Figures 2.2 and 2.3). The initial non-linear trend suggests that the seismic sequence related to the mainshock is still active, whereas the linear increment represents the characteristic background seismicity of the region. We consider the day when the tangent to the linear increment starts from the cumulative curve as indicative of the end of the aftershock sequence. We used this analysis also to compare the three selected Italian earthquakes: the 1997 (M_w 6.0) Colfiorito and the 2009 (M_w 6.3) L'Aquila extensional earthquakes and the 2012 (M_w 6.1) Emilia compressional earthquake, characterized by similar magnitudes and recorded by the same seismometric network (Figure 2.4). In this case, we adopted a completeness magnitude (M_c) of 1.6.

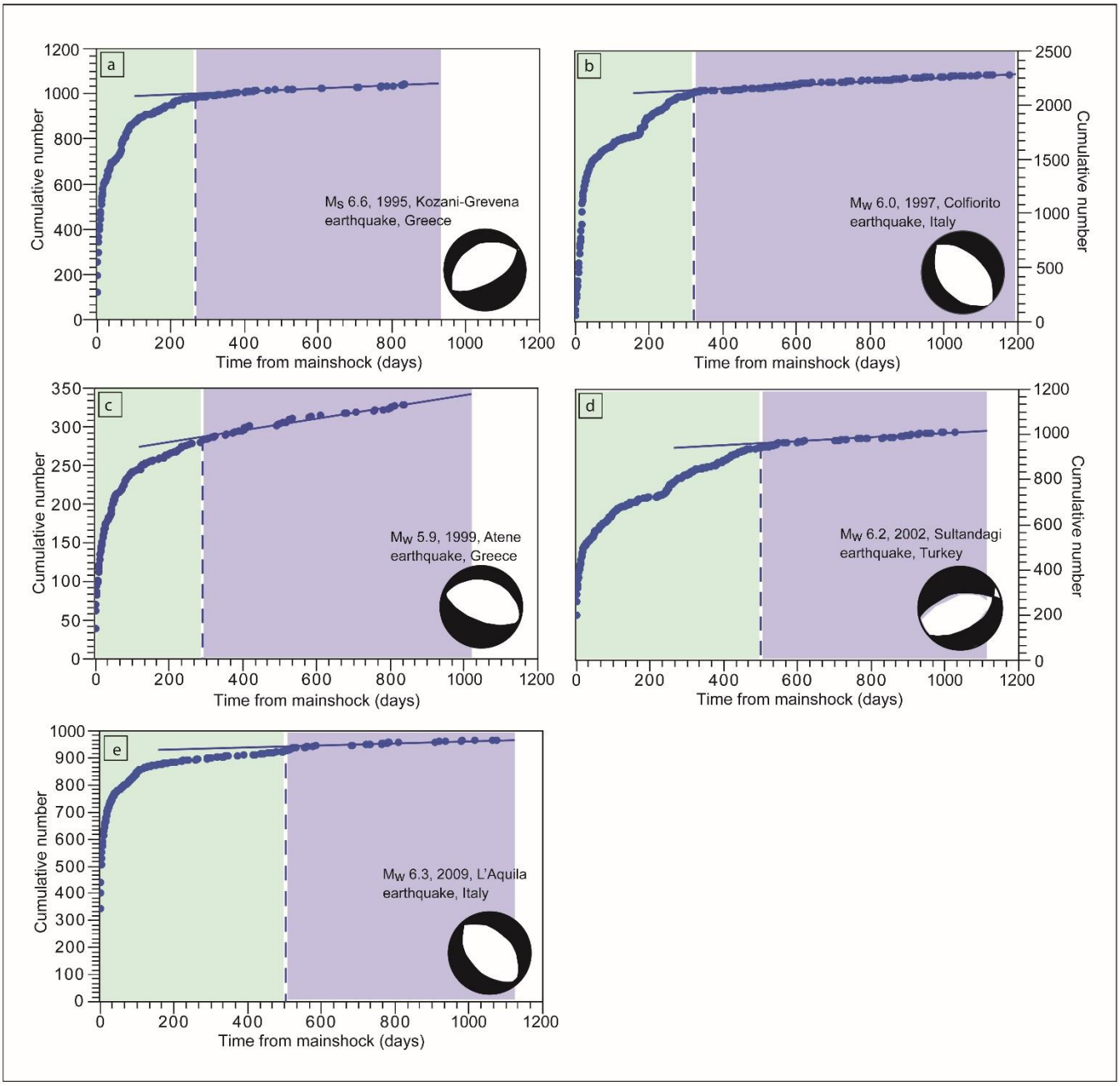

Figure 2.2. Tangents method applied to extensional seismic sequences. Aftershock sequences temporal evolution analysed by using the Tangents method, following five mainshocks nucleated in extensional areas: (a) the M_s 6.6 Kozani-Grevena earthquake (1995, Greece), (b) the M_w 6.0 Colfiorito earthquake (1997, Central Italy), (c) the M_w 5.9 Athens earthquake (1999, Greece), (d) the M_w 6.2 Sultandagi earthquake (2002, Turkey), and (e) the M_w 6.3 L'Aquila earthquake (2009, Central Italy). The cumulative number of earthquakes is shown versus the days from the mainshock nucleation. The blue dashed lines indicate the onsets of the linear trends, which are fitted by the blue solid lines. The light green and blue areas represent the seismicity related to the mainshock and the background seismicity, respectively.

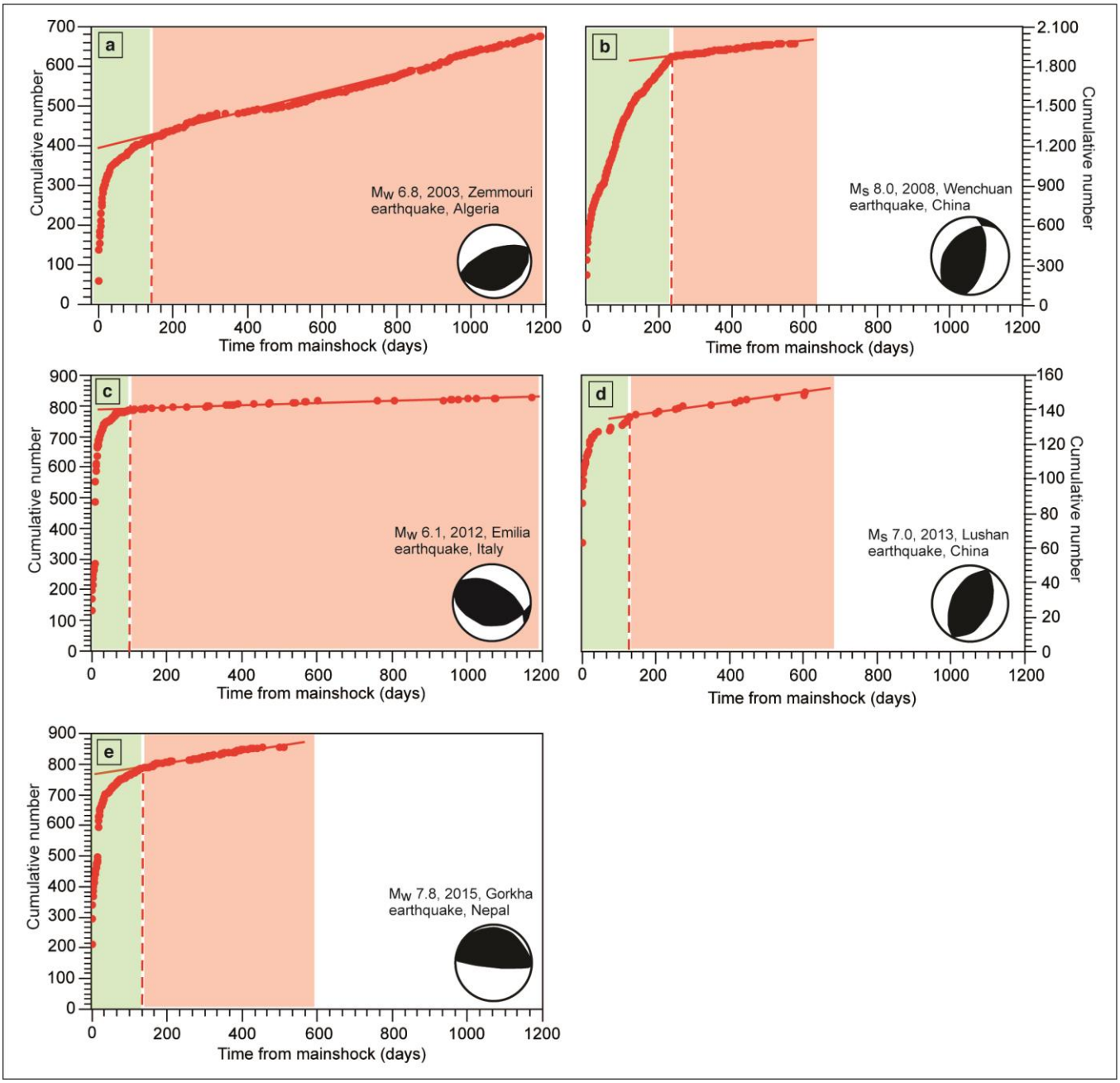

Figure 2.3. Tangents method applied to compressional seismic sequences. Aftershock sequences temporal evolution analysed by using the Tangents method, following five mainshocks nucleated in compressional areas: (a) the M_w 6.8 Zemmouri earthquake (2003, Algeria), (b) the M_s 8.0 Wenchuan earthquake (2008, China), (c) the M_w 6.1 Emilia earthquake (2012, Northern Italy), (d) the M_s 7.0 Lushan earthquake (2013, China), and (e) the M_w 7.8 Gorkha earthquake (2015, Nepal). The cumulative number of earthquakes is shown versus the days from the mainshock nucleation. The red dashed lines indicate the onsets of the linear trends, which are fitted by the red solid lines. The light green and red areas represent the seismicity related to the mainshock and the background seismicity, respectively.

To understand the physical reason of the change of slope in the cumulative curves, we calculated the strain energy release E_s generated by the earthquakes nucleation, which is related to the magnitude values M by the following empirical relation (Bath and Duda, 1964; Bath, 1966; Figures A3 and A4):

$$log\ E_s = 1.44M + 5.24 \tag{2.3}$$

where E_s is in Joule. In particular, we want to investigate the relationship between the energy released during the seismic sequence and the number of seismic events, represented by the cumulative curves.

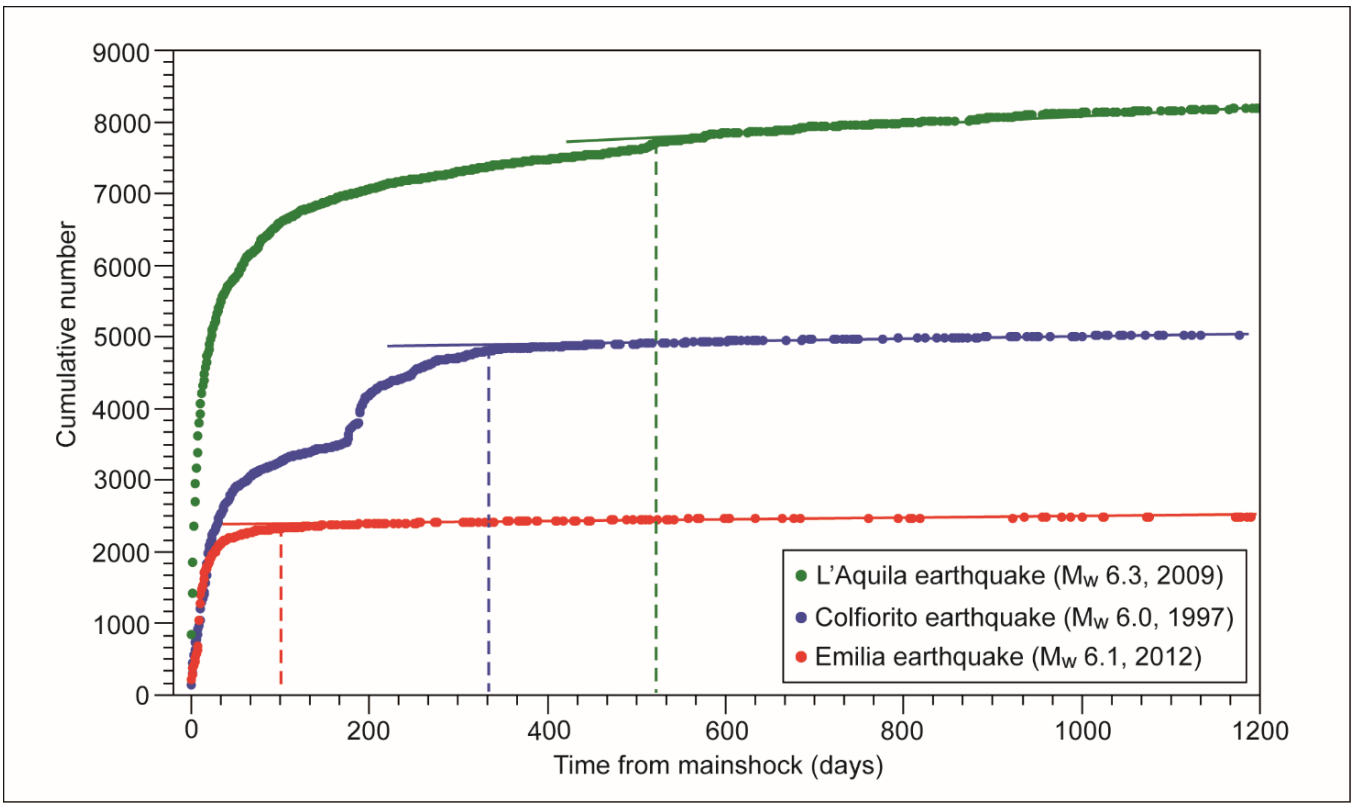

Figure 2.4. Tangents method applied to Italian seismic sequences. Comparison of aftershock sequences temporal evolution analysed by using the here proposed Tangents method in case of two Italian extensional earthquakes (the M_w 6.0 Colfiorito earthquake, 1997, Central Italy and the M_w 6.3 L'Aquila earthquake, 2009, Central Italy) and an Italian compressional earthquake (the M_w 6.1 Emilia earthquake, 2012, Northern Italy). The cumulative number of earthquakes is shown versus the days from the mainshock nucleation. The dashed lines indicate the onsets of the linear trends, which are fitted by the solid lines. The M_c is set at 1.6.

ii) **Mandelbrot method.** We used a numerical computing software to examine faulting and fragmentation processes using the fractals theory (Turcotte, 1986; Mandelbrot, 1989). In this context, the fractal geometries are strictly related to the fragmentation processes caused by earthquake nucleation. The variation of fractal parameters can thus be indicative of the temporal and spatial evolution of the fragmentation processes along a fault system in time and space. We analysed the seismological data with the software, fitting the same data with a linear regression, and obtained the fractal dimension and the related coefficient of determination (i.e., R-squared). This method allows the representation of the magnitude-frequency distribution of earthquakes. We realized semi-logarithmic graphs for each seismic sequence, in which we compared the number of earthquakes occurred in certain magnitude ranges. The fitting straight line represents a simple linear regression according to the following equation, which also defines a fractal set:

$$N_i = C r_i^{-D} \tag{2.4}$$

where N_i is the number of objects with a characteristic linear dimension r_i, C is a constant of proportionality, and D is the fractal dimension (Turcotte, 1997; Figures 2.5 and 2.6). All these parameters directly derive from the regression lines automatically calculated by the used software. R-squared can range between 0 and 1. The higher the R-squared values, the higher the model accuracy. The high R-squared values in our studies (R^2>0.95 in 90% of the cases and in one case R^2=0.91) point to a good fit between the model accuracy and the data instability. According to this topological analysis, the fractal dimension value represents the level of irregularity of the selected fractal set (Mandelbrot, 1989) and is indicative of the fragmentation process occurred during the mainshock and the following aftershocks. If D=0, it represents the classical Euclidean dimension of a point; if D=1, the dimension of a line segment; if D=2, the dimension of a surface and, finally, if D=3, the Euclidean dimension of a volume (Mandelbrot, 1989; Turcotte, 1997). To check data accuracy, w calculated the coefficient of determination (R-squared) connected with Equation 4 for each seismic sequence (Figures A5, A6, A7 and A8). R-squared represents

the variability between data instability and model accuracy. To establish the durations of aftershock sequences, we applied the Tangents method on the obtained fractal dimension trend.

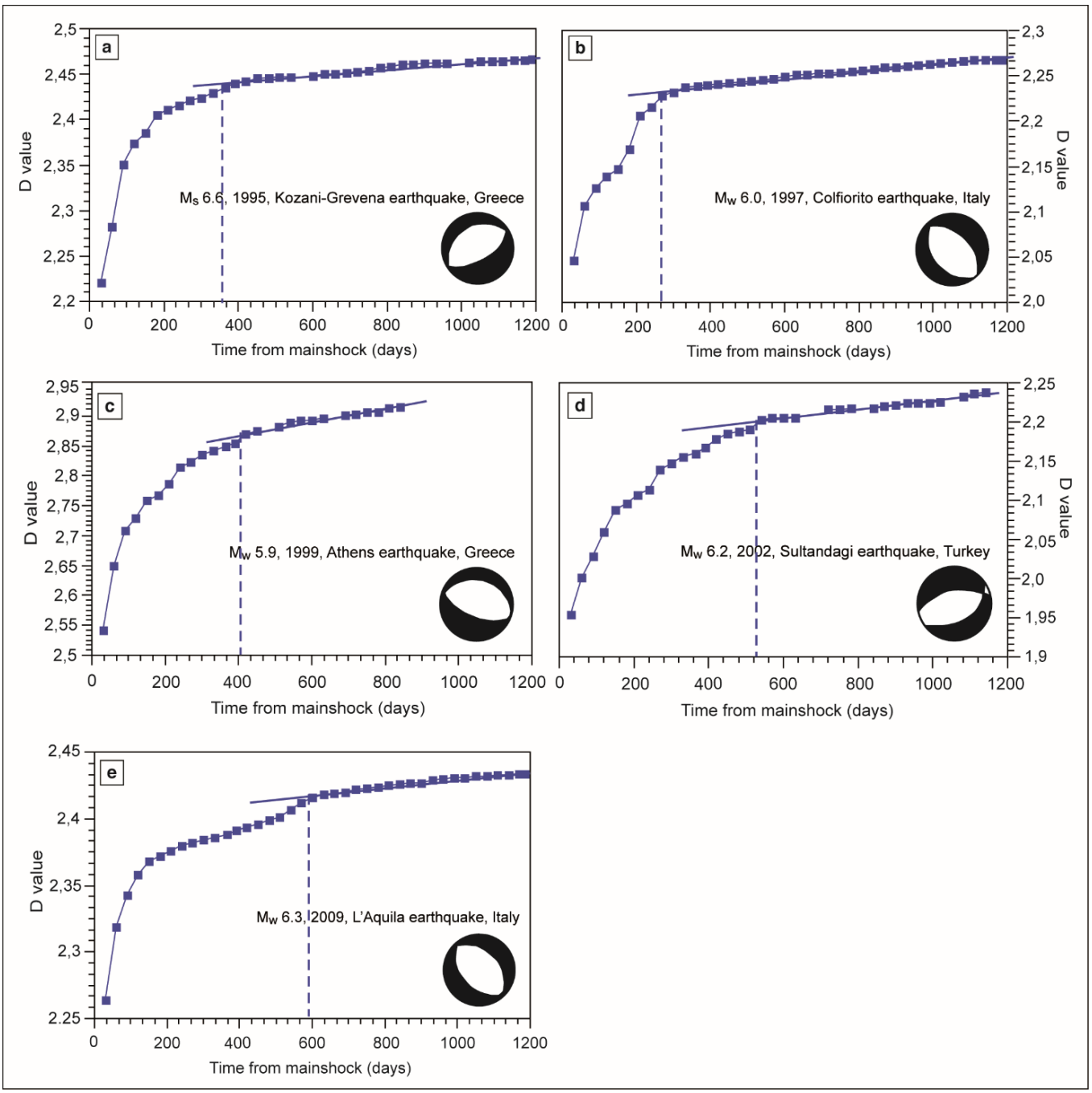

Figure 2.5. Mandelbrot method applied to extensional seismic sequences. Aftershock sequences temporal evolution analysed by using the Mandelbrot method and following five mainshocks nucleated in extensional areas: (a) the M_s 6.6 Kozani-Grevena earthquake (1995, Greece), (b) the M_w 6.0 Colfiorito earthquake (1997, Central Italy), (c) the M_w 5.9 Athens earthquake (1999, Greece), (d) the M_w 6.2 Sultandagi earthquake (2002, Turkey), and (e) the M_w 6.3 L'Aquila earthquake (2009, Central Italy). The fractal dimension (D) values are shown versus the days from the mainshock nucleation.

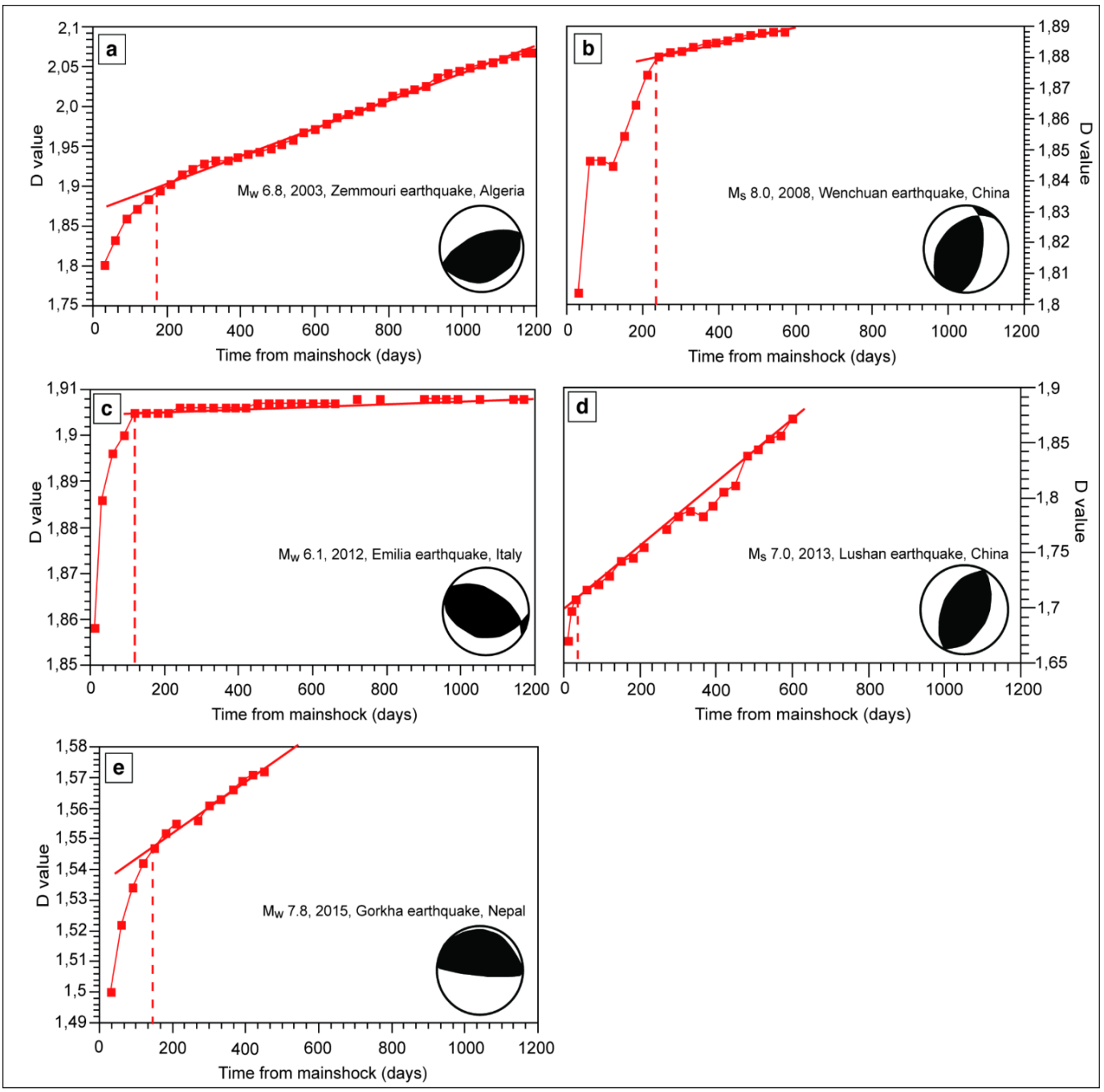

Figure 2.6. Mandelbrot method applied to compressional seismic sequences. Aftershock sequences temporal evolution analysed by using the Mandelbrot method and following five mainshocks nucleated in compressional areas: (**a**) the M_w 6.8 Zemmouri earthquake (2003, Algeria), (**b**) the M_s 8.0 Wenchuan earthquake (2008, China), (**c**) the M_w 6.1 Emilia earthquake (2012, Northern Italy), (**d**) the M_s 7.0 Lushan earthquake (2013, China), and (**e**) the M_w 7.8 Gorkha earthquake (2015, Nepal). The fractal dimension (D) values are shown versus the days from the mainshock nucleation.

2.3. Results

Hereafter, we briefly describe the selected seismic events and report the results achieved for the duration of the seismic sequences (Table 1).

2.3.1. Case studies of Extensional earthquakes

Kozani-Grevena earthquake (1995, Greece). On May 13rd, 1995 a M_s 6.6 earthquake struck the Kozani-Grevena region (northwestern Greece). This area is located on the western margin of the Internal Hellenides fold-thrust belt. This fold-thrust belt underwent extension since at least the Pliocene, which generated NE-SW to ENE-WSW-trending normal faults (Pavlides et al., 1995; Resor et al., 2005). The Kozani-Grevena mainshock occurred at 8.6 km depth along the ~8 km long Paleochori normal fault (Chiarabba and Selvaggi, 1997; Hatzfeld et al., 1997). According to the Tangents method, the sequence lasted about 300 days (Figure 2.2a). The mainshock was followed by 989 aftershocks with M≥2.5 (Figure A9a). The strongest aftershocks occurred on July 17th, two months after the M_w 5.3 mainshock. According to the Mandelbrot method the sequence lasted about 350 days, the fractal dimension (D) values vary from 2.22 to 2.47 (Figure 2.5a) and the R^2 is, on average, equal to 0.98 (Figures A6a and A8).

Colfiorito earthquake (1997, Central Italy). On September 26th, 1997 a M_w 6.0 earthquake struck the Northern Apennines region, in Central Italy (Ripepe et al., 2000; Chiaraluce et al., 2004). This area is located in the northern part of the Late Oligocene to present Apennines fold-thrust belt. Since middle Pliocene, the axial part of this fold-thrust belt underwent an extensional tectonics, which generated NW-SE-trending normal faults (Doglioni, 1991). The Colfiorito mainshock occurred at 7.5 km depth along the ~12 km long Mt. Pennino-Mt. Prefoglio normal fault (Amato et al; 1998; Ferrarini et al., 2015), which belongs to this extensional setting. According to the Tangents method the sequence lasted about 330 days (Figure 2.2b). The mainshock was followed by 2119 aftershocks with M≥2.5 (Figure A9b). The strongest aftershocks occurred October 6th and October 14th with M_w 5.4 and M_w 5.6, respectively. Furthermore, six months later, on April 3rd, 1998 another M_w 5.1 earthquake nucleated. According to the Mandelbrot method

the sequence lasted about 330 days, D varies from 2.05 to 2.27 (Figure 2.5b) and the R^2 is, on average, equal to 0.96 (Figures A6b and A8).

Athens earthquake (1999, Greece). On September 7th, 1999, a M_w 5.9 earthquake struck the city of Athens, in Greece. This area lies in between two Quaternary rift systems in central Greece: the Gulf of Corinth and the Gulf of Evia rifts (Ganas et al., 2004). E-W-trending and SW-dipping normal faults dominate the neotectonic structure of this region (Tselentis et al., 2000). The Athens mainshock occurred at 9.5 km depth along the ~15 km long Parnitha normal fault (Louvari et al., 2000; Papadimitriou et al., 2002; Baumont et al., 2004). The aftershocks activity was located at the eastern part of the activated normal fault16. According to the Tangents method, the sequence lasted about 300 days (Figure 2.2c). The mainshock was followed by 281 aftershocks with $M \geq 2.5$ (Figure A9c). The strongest M_w 4.8 aftershock occurred in the same day of the mainshock. According to the Mandelbrot method, the sequence lasted about 400 days, D varies from 2.55 to 2.93 (Figure 2.5c) and the R^2 is, on average, equal to 0.99 (Figures A6c and A8).

Sultandagi earthquake (2002, Turkey). On February 2nd, 2002 a M_w 6.2 earthquake struck the Sultandagi-Çay region of southwest Turkey (Ergin et al., 2009). This area is located in a complex geodynamic context, dominated by a series of graben and horst structures bounded by active oblique slip normal faults17. The main tectonic lineament of this region is represented by the undulated ~100 km long Sultandagi Fault, which trends primarily northwest (Emre et al., 2003). The Sultandagi mainshock occurred at 7 km depth17 along this fault (Ozer et al., 2007). According to the Tangents method, the sequence lasted about 500 days (Figure 2.2d). The mainshock was followed by 922 aftershocks with $M \geq 2.5$ (Figure A9d). The strongest aftershocks occurred two hours after the mainshock with M_w 5.6. According to the Mandelbrot method the sequence lasted about 540 days, D varies from 1.95 to 2.25 (Figure 2.5d) and the R^2 is, on average, equal to 0.9 (Figures A6d and A8).

L'Aquila earthquake (2009, Central Italy). On April 6th, 2009 a M_w 6.3 earthquake struck the Central Apennines region, in Central Italy (Chiaraluce et al., 2010; Valoroso et al.; 2013). The L'Aquila mainshock occurred at 8 km depth along the ~15–18 km long Paganica normal fault (Cinti et al., 2011). According to the Tangents method the seismic sequence lasted about 515 days (Figure 2.2e). The mainshock was followed by 915 aftershocks with M≥2.5 (Figure A9e). The strongest aftershock occurred on April 7th with M_w 5.4. According to the Mandelbrot method, the sequence lasted about 560 days, D varies from 2.26 to 2.44 (Figure 2.5e) and the R^2 is, on average, equal to 0.98 (Figures A6e and A8).

2.3.2. Case studies of compressional earthquakes

Zemmouri earthquake (2003, Algeria). On May 21st, 2003 a M_w 6.8 earthquake struck the coastal region east of Algiers and the Tell Atlas, in Algeria (Bounif et al., 2004). The Zemmouri mainshock occurred at 9 km depth along a NE-SW trending thrust (Deverchere et al., 2005), which is included in the thrust-and-fold Tell Atlas, in northern Algeria (Meghraoui et al., 2004). According to the Tangents method the sequence lasted about 100 days (Figure 2.3a). The mainshock was followed by 400 aftershocks with M≥2.5 (Figure A10a). The strongest aftershock occurred on May 27th, six days after the mainshock, with M_w 5.8. According to the Mandelbrot method the sequence lasted about 165 days, D varies from 1.8 to 2.05 (Figure 2.6a) and the R^2 is, on average, equal to 0.97 (Figures A7a and A8).

Wenchuan earthquake (2008, China). On May 12th, 2008 a M_s 8.0 earthquake struck the Sichuan Province, in central China. The main structural lineament of this area is located on the eastern edge of the Tibetan Plateau and is called the Longmenshan fault zone, which developed since Mesozoic time. This fault zone is about 500 km long, it dips to northwest and shows dextral transpressional kinematics; the fault system is composed by four main faults: the back thrust, the central thrust, the front thrust and the blind thrust (Fang et al., 2013). The Wenchuan mainshock occurred at 16 km depth along the central thrust (Xu et al.; 2008; Zhang et al., 2010). According to the Tangents method, the sequence lasted about 230 days (Figure 2.3b). The mainshock was followed by 1859 aftershocks with M≥2.5 (Figure A10b). The strongest aftershock occurred on May 25th, thirteen days after the mainshock, with M_w 6.3. According to the Mandelbrot method, the sequence lasted about 230 days, D varies from 1.8 to 1.89 (Figure 2.6b) and theR^2 is, on average, equal to 0.97 (Figures A7b and A8).

Emilia earthquake (2012, Northern Italy). On May 20th, 2012 a M_w 6.1 earthquake struck the Po Plain, in Northern Italy. This area hosts the northernmost part of the Late Oligocene to present Apennines fold-thrust belt (Scrocca et al., 2007). The Emilia mainshock occurred at 6.3 km depth along the 15 km long San Martino thrust (Bonini et al., 2014), which represents one of the active compressional structures buried under the Po Plain (Tizzani et al., 2013). According to the Tangents method, the sequence lasted

about 110 days (Figure 2.3c). The mainshock was followed by 782 aftershocks with M≥2.5 (Figure A10c). The strongest aftershock occurred on May 29th, nine days after the mainshock, with Mw 6.0, along the adjacent buried and seismogenic Mirandola thrust, at 10.2 km depth56. According to the Mandelbrot method the sequence lasted about 120 days, D varies from 1.86 to 1.9 (Figure 2.6c) and the R^2 is, on average, equal to 0.97 (Figures A7c and A8).

Lushan earthquake (2013, China). On April 20th, 2013 a M_s 7.0 earthquake struck again the Sichuan Province, in central China. The Lushan mainshock occurred five years after the Wenchuan earthquake along the same fault, at a depth of 15 km (Liu et al., 2013; Fang et al., 2013). According to the Tangents method the sequence was very short and lasted about 35 days (Figure 2.3d). The mainshock was followed by 122 aftershocks with M≥2.5 (Figure A10d). The strongest aftershock occurred few minutes after the mainshock with Mw 5.4. According to the Mandelbrot method the sequence lasted about 35 days, D varies from 1.67 to 1.87 (Figure 2.6d) and the R^2 is, on average, equal to 0.97 (Figures A7d and A8). I point out that, unlike the other case studies that show a typically curved trend, Figure 5d shows a linear trend of the temporal evolution of the fractal dimension. This anomalous behaviour is related to the seismic catalogue incompleteness. In particular, the catalogue doesn't include the seismic events with M< 3.0 and this could well justify the anomalous trend of the fractal dimension temporal evolution.

Gorkha earthquake (2015, Nepal). On April 25th, 2015 a M_w 7.8 earthquake struck Nepal (Feng et al., 2015). This region is inserted in the geodynamic context of the India-Eurasia collision. The Gorkha mainshock occurred at 15 km depth along the Main Himalayan Thrust (Parameswaran et al., 2015), a shallow dipping megathrust that accommodates most of the India–Eurasia convergence. The aftershocks sequence propagated eastwards from the mainshock (Prakash et al., 2016) and, according to the Tangents method, lasted about 130 days (Figure 2.3e). The mainshock was followed by 786 aftershocks with M ≥ 2.5 (Figure A10e). The strongest aftershock occurred about thirty minutes after the mainshock with M_w 7.1. According to the Mandelbrot method the sequence lasted about 130 days, D varies from 1.5 to 1.57 (Figure 2.6e) and theR^2 is, on average, equal to 0.96 (Figures A7e and A8).

2.4. The October 30th, 2016 M_w 6.5 Norcia earthquake case-study

The occurrence of the October 30th, 2016 M_w 6.5 Norcia earthquake has furnished another case-study to apply the abovementioned methods (i.e., Tangents and Mandelbrot methods) to an extensional seismic sequence. On October 30th, 2017, the M_w 6.5 Norcia earthquake struck the Central Apennines region, in Central Italy (Chiaraluce et al., 2017). The Norcia mainshock occurred at 7 km depth along the ~18 km long Monte Vettore fault system (Galadini and Galli, 2003). Other detailed information about the seismotectonic setting in which the M_w 6.5 Norcia earthquake occurred are reported in *Paragraph 3.2*.

We considered all the events nucleated after the Norcia mainshock in defined latitude and longitude ranges, in order to exclude the Campotosto sequence that occurred southernmost along the Campotosto extensional fault, since January 18th, 2017. In this case, we adopted a completeness magnitude (M_c) of 0.1, considering all the events ($0.1 \leq M_w \leq 6.5$) recorded in a time span included between the October 30th, 2016 and the June 30th, 2018. The existence of a complete seismological catalogue and the presence of a local and well-distributed seismometric network next to the epicentral area allow us to perform a very detailed analysis and to have indication of the temporal and spatial evolution of the fragmentation processes along the Monte Vettore fault system in time and space.

The performed analysis allows us to obtain some interesting results. According to the Tangents method, the sequence lasted about 500 days (Figure 2.7a). The mainshock was followed by more of 35000 aftershocks with $M \geq 0.1$. The strongest M_w 4.5 aftershock occurred few hours after the mainshock. According to the Mandelbrot method, the sequence lasted about 500 days, D varies from 2.2 to 2.62 (Figure 2.7b) and the R^2 is, on average, equal to 0.99 (Figures 2.7c).

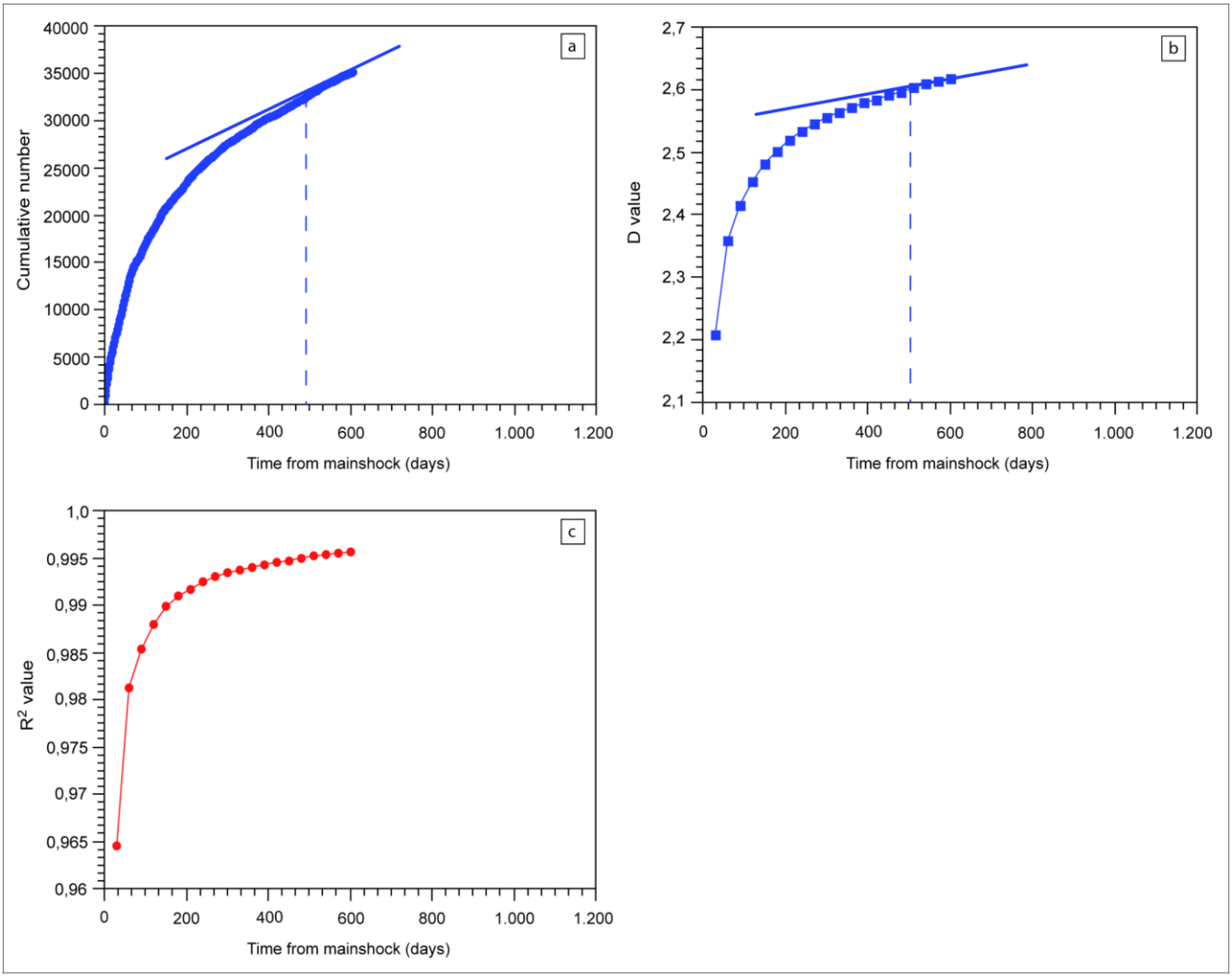

Figure 2.7. The October 30th M_w 6.5 Norcia earthquake case-study. (a) Aftershock sequences temporal evolution analysed by using the Tangents method; (b) Aftershock sequence temporal evolution analysed by using the Mandelbrot method; (c) R squared value temporal evolution in case of the Norcia seismic sequence.

Chapter 3

Ground Deformation and Source Geometry of the October 30th, 2016 M_w 6.5 Norcia Earthquake (Central Italy) Investigated Through Seismological Data, DInSAR Measurements and Numerical Modelling

3.1. Introduction

The crustal seismicity along the axial part of the Apennines belt (Central Italy) is mainly dominated by extensional faulting and is confined in the upper crust, apart from deeper events associated with a westerly directed subducting slab; conversely, the lower crust is rather seismically silent (Chiarabba et al., 2005). These characteristics are consistent with a shallower brittle crust and a deeper ductile crust, which are separated by the brittle-ductile transition (BDT) located at a depth of about 10 km, consistent with seismological observations (Petricca et al., 2015).

In the Central Italy extensional region, coseismic offsets produce predominantly subsidence of the fault hangingwall, with comparatively little uplift of both footwall and hangingwall blocks (Lavecchia et al., 2016; Cheloni et al., 2017). This observation was recognized in other regions (e.g., Thompson and Parson, 2017) and poses a problem in that a quantitative symmetry between coseismic uplift and subsidence does not occur. The October 30th M_w 6.5 Norcia earthquake (NEQ) is inserted in a seismic sequence that struck Central Italy since August 24th, 2016. This sequence was characterized by seismicity migration towards the north and by the consequent activation of several seismogenic structures. A wide literature already exists but, until now, a univocal point of view on the role played by the faults that caused the NEQ has not yet been reached (Cheloni et al., 2017; Liu et al., 2017; Pizzi et al., 2017; Xu et al., 2017; Scognamiglio et al., 2018). In particular, Cheloni et al. (2017) show, in addition to the SW dipping faults, the possible role played by: (i) a NE dipping normal fault antithetic to the Mt. Vettore Fault System (MVFS) and the Mt. Gorzano extensional fault (MGF) and illuminated by the aftershocks distribution; (ii)

a preexisting compressional low-angle structure, likely related to a segment of the Sibillini Thrust. Scognamiglio et al. (2018) proposed that a secondary rupture plane is necessary to fit their inversion of recorded ground-velocity waveforms and coseismic GPS displacements; moreover, a multi-fault source model is consistent with the deformation pattern resulting from DInSAR interferograms. Moreover, Scognamiglio et al. (2018) provides an interpretation of the unusual non-double couple component inferred from the moment tensor solution, which is anomalous if compared with other moment tensor solutions in this sector of the Apennines during the present and past seismic sequences.

In this work, we exploit seismological data and multi-orbit ALOS-2 DInSAR measurements to investigate the main effects due to the October 30th, 2016 NEQ, with particular emphasis given to the evaluation of the rock volumes affected by uplift and subsidence phenomena. Starting from the retrieved geodetic evidence we propose a numerical model of the NEQ based on the finite element method, implemented in a structural-mechanic framework and exploiting the available geological and seismological data, and the DInSAR-based ground deformation measurements.

3.2. Seismotectonic setting of the M_w 6.5 Norcia earthquake

The October 30th M_w 6.5 NEQ fits the tectonic setting of the Central Apennines fold-thrust belt and reflects extensional tectonics affecting this area since, at least, Pliocene time (Galli et al., 2008). These extensional tectonics, associated with the opening of the Tyrrhenian back-arc basin in the west (Doglioni, 1991), followed and replaced earlier compressional tectonics that formed the accretionary prism, presently shifted to east (western Adriatic Sea). Therefore, the active NW-SE-trending normal faults dissected the fold-thrust belt (Carminati et al., 2012) generating, over the centuries, earthquakes in the axial and western parts of the mountain belt (Chiaraluce, 2012). GPS data indicate that extension in the Apennines is not confined to the most elevated ridge, but is rather distributed all over the western side of the Italian peninsula, at least, down to the Tyrrhenian Sea coast. Avallone et al. (2016) show stretching at a rate of ~4 mm/yr between Rieti and Ascoli Piceno, resulting in a strain-rate of ~60 nanostrain/yr, consistent with available geological and seismotectonic information, and with the preliminary coseismic deformation observed through DInSAR measurements for the Amatrice earthquake (Lavecchia et al. 2016). This region has a record longer than 600 years of historical earthquakes and detailed constraints on the locations and slip rates of its active normal faults (Wedmore et al., 2017). The NEQ occurred in a seismic gap located between the 1997–98 Colfiorito sequence (M_w 5.7 and M_w 6.0; Chiaraluce et al., 2004) and the 2009 L'Aquila earthquake (M_w 6.3; Chiaraluce et al., 2011; Valoroso et al., 2013; Figure 3.1a). The whole sequence began with the M_w 6.0 Amatrice earthquake, nucleated on August 24th, 2016 activating the northernmost part of the SW-dipping MGF and the southernmost segment of the SW-dipping MVFS (Lavecchia et al., 2016; Figure 3.1a). Then, on October 26th, two seismic events, with M_w 5.4 and M_w 5.9 respectively, nucleated nearby Visso (Chiaraluce et al., 2017), activating the northernmost portion of the MVFS (Smeraglia et al., 2017). Finally, on October 30th the largest event of the sequence (M_w 6.5) occurred near the town of Norcia along the MVFS and hit the area included between the previous events (Figure 3.1b).

Moreover, a swarm of minor aftershocks began to affect the southernmost Campotosto area in December, 2016 and on January 18th, 2017 four seismic events ($5<M_w<5.5$) occurred along the Campotosto seismogenic fault (Falcucci et al., 2018).

Until now, more than 80000 earthquakes were recorded by the National Seismic Network (RSN) managed by the National Institute of Geophysics and Volcanology (INGV) in the whole area affected by this seismic sequence.

3.3. Data, analysis techniques and results

3.3.1. Seismological data

The NEQ activated a complex SW-dipping fault system. The principal involved structures are the MGF and the MVFS (Figure 3.1b), both characterized by extensional/transtensional kinematics and dissecting the heterogeneous clayey/marly to carbonatic sedimentary succession of the Umbria-Marche Apennines (Barchi et al., 2012). The MGF extensional fault is ~30 km long, dips ~60°–70° to the SW and accommodated a maximum down-dip displacement of ~2.3 km (Boncio et al., 2004); the MVFS is ~18 km long and consists of a series of SW-dipping (34–75°; Galadini and Galli, 2003). Moreover, the uplifted footwall block is not significantly affected by seismicity, whereas the uplifted area in the hangingwall block is bounded by a well-developed cluster of seismicity nearby the town of Norcia. In order to constrain the geometry and location of the tectonic structures involved during the NEQ, we take into account the relocated hypocentres (Chiaraluce et al., 2017) with $0.1 \leq M_w \leq 6.5$ that occurred between August 24th and November 29th, 2016 (Figure 3.1b), recorded by the INGV seismometric network. Specifically, once the relocated hypocentres are projected onto the sections, we was able to highlight three different geological structures (Figures 3.1c-f):

(i) a SW-dipping alignment parallel to the main fault system, characterized by principal faults striking N150°– 160° and dipping 45°–55°;

(ii) an E-dipping low-angle normal fault cutting through the upper crust; the relocated earthquakes highlight a flat structure which is located at most between about 8 and 10 km of depth and can also reach greater depths (down to about 12 km). This low-angle structure is the lower bound of the whole normal fault system, which is confined within the first 8 km of the upper crust, and coincides also with the lower limit of seismicity, the decollement surface;

(iii) ENE-dipping structures that are antithetic to the main fault.

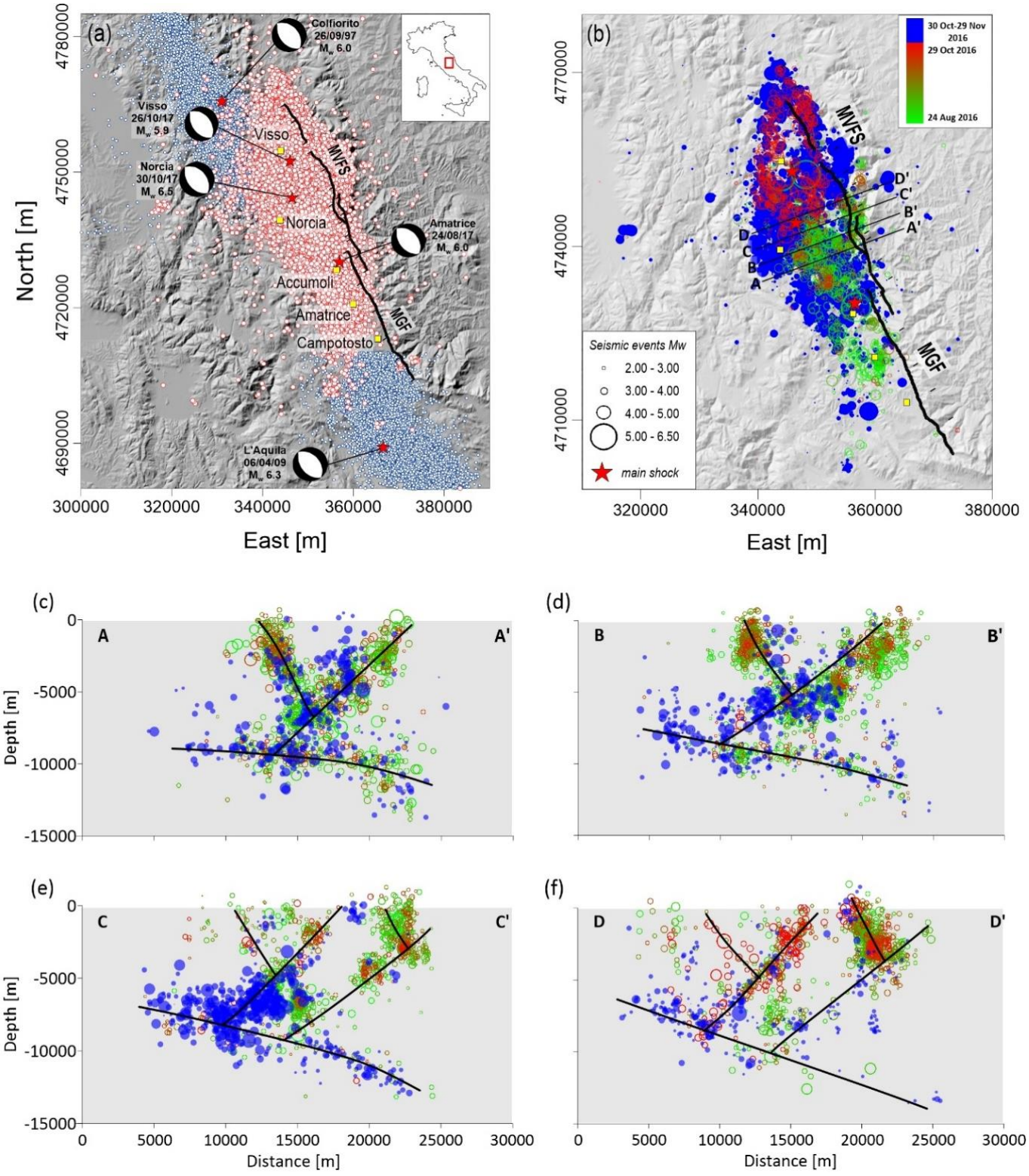

Figure 3.1. Seismological scenario. (a) Seismicity distribution in Central Italy recorded from August 24th to November 29th, 2016 (red circles) (Chiaraluce et al., 2017), superimposed on the 1 arcsec Shuttle Radar Topography Mission (SRTM) Digital Elevation Model (DEM) of the zone: the 1997-1998 Colfiorito and the 2009 L'Aquila seismic sequences are also shown (blue dots). The seismic events with $M_w \geq 5.4$ are represented by red stars and the associated focal mechanisms are also reported in the map. The black lines represent the main faults located in this

area: the Mt. Gorzano Fault (MGF) and the Mt. Vettore Fault System (MVFS); (b) Seismicity distribution as a function of magnitude (the higher the magnitude, the bigger the circles) and day of occurrence (from green to red circles). The seismic events with $M_w \geq 5.4$ are also indicated and are represented by red stars. The black lines represent the section profiles reported in panels b, c, d, e, in which the relocated hypocentres of the occurred earthquakes and the main inferred geological alignments (black lines) are projected.

3.3.2. DInSAR measurements

In order to compute the rock volumes involved during the nucleation processes of the NEQ, we focus on the analysis of the vertical displacements retrieved from the DInSAR measurements obtained through an appropriate phase unwrapping operation carried out on the generated differential interferograms (Costantini, 1998). We use two interferometric pairs acquired by the ALOS-2 system: the first was acquired along the ascending orbits on August 24th and November 2nd, 2016, respectively (Figure 3.2a and Table 3.1); the second was acquired along the descending orbits on August 31st and November 9th, 2016 (Figure 3.2b and Table 3.1), respectively. By combining the radar line-of-sight (LOS) displacements retrieved from the unwrapped interferograms obtained through these interferometric pairs, we compute (Manzo et al., 2006) the vertical and the E-W displacement maps of the coseismic ground deformations, respectively (Figures 3.2c-d).

Sensor	InSAR pair	Orbit	Wavelenght (cm)	Perpendicular baseline (m)	Track	Look angle (deg)
ALOS-2	24082016-02112016	ASC	24.2	99	197	36.6
ALOS-2	31082016-09112016	DESC	24.2	59	92	32.8
ALOS-2	24082016-06092017	ASC	24.2	99	197	36.6
ALOS-2	31082016-24052017	DESC	24.2	59	92	32.8

Table 3.1. Coseismic interferometric pair exploited for the DInSAR analysis. ALOS-2 data pairs involving both the October 26th Visso and the October 30th Norcia events.

In particular, the quantitative details about the retrieved vertical displacements, reported in Figure 3, are subsequently used for the rock volumes analysis. The map shown in Figure 3.2c displays four main patterns: (i) a major subsidence reaching its maximum value of about 98 cm near the epicentral zones nearby the town of Norcia; (ii) three smaller uplift zones, one lobe that affects the hangingwall block

(reaching maximum values of about 14 cm), a second one that affects the footwall block (reaching maximum values of about 10 cm) and an elongated easternmost deformation pattern (nearly parallel to the main Apennines structures; Figures 3.3b-e).

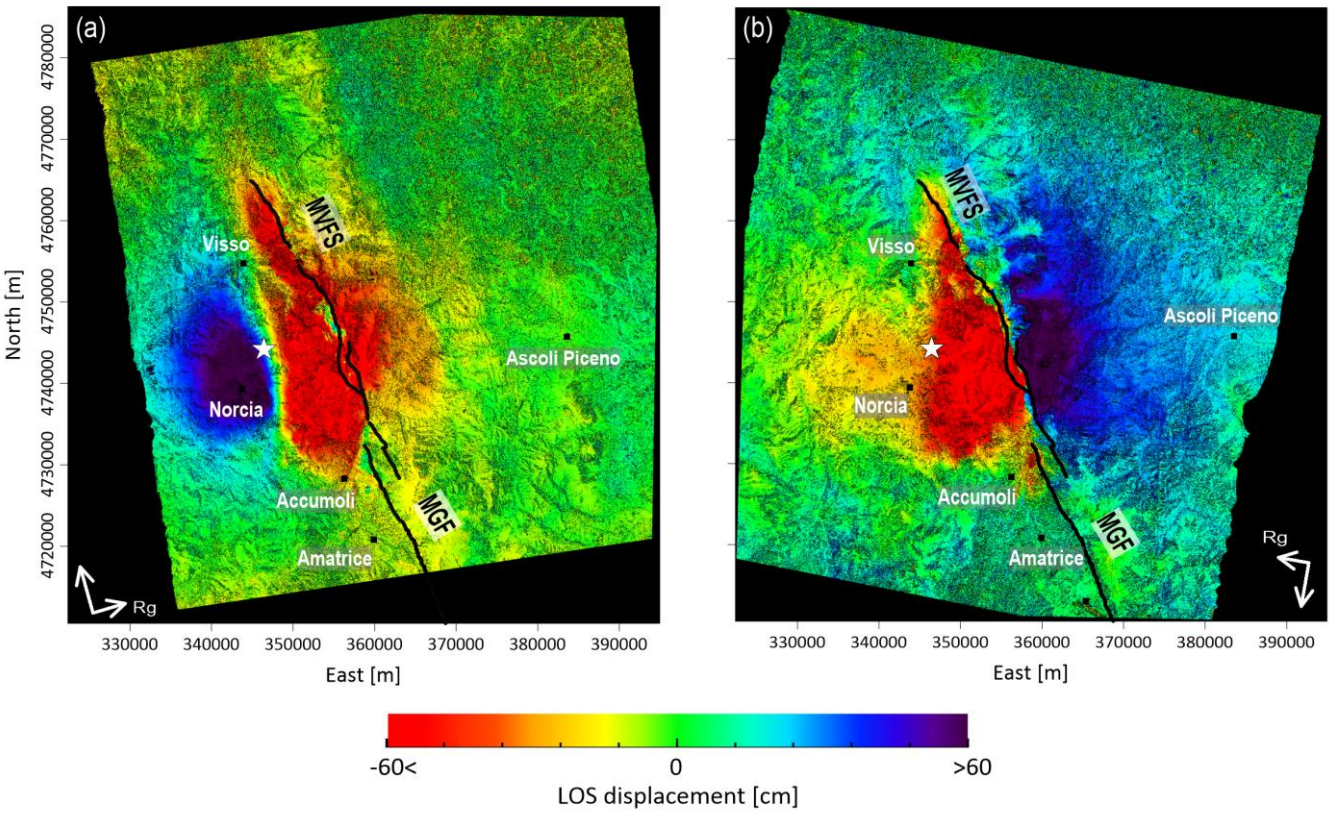
(a)
(b)
MVFS
MGF
Visso
Norcia
Accumoli
Amatrice
Ascoli Piceno
Rg
North [m]
East [m]
4720000
4730000
4740000
4750000
4760000
4770000
4780000
330000
340000
350000
360000
370000
380000
390000
-60<
0
>60
LOS displacement [cm]

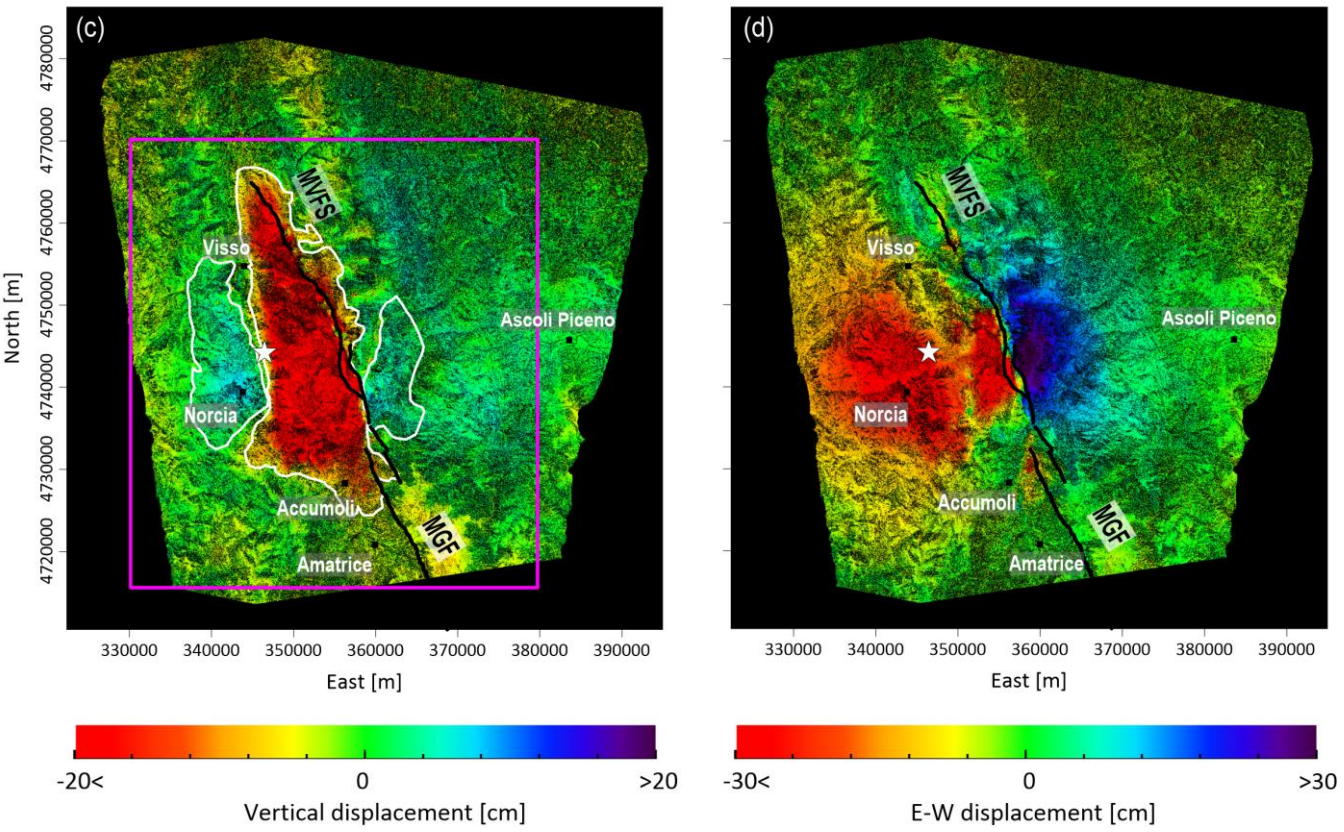
(c)
(d)
MVFS
MGF
Visso
Norcia
Accumoli
Amatrice
Ascoli Piceno
North [m]
East [m]
4720000
4730000
4740000
4750000
4760000
4770000
4780000
330000
340000
350000
360000
370000
380000
390000
-20<
0
>20
Vertical displacement [cm]
-30<
0
>30
E-W displacement [cm]

Figure 3.2. DInSAR analysis. (a-b) DInSAR (Line-of-sight [LOS]) displacement maps computed by using ALOS-2 images acquired from: (a) ascending orbits on August 24th-November 2nd, 2016 and (b) descending orbits on August 31st-November 9th, 2016; (c) vertical displacement map computed by exploiting the ascending and descending ALOS-2 measurements shown in panels a and b, and including both the M_w 5.9 Visso and the M_w 6.5 Norcia earthquakes. The magenta rectangle indicates the area considered in Figure 3a; (d) E-W displacement map computed by exploiting the ascending and descending ALOS-2 measurements shown in panels a and b, and including both the effect of the M_w 5.9 Visso and the M_w 6.5 Norcia earthquakes. The white star represents the M_w 6.5 Norcia mainshock. The white and black lines represent the contour lines of the maximum deformation zones and the main faults located in this area (i.e., MGF and MVFS), respectively.

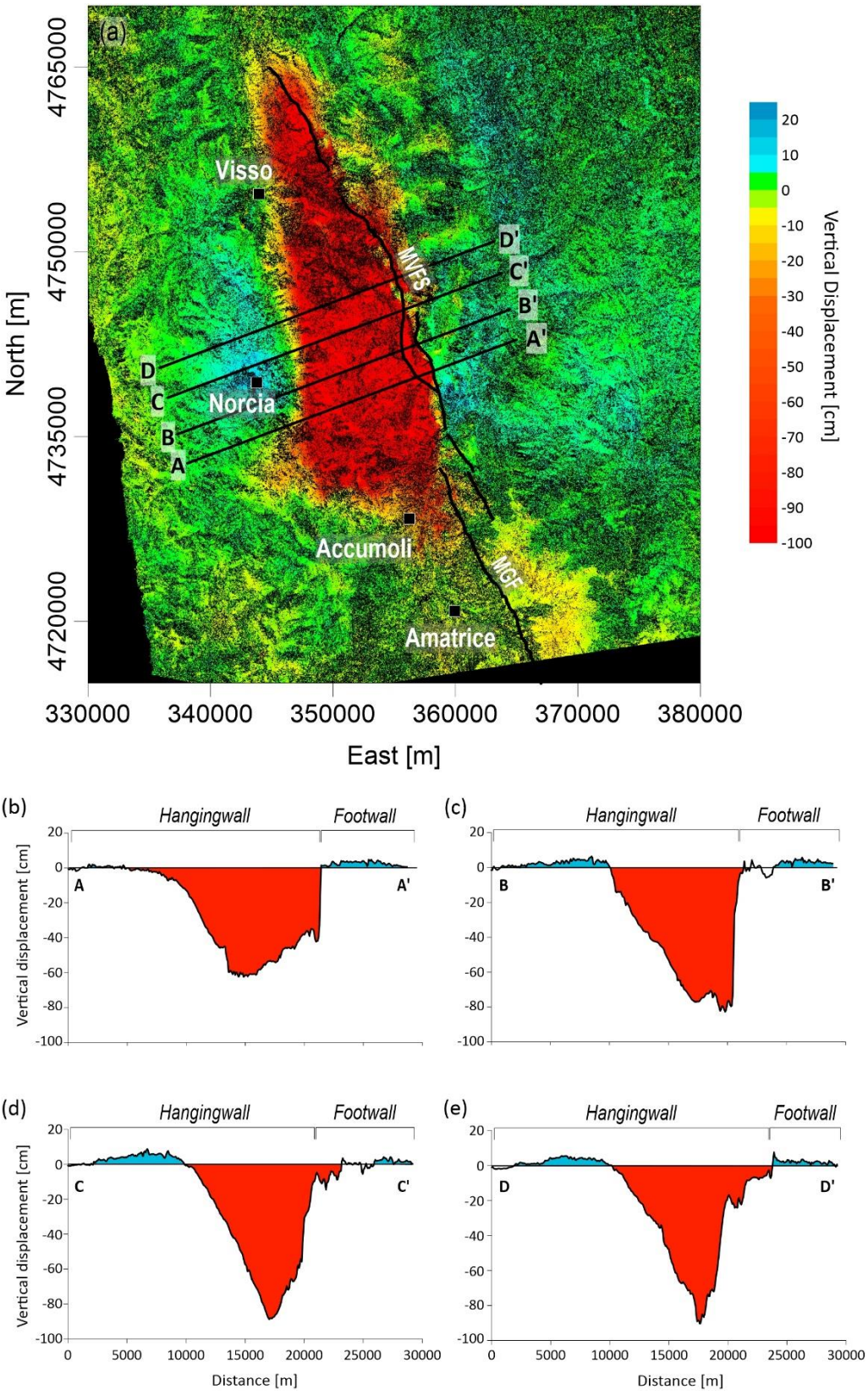

Figure 3.3. Vertical displacement analysis. (a) Vertical displacement map of Figure 3.2c with superimposed the black lines representing the main structural alignments located in this area. Moreover, the black lines represent the traces of the displacement profiles reported in panels b, c, d, e, in which the subsided and the uplifted volumes are highlighted in red and light blue, respectively.

To better discriminate the zones actually affected by ground deformation, we use two other interferometric pairs acquired by the ALOS-2 satellite. Specifically, one pair was acquired along ascending orbits on August 24th, 2016 and September 6th, 2017, respectively; the second pair was acquired along descending orbits on August 31st, 2016 and May 24th, 2017, respectively (Table 3.1). The analysis of this second data pair allows us to show that the elongated easternmost deformation pattern located in the footwall block is not clearly visible anymore (Figure 3.4); accordingly, we hypothesize that it is probably generated by atmospheric phase artefacts correlated with the topography of the area. Therefore, we consider that the ground surface affected by deformation phenomena are relevant to the central subsided area and the two adjacent uplifted lobes.

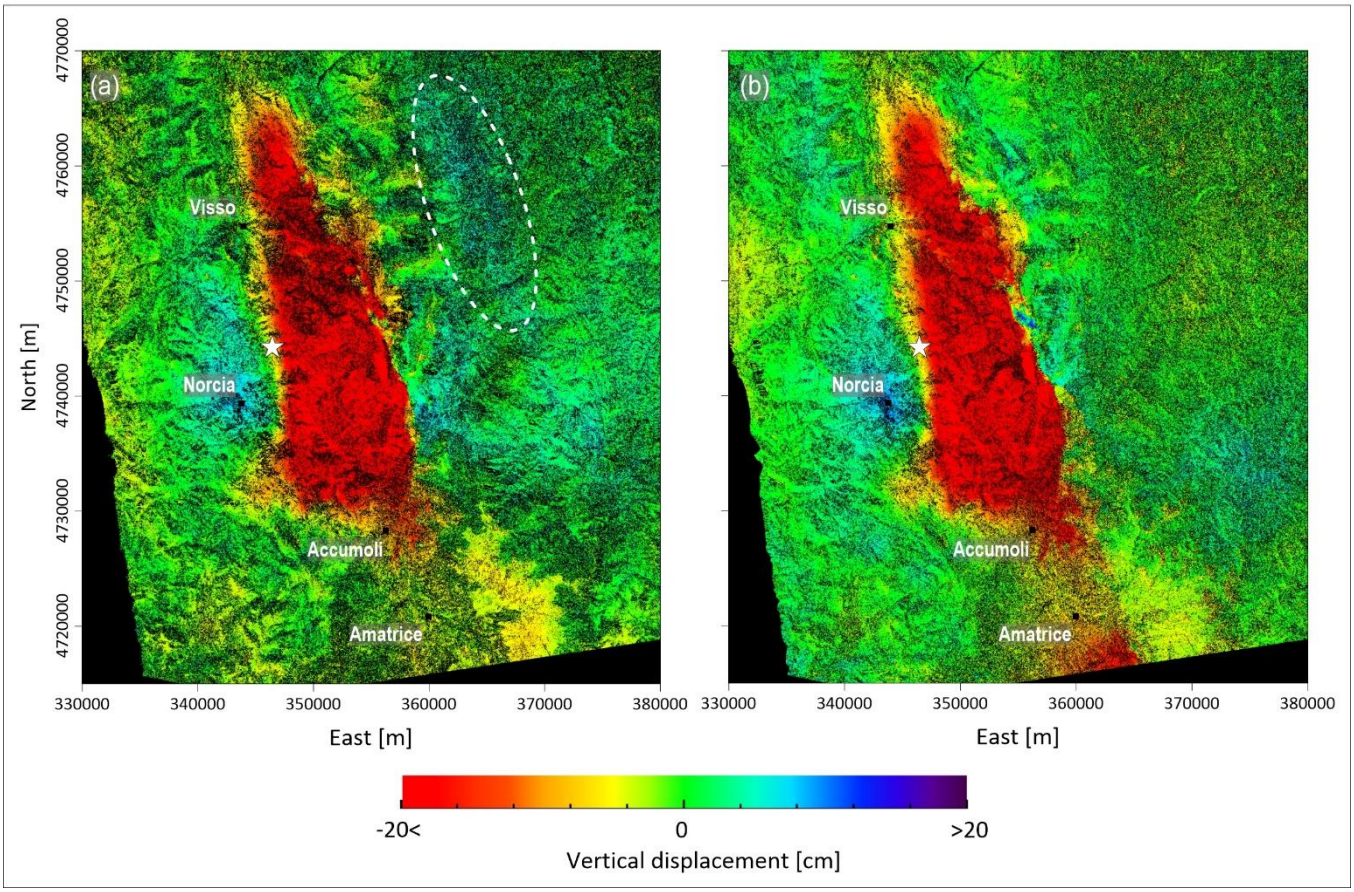

Figure 3.4. Comparison of vertical displacement maps. (a) Vertical displacement map shown in Figure 3.2a obtained through the combination of two DInSAR pairs: the first one was acquired by the ALOS-2 system along the ascending orbits on 24 August and 2 November 2016, respectively; the second was acquired along the descending orbits on 31 August and 9 November 2016; (b) Vertical displacement map obtained through the combination two DInSAR pairs: the first one was acquired by the ALOS-2 system along the ascending orbits on 24 August 2016 and 6 September 2017, respectively; the second was acquired along the descending orbits on 31 August 2016 and 24 May 2017. Both vertical displacement maps include the M_w 5.9 Visso and the M_w 6.5 Norcia earthquakes. The white star represents the M_w 6.5 Norcia mainshock. Note that, by comparing the maps in panels a and b, it is evident that the elongated easternmost deformation pattern (nearly parallel to the main Apennines structures) highlighted by the white dashed oval in panel a is not visible in panel b.

3.3.3. GPS data

The earthquake sequence occurred where several continuous and survey mode GPS networks were operating. In particular, several instruments were installed at geodetic benchmarks belonging to the Istituto Nazionale di Geofisica e Vulcanologia (INGV), CaGeoNet (Galvani et al., 2012), and to the Istituto Geografico Militare networks. Moreover, a new INGV continuous station was built at Arquata del Tronto. While the few coseismic offsets for the August 24th mainshock derived from continuous GPS data have been already described in Cheloni et al. (2016) and in Huang et al. (2017), the complete set of GPS displacements, from both permanent and survey mode stations, were presented in Cheloni et al. (2017) for the first time. The complex coseismic deformation pattern highlights a general SW-NE oriented extension, in agreement with the deformation field depicted by the DInSAR measurements. Maximum displacements (subsidence of ~17 cm and ~5 cm of horizontal movement toward southeast and southwest) were measured near Accumoli (ACCU, RIFP, and SLLI stations, respectively). Figures 3.5a-c show coseismic displacements related to the October 26th and 30th mainshocks. Due to a more limited number of GPS observations with respect to the Amatrice event, both the displacement fields (Figures 3.5a and b) show a sparser displacement pattern, characterized by a general SW-NE oriented extension in different portions of the MVFS. For the October 26th event, the maximum horizontal displacements were observed at stations FIAB and CAMP, which moved ~3 cm toward northeast and southwest, respectively (Figure 3.5a), while no significant vertical patterns were observed. As regards the October 30th NEQ, the largest horizontal displacements were observed at stations VETT and MSAN, with ~40 cm of movement toward northeast and ~25 cm toward southwest, respectively (Figure 3.5b). The largest vertical displacements were measured at sites RIFP, MSAN, and ARQT, with a subsidence reaching up to ~20–40 cm (Figure 3.5c). Finally, both stations 1322 and VETT, located on the footwall of the main normal fault system, showed an uplift of ~2–5 cm.

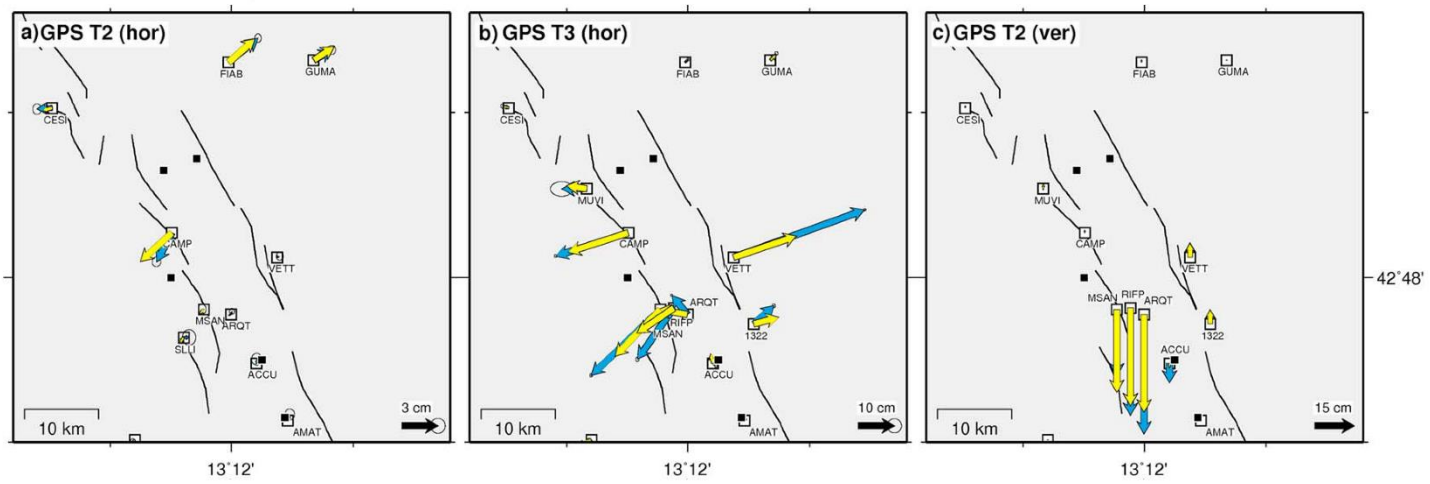

Figure 3.5. GPS measurements. (a-c) Observed (blue) and predicted (yellow) GPS horizontal displacements relative to the October 26th and 30th events, respectively; the vertical displacements are showed only for the latter event.

3.3.4. Geodetic modelling

The results of the inversion for slip distribution on the two fault planes corresponding to the activated segments of Mount Vettore normal fault system were obtained from the exploitation of a geodetic data set consisting of three ALOS-2 interferograms and of the GPS coseismic offsets for the October 26th and 30th events. In the modelling, the fault geometries were based on field data (Falcucci et al., 2016), focal parameters (http://cnt.rm.ingv.tdmt), and relocated aftershocks (Chiaraluce et al., 2017), along with the general strike of the MGF and MVFS. Two fault planes were considered, with ~160° strike and 20 × 4 km^2 size, which compose a 40 km long tectonic structure capturing almost the whole area affected by the October seismic sequence. The sensitivity of the RMS of the residuals to the overall fault dip was tested by performing a number of inversions varying the dip (within a range of 30°–60°) of the assumed fault planes. The retrieved data are consistent with a fault dip of ~40°, in agreement with previous findings by Lavecchia et al. (2016) and Huang et al. (2017) for the southern sector of the causative MVFS. The fault planes were subdivided into small patches, solving for slip and rake values on each patch. At shallow depth fault patches are about 1 × 1 km^2 wide, while the deeper ones are approximately 3.5 × 3.5 km^2. The preferred model satisfactorily reproduces the main characteristic of both the observed InSAR and GPS displacements. The October 30th M_w 6.5 NEQ ruptured the ~20 km long segment that had remained unbroken after the previous large events (Figure 3.6a-b). The mainshock occurred on the extensional MVFS, which was only partially activated in its southern portion during the August 24th earthquake. In this case, a main patch of slip (with peak slip up to >2 m) located at the centre of the fault plane (between 3 and 7 km depth) was found. The slip reaches the surface in the area where surface ruptures were observed (Galadini et al., 2017).

The model retrieves slip on the MVFS, which releases a seismic moment of 8.46 × 10^{18} Nm, equivalent to a M_w 6.59 earthquake. Most of the coseismic slip occurred on one main asperity (up to >2 m of slip) located updip of the hypocentre, between 3 and 7 km depth. In addition, some slip (up to ~1 m) is also required in the shallower portion of the plane, in correspondence to the observed surface breaks (Galadini et al., 2017), and in the deeper south-eastern part of the fault, which ruptured only a portion of the MVFS.

The results revealed that the assumption of slip occurring only on the two segments of the SW-dipping MGF and MVFS generates some displacement residuals (up to ~10 cm) in the 30 October coseismic interferograms, especially in the area of Norcia.

In order to better explain the displacement field imaged by these ALOS-2 interferograms, we hypothesized the occurrence of a further amount of slip on a secondary fault and explored two different hypotheses: (i) an antithetic NE-dipping extensional fault emerging in the Norcia area and well visible in the relocated aftershocks distribution (Figures 3.6c and d) and (ii) a pre-existing low-angle WNW-dipping thrust segment below the Castelluccio plain (Figures 3.6e and f). We found that, assuming additional slip on the antithetic fault or on the low-angle dislocation, the RMS for InSAR data decreases in both cases by ~10–15% and for GPS data by ~7–10% with respect to what was obtained modeling only the MGF and MVFS. Both the explored solutions (Figures 3.6c and e) show a main patch of slip located between 2 and 4 km depth, with maximum slip of ~0.7–0.8 m, equivalent to a M_w ~ 6.1–6.2 earthquake. The fact that no large aftershocks occurred around the two hypothesized ancillary faults suggests that the secondary dislocation may have slipped mostly aseismically.

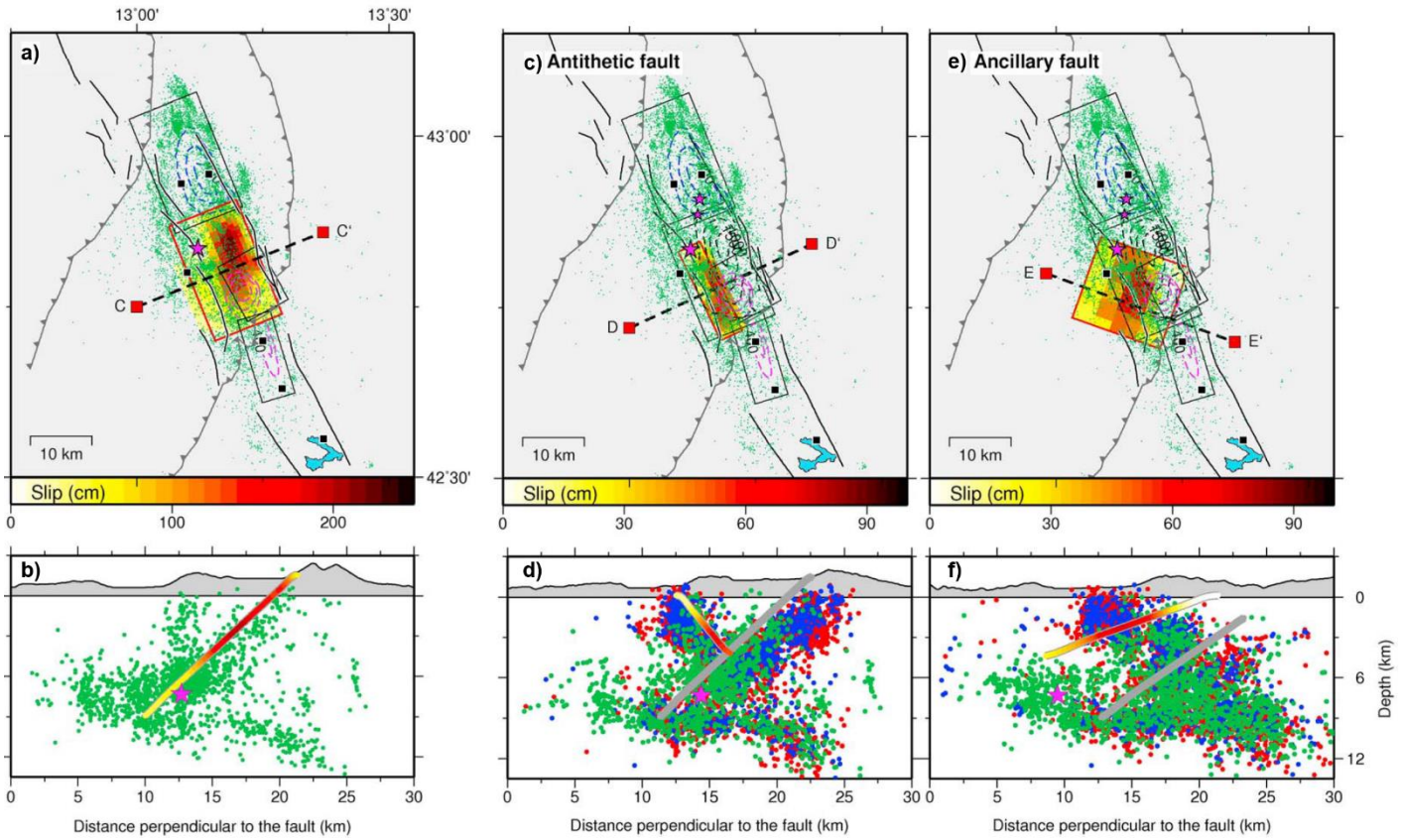

Figure 3.6. Geodetic model of the 30 October M_w 6.5 Norcia earthquake. (a-b) The October 30th Norcia coseismic slip distributions. Ancillary slip distributions assuming that normal slip occurred either on an (c and d) antithetic fault or on a (e and f) pre-existing compressional structure. Seismicity: purple stars indicate the main events; dots are relocated aftershocks (red = between August 24th and September 24th; blue = September 25th and October 25th; green = October 26th and November 30th).

3.4. Computation of uplifted and subsided volumes

We adopt three different methods to compute the uplifted and subsided volumes presented in the previous section: (i) the Topographic method (3D Cavalieri-Simpson modified method), (ii) the Numerical approach method and (iii) the Surfacing method. We prefer to use three methods in order to test the validity of the obtained volume values and, therefore, the differences among the calculated volumes are indicative of the accuracy of volume computations.

3.5.1. Topographic method (3D Cavalieri-Simpson modified method)

This method is useful for numerical integration by using quadratic polynomials to approximate the integrand on a sequence of intervals (Velleman, 2005). This mathematical law envisages subdivision of the integration interval into sub-intervals, in which the function is integrated through parabolic arches (i.e. through quadrangular polynomials). Specifically, we produce a uniformed regular matrix of the ground deformation displacement maps, considering the Nearest Neighbour geostatistical gridding method. This method assigns the value of the nearest point to each grid node and is useful when data are already evenly spaced. Alternatively, in cases where the data are nearly on a grid with only a few missing values, this method is effective for filling in the holes in the data. On this vertical displacement map, we trace 192 profiles that spatially include both the subsided and the uplifted zones (Figures 3.7a-c). These profiles are spaced 250 m apart and the spacing is selected taking into account the maximum horizontal gradient of the vertical component of deformation. We firstly calculate the areas by considering each profile and, subsequently, we compute the subsided and the uplifted volumes by multiplying the computed areas times the distances.

3.4.2. Numerical approach method

This method allows us to calculate automatically volumes by using the Surfer 15® tool (Golden Software). This software is able to realize this computational analysis considering solids defined by an upper surface and a lower one (we use again the Nearest Neighbour geostatistical gridding method) and employing three classical numerical integration algorithms (Press et al., 1988). In particular, these three mathematical methods can be recognized as:

1. the Extended Trapezoidal Rule, represented by the following formula:

$$Volume \approx \frac{\Delta y}{2}[A_1 + 2A_2 + 2A_3 + 4A_3 + \cdots + 2A_{nCol-1} + A_{nCol}] \quad (3.1)$$

where Δy is the grid row spacing and A is the area.

2. the Extended Simpson's Rule, represented by the following formula:

$$Volume \approx \frac{\Delta y}{3}[A_1 + 4A_2 + 2A_3 + 4A_3 + \cdots + 2A_{nCol-1} + A_{nCol}] \quad (3.2)$$

where Δy is the grid row spacing and A is the area.

3. the Extended Simpson's 3/8 Rule, represented by the following formula:

$$Volume \approx \frac{3\Delta y}{8}[A_1 + 3A_2 + 3A_3 + 2A_3 + \cdots + 2A_{nCol-1} + A_{nCol}] \quad (3.3)$$

where Δy is the grid row spacing and A is the area.

The difference in the volume calculations by three different methods measures the accuracy of the volume computations. We obtain very similar values and, therefore, we report in Table 3 the mean value obtained by using the abovementioned automatic approaches.

3.4.3. Surfacing method

The starting point of this method is the separation of the DInSAR measurements into negative and positive components of the vertical displacement. This analysis was performed in collaboration with Dr. Patrizio Petricca (Sapienza University). The two obtained datasets are smoothed over a regular grid by the surface routine of the software Generic Mapping Tools (Wessel et al., 2013) by solving:

$$(1 - T) * \nabla\big(\nabla(z)\big) + T * \nabla(z) = 0 \tag{3.4}$$

where ∇ indicates the Laplacian operator, z is the vertical displacement value and T is a tension factor between 0 and 1. T = 0 gives the minimum curvature solution and T=1 gives a harmonic surface (no maxima or minima are possible). We test all values for the T tension factor with no significant differences in obtained volumes, hence we hold T=0.5 as suggested in Smith and Wessel (1990) for steep topography data. We use a horizontal grid resolution of 5x5 cm even if results are stable increasing the grid resolution about one order. Two different surfaces, containing all positive (top smoothing surface) and negative (bottom smoothing surface) values respectively, are than defined (Figure 3.7d). Following, we select a subset of both datasets (positive/negative) by using location polygons enclosing uplifted and subsided areas respectively in both hangingwall and footwall of the main fault (magenta and blue shaded areas in Figure 3.7e). Considering a reference plane located at 0 cm elevation (Figure 3.7d) and measuring the volume between the reference plane and the top smoothing surface, and between the reference plane and the bottom smoothing surface respectively, we obtain the uplifted and the subsided volumes.

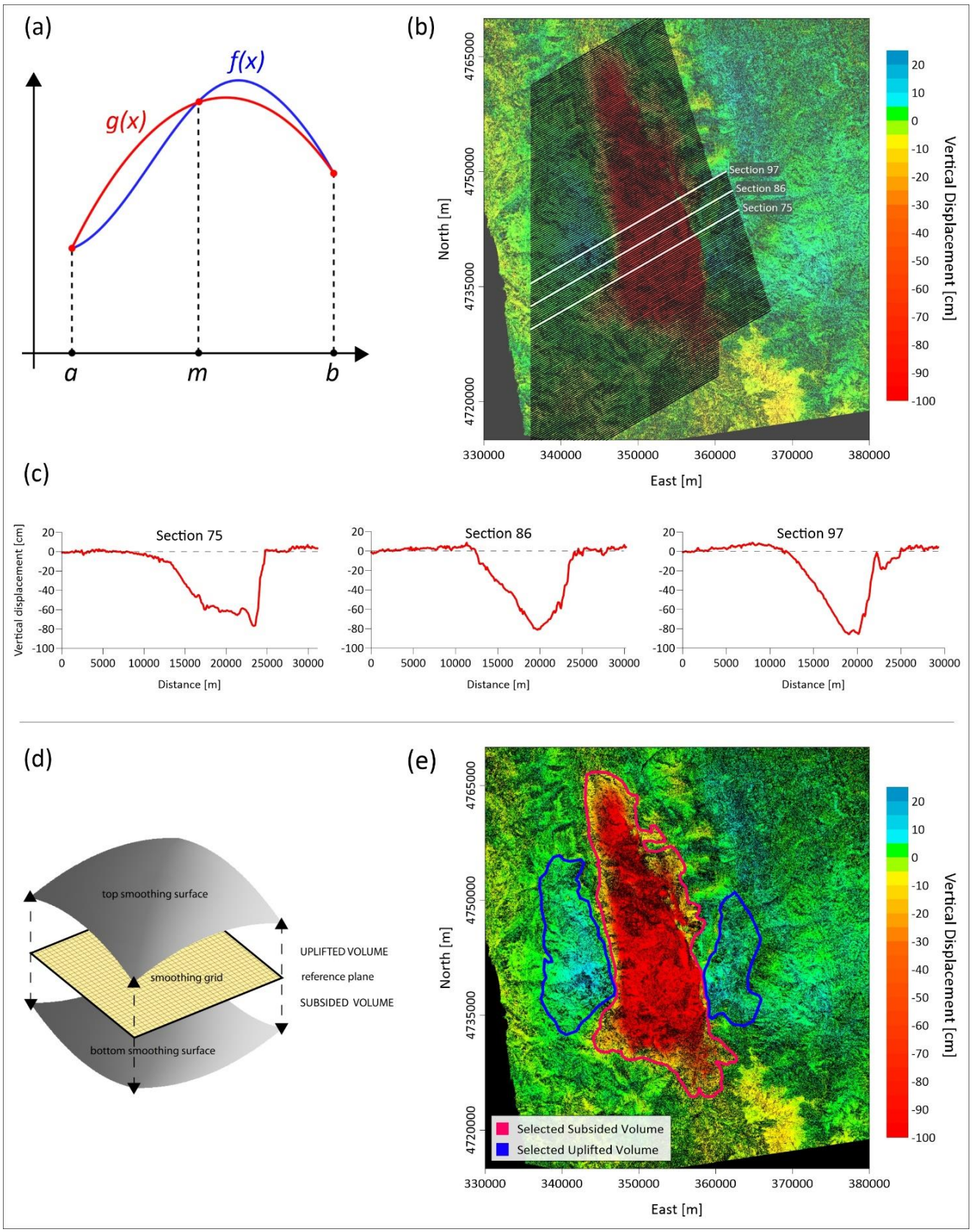

Figure 3.7. Volume retrieval methods. (a) Graphical representation of the Cavalieri-Simpson Rule; this method approximates the integral of the requested function (in blue) with that of the parabola that interpolates it in the nodes (in red); (b) Vertical component map in which the exploited 192 traced profiles are reported; (c) Examples of the

displacement profiles (in red) used for the volumes computation; (d) Graphic representation of the Surfacing Method. The employed routine is able to calculate the uplifted and subsided volumes, considering a reference plane located at 0 cm elevation and measuring the volume between the reference plane and the top smoothing surface, and between the reference plane and the bottom smoothing surface, respectively; (e) Vertical component map in which the polygons used for the computation of the subsided (in magenta) and uplifted (blue) volumes are shown.

3.4.4. Results

The DInSAR measurements show that during the NEQ, the hangingwall block was affected by broad subsidence with a maximum vertical amplitude of about 98 cm and by a significantly less extended region characterized by uplift (with a maximum of 14 cm); moreover, also the footwall block was affected by uplift (with a maximum of 10 cm; Figure 3.3b-e). The Topographic method shows that the NEQ was characterized by a subsided volume of 0.100 km^3 while the uplifted volume was 0.0070 km^3. By using the Numerical method, volumes of 0.101 km^3 and 0.0074 km^3 were calculated for subsidence and uplift, respectively. Finally, volumes of 0.101 km^3 and 0.0075 km^3 were obtained with the Surfacing method for subsidence and uplift, respectively. The very similar values obtained with these methods assesses the reliability of our results. In addition, we remark that the subsided and uplifted rock volumes are markedly different and the deficit (i.e., the difference between subsided and uplifted volumes) is 0.0930 km^3, 0.0936 km^3 and 0.0935 km^3 for the Topographic, Numerical and Surfacing methods, respectively (Table 3.2).

Deformed volume [km^3]	**Topographic method**	**Numerical approach method**	**Surfacing method**
Subsidence	0.100	0.101	0.101
Uplift	0.0070	0.0074	0.0075
Unbalance	0.0930	0.0936	0.0935

Table 3.2. Computed volumes values. Results obtained by employing the three abovementioned methods.

3.5. Numerical modelling

The results presented in the previous section clearly highlight an unbalance between the subsided and the uplifted volumes. To provide a possible interpretation of this volumetric asymmetry, we propose a 2D numerical model of the NEQ based on the finite element method and implemented in a structural-mechanic framework (Figures 3.8 to 3.11); our approach is based on the linear elasticity and on the plain strain approximation mode to minimize the differences between the modeled vertical displacements and those retrieved through the DInSAR analysis (Tizzani et al., 2013; Castaldo et al., 2018). In particular, in the considered numerical environment we exploit the a priori available geological and structural information and the seismicity distribution relevant to the investigated seismogenic area, to take into account the mechanical heterogeneity and the active alignments that characterize the upper crust in the Apennines chain. According to Tizzani et al. (2013), we evolve the model through two stages: during the first one (interseismic), the model compacts under the weight of the rock successions (gravity loading) until it reaches a stable equilibrium. At the second stage (co-seismic), where the stresses are instantaneously released through a no uniform slip along the faults, we use an iterative procedure based on a trial-and-error approach (Tarantola, 2005). Starting from the geometry of the ground deformation pattern (see Figure 3.2) and to ensure the most representative section of this seismogenic area, we choose as a reference profile section BB' (see Figures 3.1d and 3.3c) reported in the maps of Figures 3.1b and 3.3a. In this context, we build up a simplified geometry of the study region, which extends for about 100 km, with a depth of 26 km; such a large zone, with respect to the co-seismic epicentral region, allows to reduce edge effects to negligible (Figures 3.8a and 3.10a). Concerning rheology, we develop a heterogeneous model by considering two geological units having isotropic mechanical properties: (A) the Umbria-Marche carbonate sedimentary succession, (B) the evaporitic layer and basement unit (Figures 3.8a and 3.10a) and a carbonate fractured unit (C in Figure 3.10a). The considered elastic parameters values are reported in Table 3.3 (Schön, 2015).

Parameters	Unit A	Unit B	Unit C
Density	2600	2700	2300
Young's Modulus	30	30	9
Poisson's Ratio	0.33	0.32	0.27

Table 3.3. Considered elastic parameters values. Parameters for each layer defined in the model: Density (kg/m^3), Young's Modulus (GPa) and Poisson's Ratio.

To simulate the possible structural frameworks of the investigated area, we define two possible opposite scenarios: (i) a single SW-dipping fault; (ii) a single SW-dipping fault with an antithetic zone.

3.5.1. Single fault

This scenario consists of a single SW-dipping fault and of a low-angle E-dipping fault (Figure 3.8a). As boundary conditions, we adopt a free boundary at the Earth surface, whose geometry is constrained by the topography of the considered area. A roller condition at the two sides and at the bottom boundary of the numerical domain is applied. In addition, we assume specific internal boundary settings for the main structural alignments pattern in order to simulate the tectonic contacts among the achieved structural domains. Gravity is applied as a body force to all the elements and a constant density of 2600 kgm^{-3} is assigned to all the elements of Unit A, whereas a density of 2700 kgm^{-3} is assigned to Unit B (Table 3.3). The behaviour of the SW-dipping fault is modelled as a contact body with frictional forces, while the low-angle east-dipping seismogenic layer as roller constraints. Moreover, we apply a couple of forces to the two sides of the main SW-dipping fault (the considered fault segment is 8 km long); the forces applied to the internal and external sides of the fault surfaces are equal to 3.4 MPa and 2.3 MPa, respectively. The entire numerical domain is discretized in 17,226 tetrahedral elements with a higher refinement along the two main faults (Figure 3.8b). In order to reproduce the coseismic displacement along the fault, we assume stationarity and linear elasticity of the involved materials by considering the solution of the equilibrium mechanical equations (Fagan, 1992).

The retrieved best fit model, evaluated by considering the achieved minimum RMS value of the residuals (i.e., the difference between measured and modelled displacements), is reported in Figure 3.9a for the vertical deformation component. The performed solution, accounting also for the topography of the considered area, does not show a good spatial fit with the observed ground deformations, both in terms of shape and amplitude of the residual signal. In particular, the performed misfit analysis revealed rather high RMS values for the achieved residuals of the ALOS-2 DInSAR measurements (RMS = 12,42 cm).

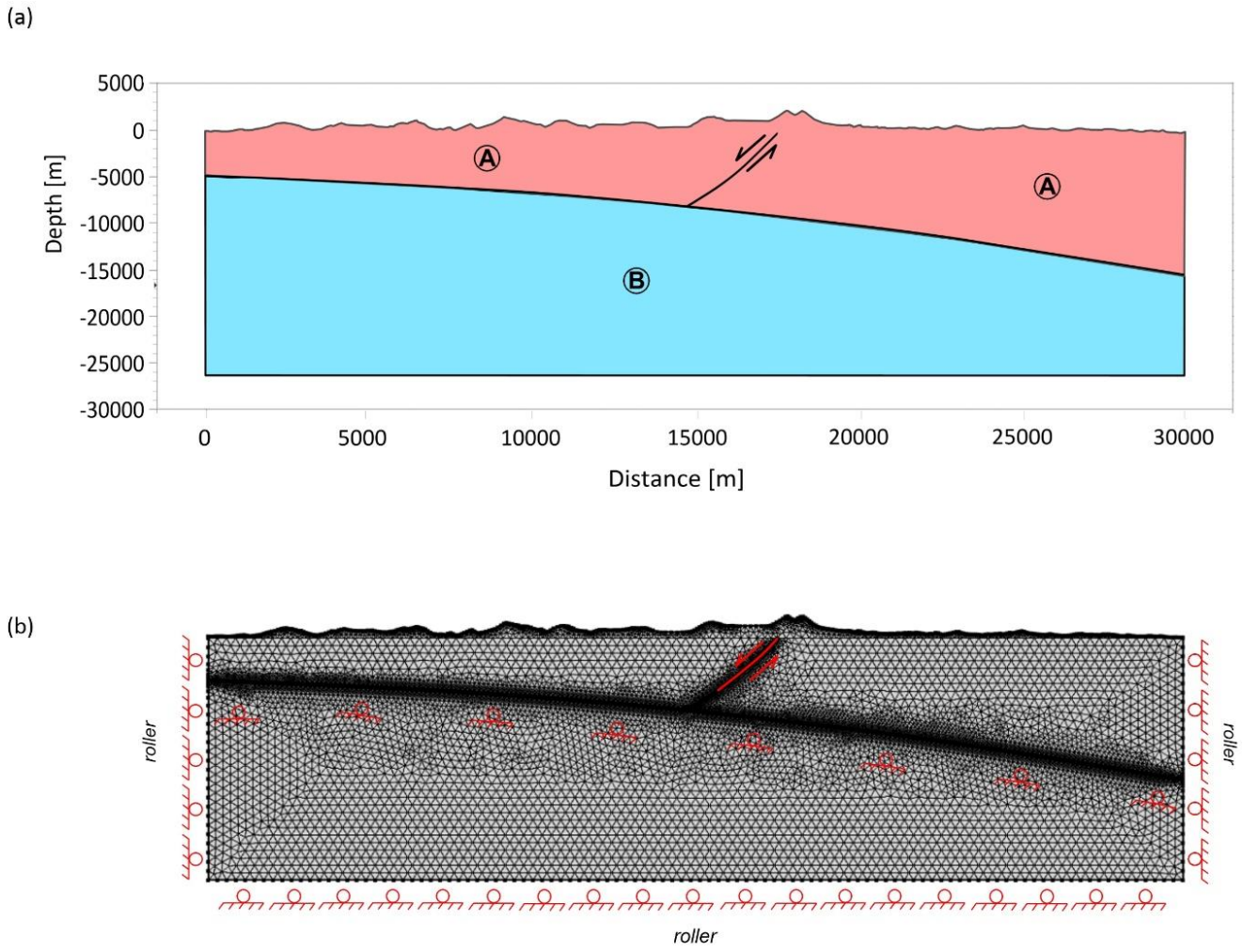

Figure 3.8. Single fault model setup. (a) Simplified geological cross-section (BB' reported in Figures 1d and 4c) exploited in the considered FE environment; (b) Discretized numerical domains with highlighted the boundary conditions; note that the red line represent the segments along which the forces are applied.

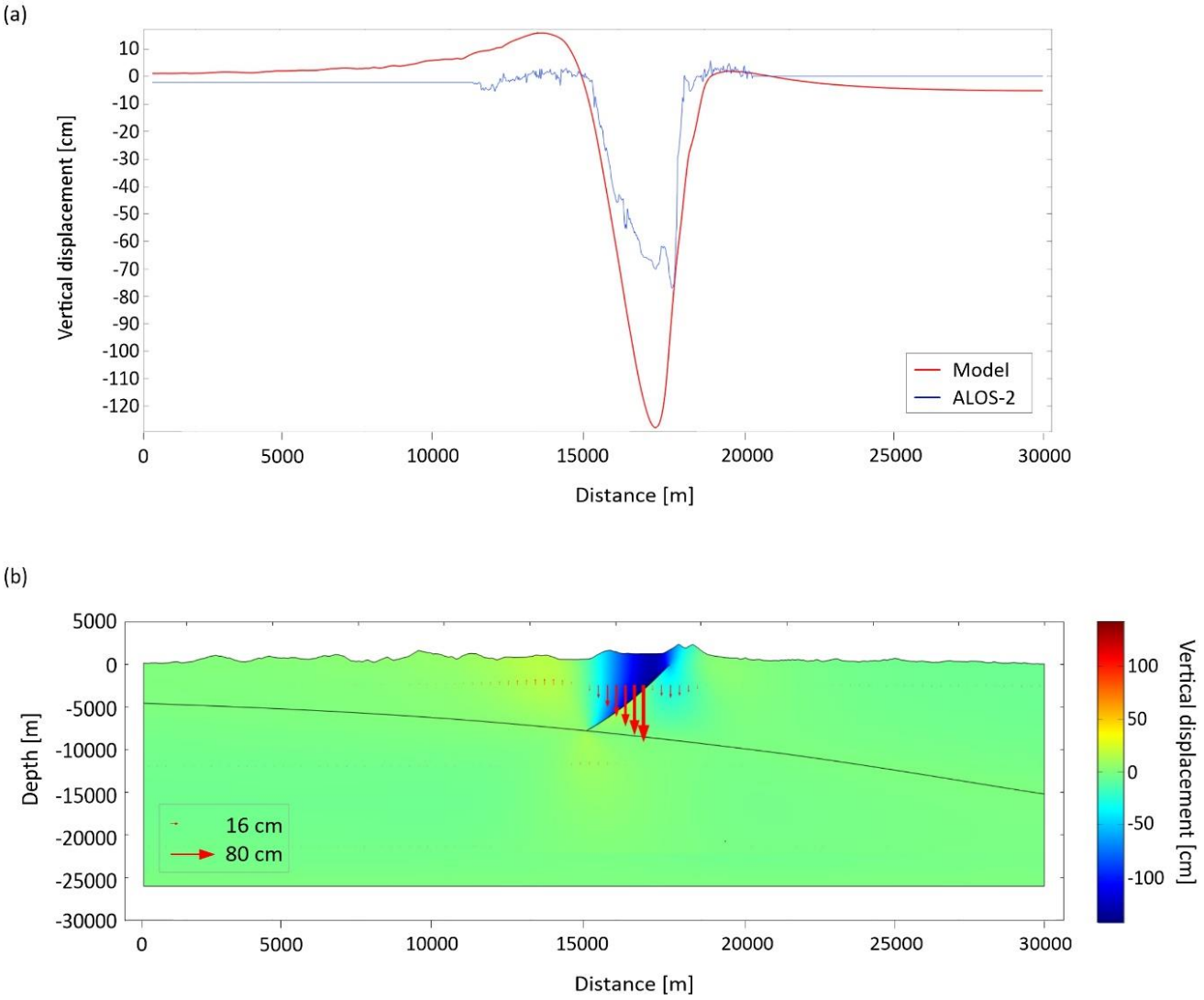

Figure 3.9. Results of the single fault model. (a) Comparison between the vertical component of the deformations retrieved through the DInSAR analysis and the FE modelling; (b) Crustal distribution of the modelled vertical components of the retrieved displacements; the red arrows indicate the modelled displacement vectors.

3.5.2. Role of the antithetic zone

This scenario consists of a single SW-dipping fault, of an antithetic fractured zone and of a low-angle E-dipping fault (Figure 3.10a). As boundary conditions, we adopt a free boundary at the Earth surface, whose geometry is constrained by the topography of the considered area. A roller condition at the two sides and at the bottom boundary of the numerical domain is applied. In addition, we assume specific internal boundary settings for the main structural alignments pattern in order to simulate the tectonic contacts among the achieved structural domains. Also in this case, gravity is applied as a body force to all the elements. A constant density of 2600 kgm^{-3} is assigned to all the elements of the Unit A, whereas density values of 2700 kgm^{-3} and 2300 kgm^{-3} are assigned to the Units B and C, respectively (Table 3.3). The behaviour of the SW-dipping fault and of the antithetic zone is modelled as a contact body with frictional forces, while the low-angle east-dipping seismogenic layer as roller constraints. Moreover, we apply a couple of forces to the two sides of the main SW-dipping fault (the considered fault segment is 8 km long); the forces applied to the internal and external sides of the fault surfaces are equal to 3.4 MPa and 2.3 MPa, respectively. The entire numerical domain is discretized in 17,768 tetrahedral elements with a higher refinement along the three main structures (Figure 3.10b). In order to reproduce the coseismic displacement along the fault, we assume stationarity and linear elasticity of the involved materials by considering the solution of the equilibrium mechanical equations (Fagan, 1992).

Our best fit model, relevant to the minimum RMS value, is reported in Figure 3.11a for the vertical deformation component. The achieved solution accounting also for the topography of the considered area, shows a very good fit with the observed ground deformations, both in terms of shape and amplitude of the residual signal. In particular, the performed misfit analysis revealed rather small RMS values for the achieved residuals of the ALOS-2 DInSAR measurements (RMS = 3,48 cm).

(a)

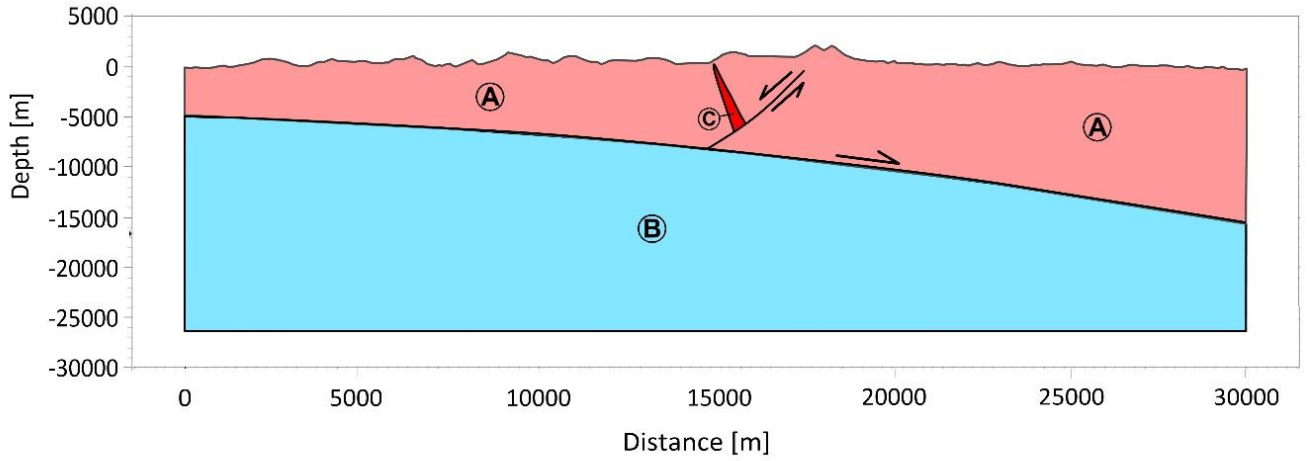

(b)

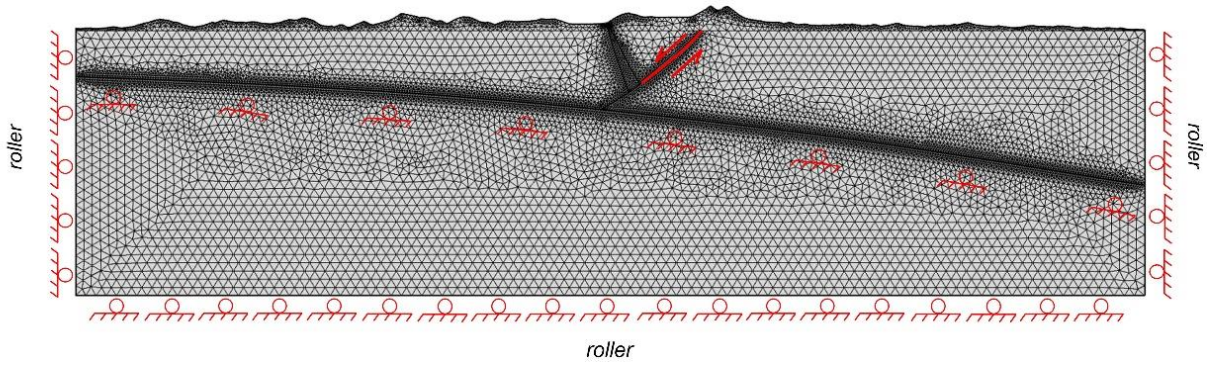

Figure 3.10. SW-dipping fault and antithetic zone model setup. (a) Simplified geological cross-section (BB' reported in Figures 1d and 4c) exploited in the considered FE environment; (b) Discretized numerical domains with highlighted the boundary conditions; note that the red line represent the segments along which the forces are applied.

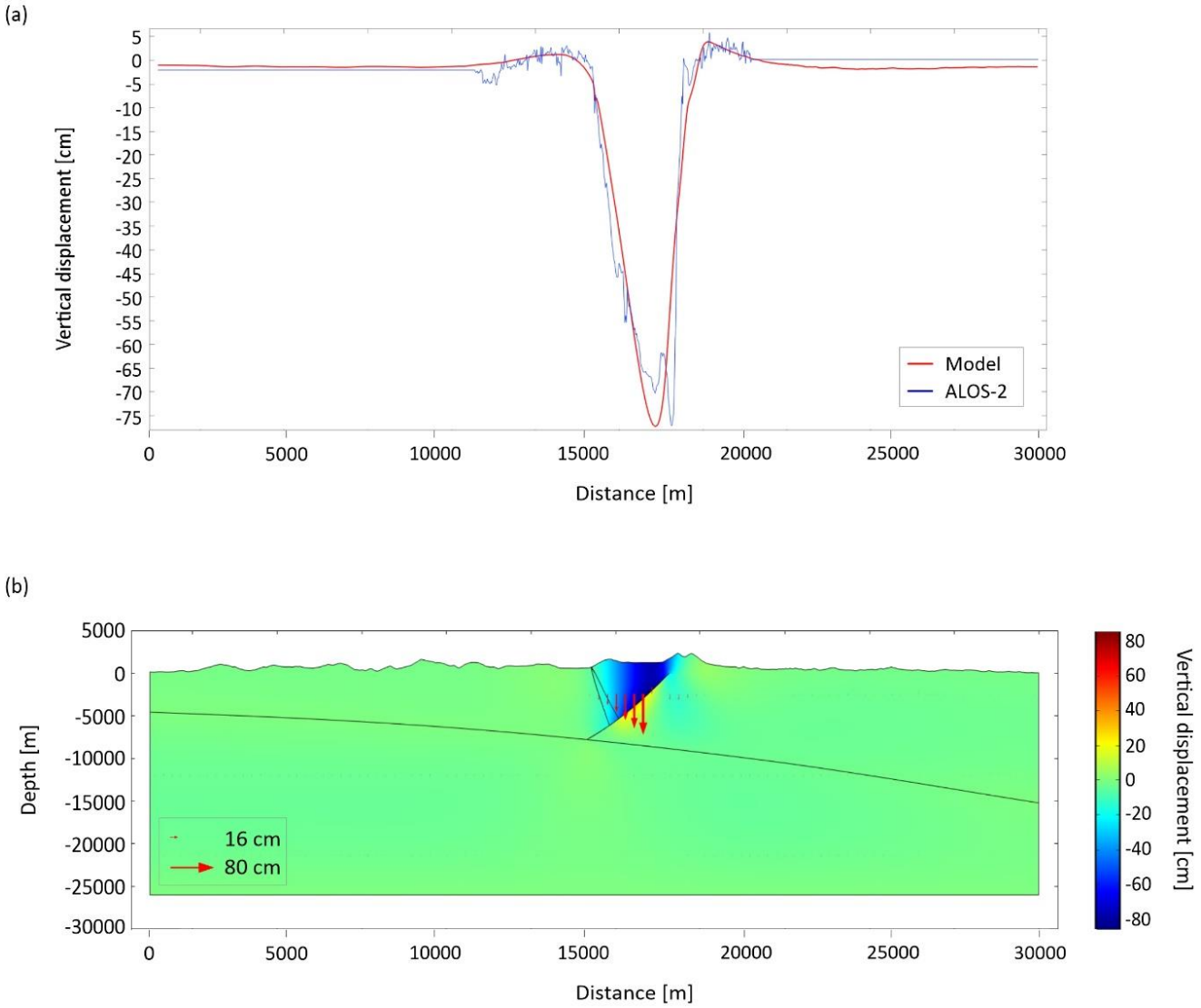

Figure 3.11. Results of the SW-dipping fault and antithetic zone model. (a) Comparison between the vertical component of the deformations retrieved through the DInSAR analysis and the FE modelling; (b) Crustal distribution of the modelled vertical components of the retrieved displacements; the red arrows indicate the modelled displacement vectors.

Chapter 4

Discussion

4.1. On the aftershock sequences duration

The Tangents and Mandelbrot methods provide comparable durations for each seismic sequence (Table 1), also including the M_w 6.5 Norcia earthquake. The analysis of these sequences highlights the relationships between the aftershocks decay and the tectonic settings in which the seismic sequences occurred:

i) According to the Tangents method, the average duration of aftershock sequences within extensional and compressional tectonic settings are about 390 days and 120 days, respectively; extensional sequences are thus 270 days longer than compressional ones (Figures 2.2 and 2.4). Aftershock sequences within extensional tectonic settings comprise more seismic events (1045 aftershocks on average) than sequences within compressional earthquakes (790 aftershocks on average). Surprisingly, a M_w 6.0 extensional earthquake (i.e., Colfiorito earthquake, 1997, Italy) is characterized by a longer aftershocks sequence duration than a M_s 8.0 compressional earthquake (i.e., Wenchuan earthquake, 2008, China).

ii) According to the Mandelbrot method, the average duration of aftershock sequences within extensional tectonic settings is about 430 days, 295 days longer than that of aftershock sequences within compressional tectonic settings (about 135 days; Figures 2.5 and 2.6). Furthermore, extensional aftershock sequences comprise more seismic events (1056 aftershocks on average) than those within compressional earthquakes (795 aftershocks on average). The fractal dimension (D) values calculated for extensional and compressional sequences are also different. D varies between ca. 2–3 and ca. 1–2 for extensional and compressional earthquakes, respectively. As the fractal dimension is indicative of the geometrical fragmentation process, with time extensional seismic sequences are thus spatially distributed within a volume, while compressional seismic sequences closer to a fault along a surface. The average coefficient

of determination R-squared (or R^2) is, greater than 0.95 for nine seismic sequences (i.e., the 1995 Kozani-Grevena, the 1997 Colfiorito, the 1999 Athens, the 2009 L'Aquila extensional sequences and the 2003 Zemmouri, the 2008 Wenchuan, the 2012 Emilia, the 2013 Lushan and the 2015 Gorkha compressional sequences) and equal to 0.90 for the 2002 Sultandagi extensional sequence. These high R^2 values indicate that the collected seismological data and the derived results are robust.

These analyses strongly support the conclusion that, irrespective of the magnitude of the mainshocks, extensional seismic sequences are longer than compressional sequences. We propose that the type of energy released during the earthquakes, in turn related to the tectonic setting, controls the different duration of seismic sequences. The observed variability of the duration of aftershock sequences, however, could be conditioned by rock properties and fault characteristics. Doglioni et al. (2015a) proposed that single extensional seismic sequences dissipate gravitational energy (Figure 4.1a) stored during the interseismic phase, within a hangingwall volume confined by the main normal fault and an antithetic fractured dilated zone. When the stresses related to this gravitational energy exceed the strength of the dilated zone and of the main normal fault, the rock volume collapses slipping along the main fault, generating the earthquake (Petricca et al., 2015; Figure 4.1a). The downward hangingwall block movement is favoured by gravity. This induces an increase of potential energy and facilitates fracturing processes both during the pre-seismic period and the coseismic phase. The potential energy is transformed into kinetic energy as indicated by the double-couple mechanism of the earthquakes generated by the shear on the fault planes. In this case, most of the involved forces are distributed within the fault hangingwall volume. After the onset of slip, the hangingwall preserves its inertia for a longer period since in this case external and internal (body) forces sum up downward. The aftershock sequences can be interpreted as related to the rock wedge settlement due to the closure of fractures and to the complete dissipation of gravitational energy within the dilated antithetic wedge (Doglioni et al., 2011; Doglioni et al., 2015b). On the contrary, thrust-related earthquakes are characterized by dissipation of elastic energy (Doglioni et al., 2011; Doglioni et al., 2015b; Figure 4.1b), which is stored both within the rock volume above the thrust fault (i.e., the hangingwall block) and along the thrust fault itself during the pre-seismic period (Figure 4.1b). When the elastic energy exceeds

the fault resistance, the hangingwall block generates the earthquake by moving upward along the fault (Tizzani et al., 2013). The elastic energy dissipation is buffered by the gravitational force. The downward directed gravitational force is opposite to the upward sense of motion of the fault hangingwall. As a consequence: (1) the work that the tectonic forces have to do on the block is greater and (2) after the onset of slip the hangingwall block preserves its inertia for a shorter period because most of the system energy is spent during rupture and slip along the main fault to overcome the gravitational force. For this reason (i.e., to overcome the inertial system), compressional earthquakes are of higher magnitude. Most of the energy stored during the interseismic phase is used to activate the main fault and stresses are concentrated at the interface between hangingwall and footwall blocks. Since the amount of elastic energy necessary to move downward (i.e., in favour of the gravity force) the hangingwall block during extensional earthquakes is low, we suggest that aftershocks can be easily generated until gravitational equilibrium is reached again, producing longer extensional aftershock sequences. On the contrary, since the amount of elastic energy necessary to move upward (i.e., against the gravity force) the hangingwall block during compressional earthquakes is necessarily higher, the sequence of aftershocks can be interrupted earlier. Compressional aftershock sequences are thus shorter and comprise less earthquakes than in extensional aftershock sequences (Figure 4.1). The physical model is based on both the versus and the different type of energy involved in extensional tectonic settings with respect to the compressional tectonic environments, as proposed in a previous study (Doglioni et al., 2015b).

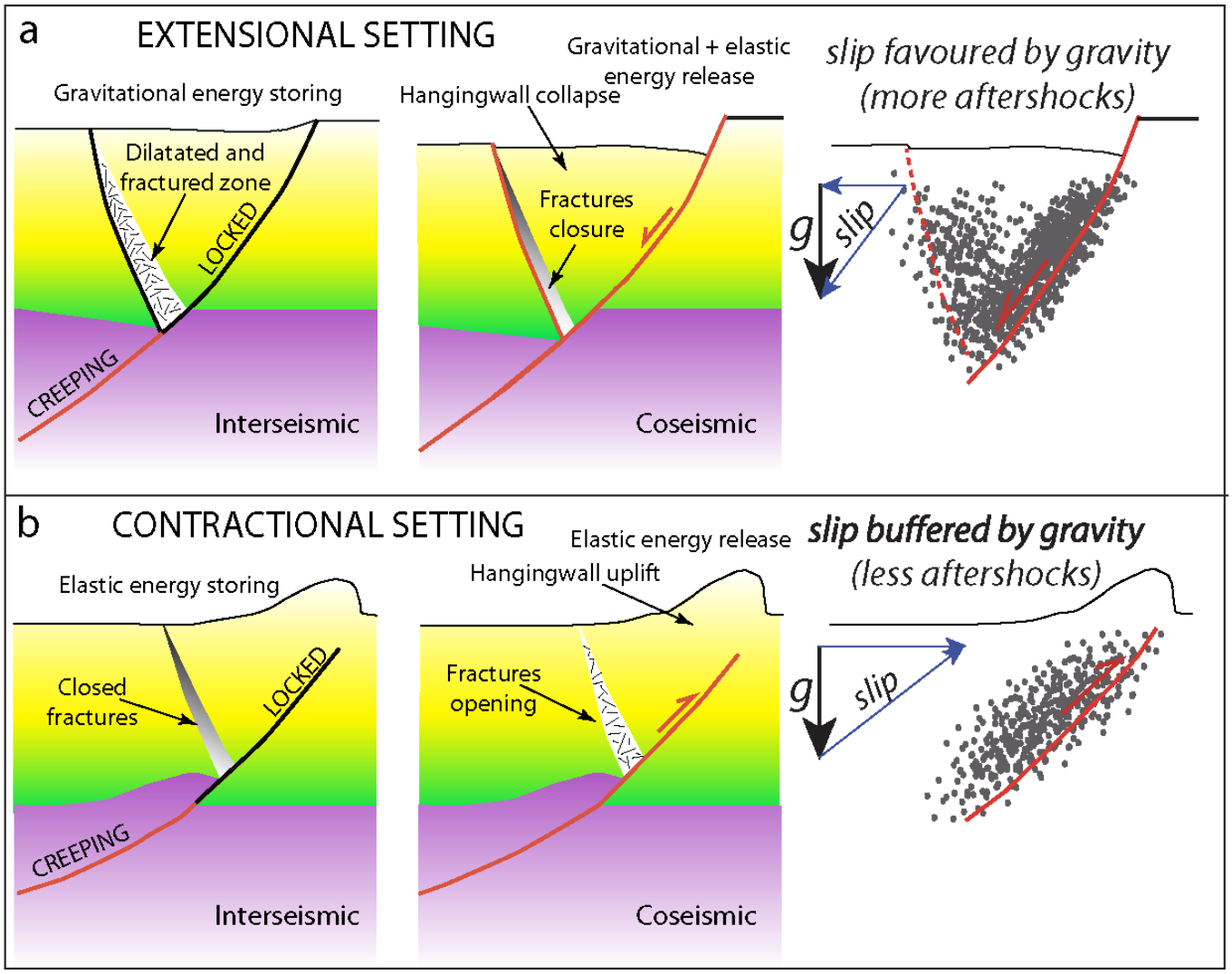

Figure 4.1. Model suggested for extensional and compressional settings. (a) Geological model of the seismic cycle (i.e., interseismic and coseismic periods) associated with a normal fault. (b) Geological model of the seismic cycle (i.e., interseismic and coseismic periods) associated with a thrust. In both models I assume a steady state strain rate in the ductile lower crust and a stick–slip motion in the brittle upper crust (modified from Doglioni et al., 2011). Extensional tectonic settings are characterized by longer aftershocks duration because the hangingwall moves in favour of gravity and the volume will collapse until a gravitational equilibrium is reached.

4.2. On the October 30th M_w 6.5 Norcia earthquake

The abovementioned dominant role played by gravity within earthquake nucleation mechanism in extensional tectonic settings has been tested in a recent case-study: the October 30th M_w 6.5 Norcia earthquake (NEQ). We have extensively exploited seismological data and multi-orbit ALOS-2 DInSAR measurements relevant to the October 30th NEQ, to investigate the earthquake main surface deformation effects and the characteristics of the seismogenic source. The starting point of our study is the analysis of a set of ALOS-2 coseismic DInSAR maps which reveals three distinct surface deformation patterns: (i) a major subsidence that reaches a maximum value of about 98 cm near the epicentral zones, nearby the town of Norcia; (ii) two smaller uplift lobes that affect both the hangingwall (reaching maximum values of about 14 cm) and the footwall blocks (reaching maximum values of about 10 cm; Figures 3.1b-e). Subsequently, we compute, by employing three different methods, the rock volumes affected by the retrieved uplift and subsidence effects during the NEQ. For all the methods, the coseismic uplift in the hangingwall block is about 1/14 of subsidence (Table 3.2), thus highlighting a significant volumetric asymmetry within the seismogenic crust. Following this analysis, we implement a numerical model of the NEQ which allows us to exploit the available geological and seismological data, and the ground deformation measurements retrieved from the multi-orbit DInSAR data. In particular, we investigate two different model scenarios obtained through the progressive integration of the a priori available information. First, we consider a more simplified scenario taking into account only the role of a single SW-dipping fault along which the M_w 6.5 NEQ nucleated. Subsequently, we implement a more realistic and complex scenario, characterized by a SW-dipping fault and an antithetic zone. We find that for the first scenario we cannot achieve a good fit with the observed ground deformations (RMS = 12,42 cm; Figure 3.9a and b); conversely, the second scenario furnishes a rather good fit with the coseismic surface deformation pattern (RMS=3,48 cm; Figure 3.11a and b). Note that our modelling approach allows us to properly reproduce the retrieved ground deformation patterns through the combination of two different effects: (i) the gravitational sliding of the hangingwall along the main fault plane and (ii) the frictional force acting in the opposite direction, consistently with the double couple fault plane mechanism. These two effects are considered in both

scenarios and, as already said, the second one, which consist of a SW-dipping fault and an antithetic zone, presents a rather good fit with the coseismic surface deformation pattern (Figure 3.11a and b). Therefore, we suggest that this second scenario represents a reliable one. In this case, two further elements are discussed in the following, which are relevant to the available seismological information and the retrieved rock volumes unbalance. For what concerns the signature of the antithetic zone, we remark that it is clearly visible through the hypocentral distribution of the earthquakes occurred between August 24th and October 29th, 2016, showing an evident antithetic alignment; the seismicity data analysis suggests that the formation of this antithetic zone has already occurred before the NEQ nucleation (Figures 3.1c-f). Moreover, Porreca et al. (2018) provided a novel reconstruction of the subsurface geology of the considered seismogenic area by using seismic reflection profiles. In particular, we take into account one of the interpreted sections in which the presence of an antithetic zone is clearly visible. Consequently, we analyse the temporal evolution of the occurred seismic events by combining and comparing their hypocentral locations with the abovementioned seismic profile, obtaining a good fitting. Finally, the distribution of the overall events of the seismic crisis and of those recorded since January 2015 also highlight the spatial position of the decollement layer.

As regards the GPS measurements and the related geodetic modelling, the achieved results indicate that, during the M_w 6.5 NEQ, an additional dislocation occurred along a secondary fault and the presence of an antithetic structure can be considered a valid hypothesis to explain the retrieved geodetic deformation values (Figure 3.6).

As regards the retrieved volume unbalance, we underline that the processes that could promote such permanent deformation within a rock mass are the diffusion mass transfer (i.e., pressure solution) and/or the plastic deformation (i.e., mineral recrystallization, grain boundary sliding). These processes are related to low strain rates phenomena occurring during interseismic phases, as also shown by field evidences (Gratier et al., 2013) and laboratory simulations (Tesei et al., 2014). However, during the NEQ nucleation, we have calculated a volume deficit in response to a high strain rate event. A possible explanation of this finding is based on the presence, at depth, of an interseismically dilated volume able to accommodate the

collapse of a wedge bounded by the main fault, the antithetic one and a decollement layer. As proposed in Doglioni et al. (2015a), the hangingwall collapse can be allowed by the presence of a dilated zone, located antithetically to the main fault, generated from the decollement upward and that can absorb the volume settlement. When the strength of the fractured antithetic fault is not anymore able to sustain the weight of the rock wedge, the collapse of the hangingwall occurs in favor of gravity and the slip along the antithetic fault allows the closure of the fractures generating the expulsion of the fluids (Doglioni et al., 2015a). In fact, we can interpret this volume as provided by microfractures filled by fluids circulating within the seismogenic crust; furthermore, their expulsion has been observed during the late pre-seismic and coseismic stage of the NEQ and could be related to the closure of this multitude of microfractures and by the consequent decrease during the earthquake of diffuse permeability (Barberio et al., 2017). We further remark that fluids expulsion phenomena are typical of extensional earthquakes such as the 1997 M_w 6.0 Colfiorito (Quattrocchi et al., 2000; Carro et al., 2005) and the 2009 M_w 6.3 L'Aquila earthquakes (Di Luccio et al., 2010; Terakawa et al., 2010; Doglioni et al., 2014; Sugan et al., 2014).

The retrieved results have been very useful to clarify the kinematics of the M_w 6.5 NEQ and to propose a new interpretation about this seismic event. According to Cheloni et al. (2017), both an antithetic normal fault and a pre-existing compressional low-angle structure (likely related to a segment of the Sibillini Thrust; Lavecchia et al., 2016) associated with a main SW-dipping normal fault can explain the retrieved geodetic measurements and modelling. In fact, both the structural sections across the seismogenic area, the elongated seismicity pattern and the inversion of geodetic data do not allow to discern between the two possible scenarios. In the wake of this work and analysing thoroughly both seismological and DInSAR evidence, I have decided to focus my work on the role of antithetic NE-dipping structure. The built model, that in detail takes into the antithetic zone in addition to the main fault and the role of gravity, can be considered convincing to explain the retrieved deformation values and is also in agreement with the general tectonic setting of the Central Apennines. The development of the abovementioned 2D modelling, the employed multidisciplinary approach and the very good fit obtained between the model and the retrieved

DInSAR-based ground deformation measurements allow to introduce an alternative interpretation with respect to the other models proposed until now (e.g., Scognamiglio et al., 2018).

4.3 General discussion

The analyses performed during this Ph.D. and well described in the previous chapters permit to make some observations to contextualise all the retrieved results into a more general model.

The results obtained by both aftershocks duration analysis and numerical modelling approach allow us to take into consideration the importance of the different kinds of energies involved in earthquakes nucleation and, in particular, the role played by gravitational energy. It is well known that the potential energy (mainly elastic and gravitational energies), accumulated for tens or thousands of years during the inter-seismic phase, is released instantaneously through an earthquake during the co-seismic phase in the form of radiated energy, fracture energy, and thermal energy (Kanamori and Rivera, 2006). In the specific case of extensional earthquakes, the dominant effect of the gravitational force, which acts on rock bodies, and the double-couple mechanism on the main faults favourite the downward motion of the involved seismogenic rock blocks. The involvement of the rock blocks during earthquake nucleation process is also testify by the fractal dimension (D) values; in fact, as computed by using the Mandelbrot method, D varies between ca. 2–3 and ca. 1–2 for extensional and compressional earthquakes, respectively, highlighting a substantial difference between extensional and compressional sequences. As the fractal dimension is indicative of the geometrical fragmentation process, with time extensional seismic sequences are thus spatially distributed within a volume, while compressional seismic sequences closer to a fault along a surface. For example, in the case of the NEQ, the spatial distribution of aftershocks and their temporal evolution represent an evidence of the validity of the fractal dimension values; in fact, the analysed aftershocks tend to occupy the seismogenic hangingwall block confined by the main normal fault and an antithetic fractured dilated zone (Figure 3.1c-f). According to Doglioni et al. (2015a), single extensional seismic sequences dissipate gravitational energy (Figure 4.1a) stored during the interseismic phase, within the hangingwall volume. When the stresses related to this gravitational energy exceed the strength of the dilated zone and of the main normal fault, the rock volume collapses slipping along the main fault, generating the earthquake (Figure 4.1a). The downward hangingwall block movement is favoured by gravity itself. The fall of the

hangingwall of the normal fault is allowed by the presence of a dilated inclined wedge generated from the BDT upward that can absorb the volume decrement during the collapse; this rock wedge is kinematically and mechanically required by the strain partitioning between the brittle upper crust and the ductile lower crust (Petricca et al., 2015). Due to the prevailing action of gravity in earthquake nucleation processes, in literature extensional events are also defined as "graviquakes" (Doglioni et al., 2011; Doglioni et al., 2015a). On the other hand, within compressional and strike-slip tectonic settings, the dissipation of elastic energy is preponderant with respect to gravitational one and, for this reason, this events are also called "elastoquakes". Since the hangingwall block moves upward along the fault generating the mainshock, the elastic energy dissipation is buffered by the gravitational force (Doglioni et al., 2011; Doglioni et al., 2015b; Figure 4.1b); indeed, the downward directed gravitational force is opposite to the upward sense of motion of the fault hangingwall.

The substantial differences that exist between extensional and compressional seismic events (i.e., in terms of aftershocks duration, of fractal dimension values, of involved energies) can also affect the preseismic phase. The associated phenomenology may be summarized into some possible precursors such as foreshocks nucleation, subsidence onset of the hangingwall that could be detected by DInSAR measurements, variations of fluids circulation and, consequently, of the V_p/V_s ratio.

The analysis of the mid-term behaviour of an ongoing seismic sequence, the application of an integrating multidisciplinary approach and the monitoring of some parameters that could occur before the mainshock event in areas of low strain rate along active faults may eventually provide potential tools for a better understanding of earthquakes kinematics within different tectonic settings (i.e., extensional, compressional and strike-slip environments). Therefore, one of the most important goals of this kind of multidisciplinary approach regards the definition, the assessment and the enhancement of seismic hazard within active seismogenic regions.

Chapter 5

Conclusions and future perspectives

In this Ph.D. thesis we have performed a detailed analysis of seismic sequences by employing different techniques and by integrating seismological data, geodetic measurements and numerical modelling.

In the first part (Chapter 2) of the thesis, we have carried out a comparative analysis of ten aftershock sequences occurred in extensional and compressional tectonic settings using two different methods (i.e., the Tangents method and the Mandelbrot method); the retrieved results have allowed us to argue that, irrespective of the mainshock magnitude, aftershock sequences in extensional tectonic settings are longer and comprise more seismic events than those in compressional settings. We have proposed that these differences can be due to the different type of energy stored within extensional and compressional tectonic settings during the interseismic stage and dissipated during the earthquake sequences: (i) gravitational energy with a minor elastic component dominates in extensional sequences whereas (ii) pure elastic energy is dissipated in compressional sequences. Therefore, for mainshocks of comparable magnitudes, extensional aftershock sequences last longer because the downward hangingwall movement is favoured by gravity and will continue until the gravitational equilibrium is reached. During compressional earthquakes, the upward hangingwall motion occurs instead against gravity and thrust-related aftershocks end earlier because the elastic energy dissipation is hindered by the gravitational force.

In the second part (Chapter 3) of this work, we have applied a multidisciplinary approach to study the October 30th, 2016 M_w 6.5 Norcia (Central Italy) earthquake by exploiting the information derived from the hypocentral distribution of the occurred seismic events, the DInSAR measurements obtained from the ALOS-2 sensor and a numerical modelling. The analysis of the relocated hypocentres has allowed to highlight three main structures: (i) a SW-dipping alignment parallel to the main fault system; (ii) an E-dipping low-angle normal fault cutting through the upper crust; (iii) ENE-dipping structures that are antithetic to the main fault. The DInSAR measurements showed that the considered seismogenic area was

interested by significant coseismic ground deformations. In particular, the vertical displacement map showed three main deformation patterns: (i) a major subsidence that reaches a maximum value of about 98 cm near the epicentral zones nearby the town of Norcia; (ii) two smaller uplift lobes that affect both the hangingwall (reaching maximum values of about 14 cm) and the footwall blocks (reaching maximum values of about 10 cm); the coseismic uplift in the hangingwall block is about 1/14 of subsidence, suggesting an unbalance between the subsided and the uplifted volumes within the seismogenic crust. The results of our 2D modelling have highlighted that the presence of an antithetic zone is necessary to reach the best fit between measured and simulated coseismic surface deformations (RMS=3,48 cm). This scenario has allowed to justify the occurrence of subsidence and uplift phenomena caused by the M_w 6.5 Norcia earthquake as the result of the gravitational sliding of the hangingwall along the main fault plane and the frictional force acting in the opposite direction, consistently with the double couple fault plane mechanism.

The analysis performed for this Ph.D. thesis allow to sketch some future perspectives. Future work should be focused on the analysis of aftershock sequences within other tectonic settings, such as subduction zones and/or strike-slip environments. Moreover, it could be useful to apply the same analysis to other cases, in order to extend the statistics of the studied earthquake at a major scale, and to consider also foreshock events. The hypothesized influence of the different energies involved during earthquakes nucleation process within different tectonic settings can have also repercussions on earthquakes kinematics; therefore, the available multidisciplinary data (geodetic measurements, seismological data, seismic profiles, geological and petrophysical information) and their integration within a numerical model could represent a turning point in a better and more complete understanding of seismic events occurrence. Furthermore, the continuous monitoring (made possible by the short-time acquisitions of satellites and by the real-time recording of seismometers and GPS) of active areas and the integration of the collected data could help in the characterization of the preseismic phase. To conclude, on one hand, the comparative analysis of aftershock seismic sequences is useful in understanding the mid-term behaviour of an ongoing seismic sequence within different tectonic settings; on the other hand, the abovementioned

multidisciplinary approach can improve the knowledge about earthquakes kinematics. Both analyses can be considered valid to provide useful inputs to improve seismic hazard assessment in active seismogenic areas.

Appendix A

A.1 Aftershock sequences evolution according to the Omori law

We used ZMAP (Wiemer, 2001), an algorithm developed in MatLab environment, to describe the aftershocks decay of a seismic sequence according to the Omori-Utsu Law (Omori, 1894; Utsu, 1961):

$$n(t) = \frac{k}{(c+t)^p} \quad \text{(A.1)}$$

where *k* and *c* are constant, *t* is the time and *p* indicates the rate decay. In particular, the *p* value is a key parameter representative of each earthquake and varies between 0.7 and 1.5. The variability in p- value may be related to the structural heterogeneity, stress and temperature in the crust (Utsu and Ogata, 1995). However, it is not clear yet which of these factors is most significant in controlling the p-value. The K-value is dependent on the total number of events in the sequence and *c* on the rate of activity in the earliest part of the sequence. The constant *c* is a controversial quantity (Utsu and Ogata, 1995); in fact, it is strongly influenced by the incompleteness of the catalogue in the early part of a sequence.

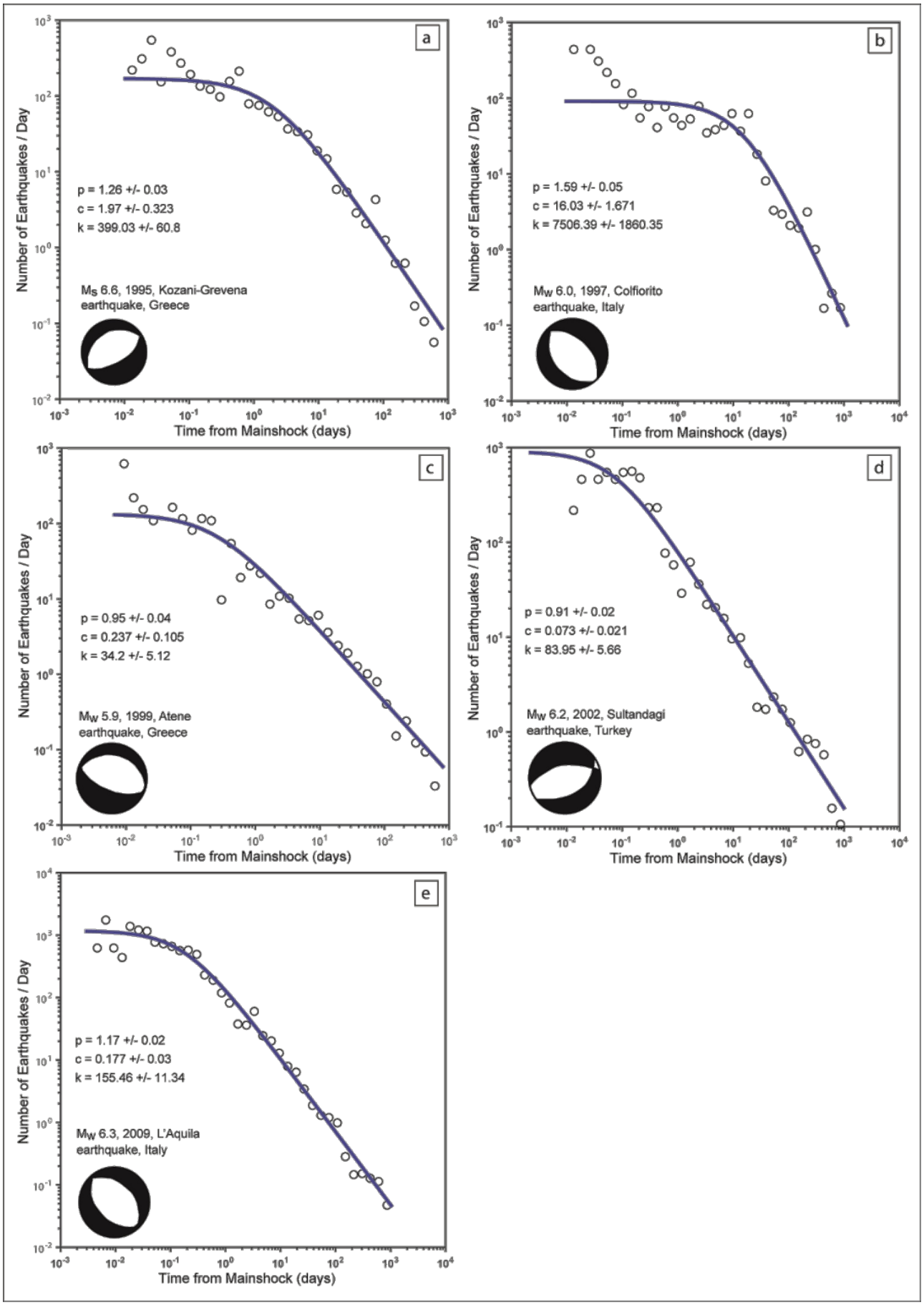
a
p = 1.26 +/- 0.03
c = 1.97 +/- 0.323
k = 399.03 +/- 60.8
Ms 6.6, 1995, Kozani-Grevena earthquake, Greece
b
p = 1.59 +/- 0.05
c = 16.03 +/- 1.671
k = 7506.39 +/- 1860.35
Mw 6.0, 1997, Colfiorito earthquake, Italy
c
p = 0.95 +/- 0.04
c = 0.237 +/- 0.105
k = 34.2 +/- 5.12
Mw 5.9, 1999, Atene earthquake, Greece
d
p = 0.91 +/- 0.02
c = 0.073 +/- 0.021
k = 83.95 +/- 5.66
Mw 6.2, 2002, Sultandagi earthquake, Turkey
e
p = 1.17 +/- 0.02
c = 0.177 +/- 0.03
k = 155.46 +/- 11.34
Mw 6.3, 2009, L'Aquila earthquake, Italy
Number of Earthquakes / Day
Time from Mainshock (days)

Figure A1. Aftershock sequences temporal evolution analysed by using the Omori method in case of five extensional earthquakes case studies: a) the M_s 6.6 Kozani-Grevena earthquake (1995, Greece), b) the M_w 6.0 Colfiorito earthquake (1997, Central Italy), c) the M_w 5.9 Athens earthquake (1999, Greece), d) the M_w 6.2 Sultandagi earthquake (2002, Turkey), and e) the M_w 6.3 L'Aquila earthquake (2009, Central Italy). The fundamental parameter (p, c and k) values are also reported in the graphs. The days of the mainshock and after the mainshock are reported on the x-axis and the number of earthquakes per day is shown on the *y*-axis. The data are represented by circles and are fitted by a curve.

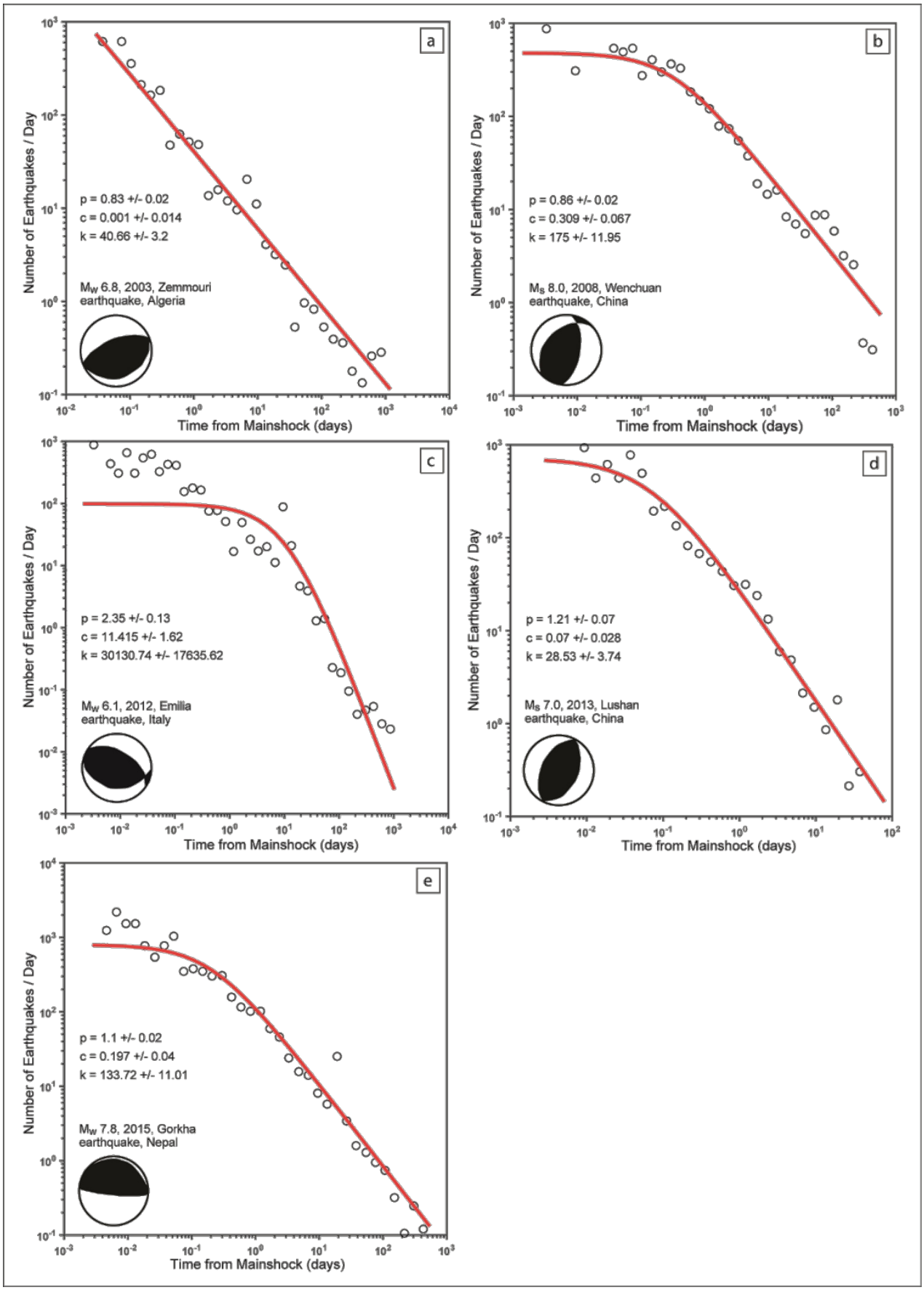
a
Number of Earthquakes / Day
Time from Mainshock (days)
p = 0.83 +/- 0.02
c = 0.001 +/- 0.014
k = 40.66 +/- 3.2
Mw 6.8, 2003, Zemmouri earthquake, Algeria
b
Number of Earthquakes / Day
Time from Mainshock (days)
p = 0.86 +/- 0.02
c = 0.309 +/- 0.067
k = 175 +/- 11.95
Ms 8.0, 2008, Wenchuan earthquake, China
c
Number of Earthquakes / Day
Time from Mainshock (days)
p = 2.35 +/- 0.13
c = 11.415 +/- 1.62
k = 30130.74 +/- 17635.62
Mw 6.1, 2012, Emilia earthquake, Italy
d
Number of Earthquakes / Day
Time from Mainshock (days)
p = 1.21 +/- 0.07
c = 0.07 +/- 0.028
k = 28.53 +/- 3.74
Ms 7.0, 2013, Lushan earthquake, China
e
Number of Earthquakes / Day
Time from Mainshock (days)
p = 1.1 +/- 0.02
c = 0.197 +/- 0.04
k = 133.72 +/- 11.01
Mw 7.8, 2015, Gorkha earthquake, Nepal

Figure A2. Aftershock sequences temporal evolution analysed by using the Omori method in case of five compressional earthquakes case studies: a) the M_w 6.8 Zemmouri earthquake (2003, Algeria), b) the M_s 8.0 Wenchuan earthquake (2008, China), c) the M_w 6.1 Emilia earthquake (2012, Northern Italy), d) the M_s 7.0 Lushan earthquake (2013, China), and e) the M_w 7.8 Gorkha earthquake (2015, Nepal). The fundamental parameter (p, c and k) values are also reported in the graphs. The days of the mainshock and after the mainshock are reported on the x-axis and the number of earthquakes per day is shown on the *y*-axis. The data are represented by circles and are fitted by a curve.

Extensional earthquakes			
	p	***c***	***k***
Kozani-Grevena earthquake	*1.26 ± 0.03*	*1.97±0.323*	*399.03±60.8*
Colfiorito earthquake	*1.59 ± 0.05*	*16.03 ± 1.671*	*7506.39 ± 1860.35*
Athens earthquake	*0.95 ± 0.04*	*0.237 ± 0.105*	*34.2 ± 5.12*
Sultandagi earthquake	*0.91 ± 0.02*	*0.073 ± 0.021*	*83.95 ± 5.66*
L'Aquila earthquake	*1.17 ± 0.02*	*0.177 ± 0.03*	*155.46 ± 11.34*
Compressional earthquakes			
	p	***c***	***k***
Zemmouri earthquake	*0.83 ± 0.02*	*0.001 ± 0.014*	*40.66 ± 3.2*
Wenchuan earthquake	*0.86 ± 0.02*	*0.309 ± 0.067*	*175 ± 11.95*
Emilia earthquake	*2.35 ± 0.13*	*11.415 ± 1.62*	*30130.74 ± 17635.62*
Lushan earthquake	*1.21 ± 0.07*	*0.07 ± 0.028*	*28.53 ± 3.74*
Gorkha earthquake	*1.1 ± 0.02*	*0.197 ± 0.04*	*133.72 ± 11.01*

Table A1. List of the parameters of the Omori Law (p, c and k) calculated for each seismic sequence.

A.2 Strain release variations vs. time

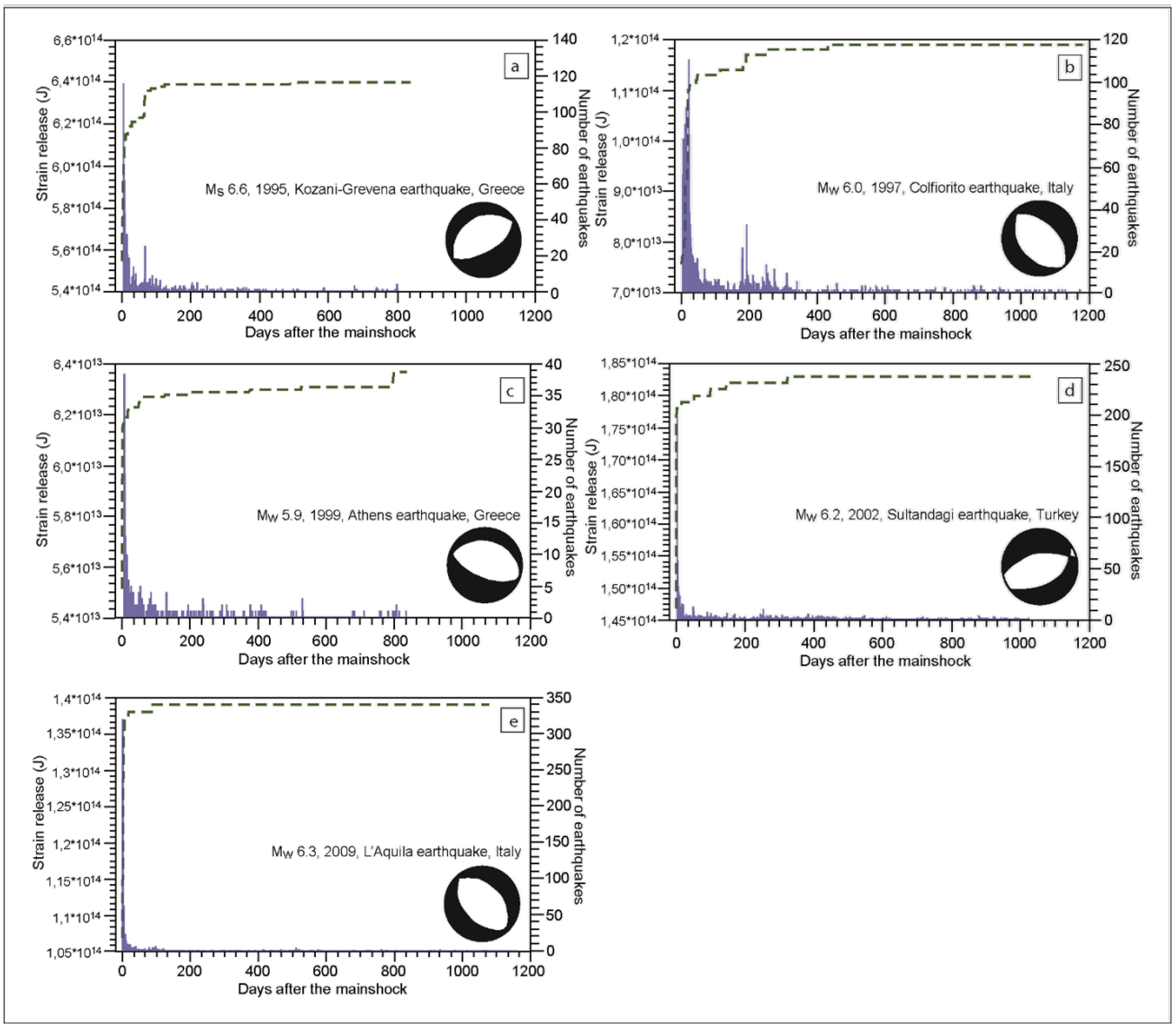

Figure A3. The green dashed lines represent the strain release versus time and the number of occurred earthquakes in case of five extensional earthquakes: a) the M_s 6.6 Kozani- Grevena earthquake (1995, Greece), b) the M_w 6.0 Colfiorito earthquake (1997, Central Italy), c) the M_w 5.9 Athens earthquake (1999, Greece), d) the M_w 6.2 Sultandagi earthquake (2002, Turkey), and e) the M_w 6.3 L'Aquila earthquake (2009, Central Italy).

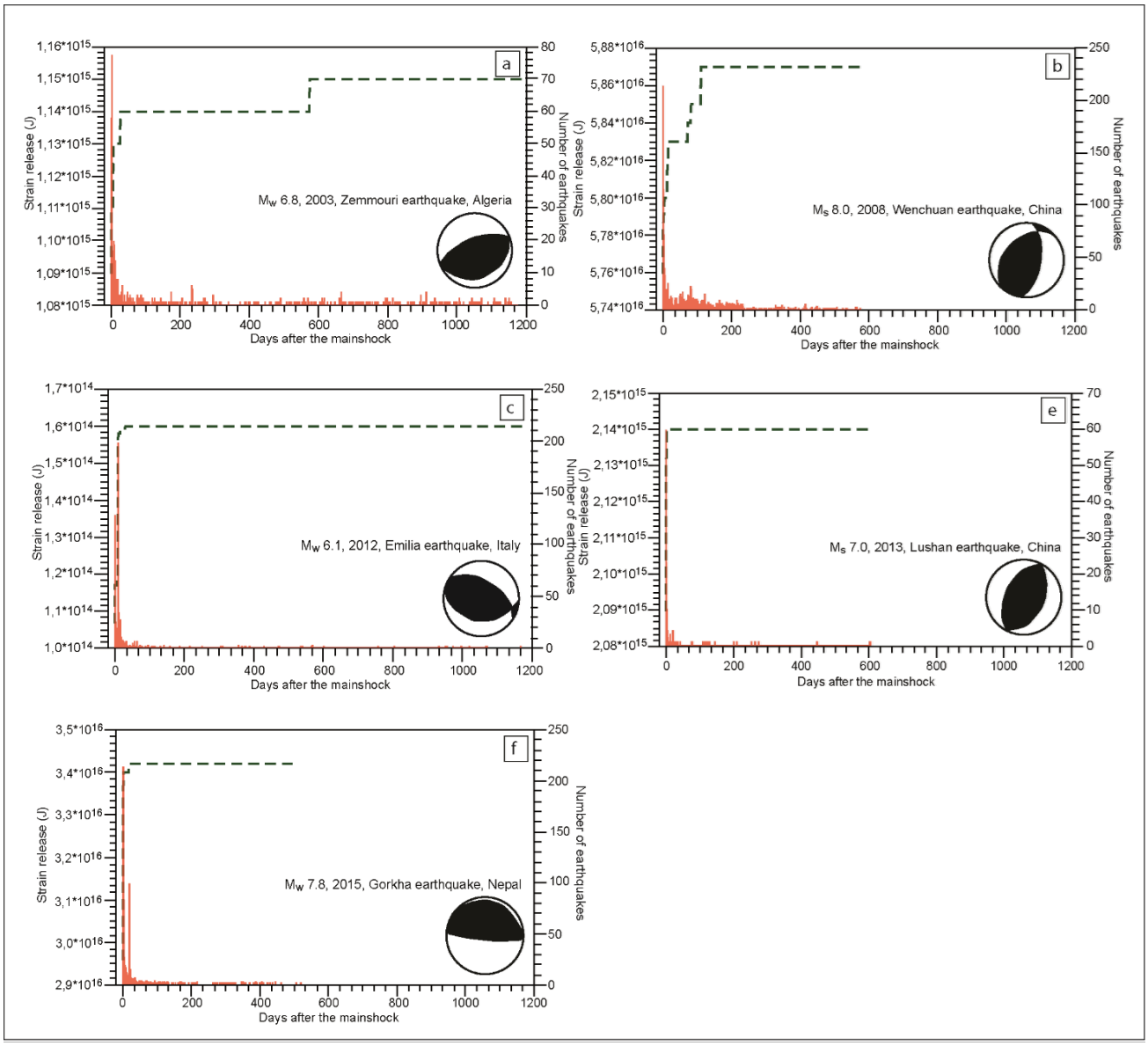

Figure A4. The green dashed lines represent the strain release versus time and the number of occurred earthquakes in case of five compressional earthquakes: a) the M_w 6.8 Zemmouri earthquake (2003, Algeria), b) the M_s 8.0 Wenchuan earthquake (2008, China), c) the M_w 6.1 Emilia earthquake (2012, Northern Italy), d) the M_s 7.0 Lushan earthquake (2013, China), and e) the M_w 7.8 Gorkha earthquake (2015, Nepal).

A.3 R squared values

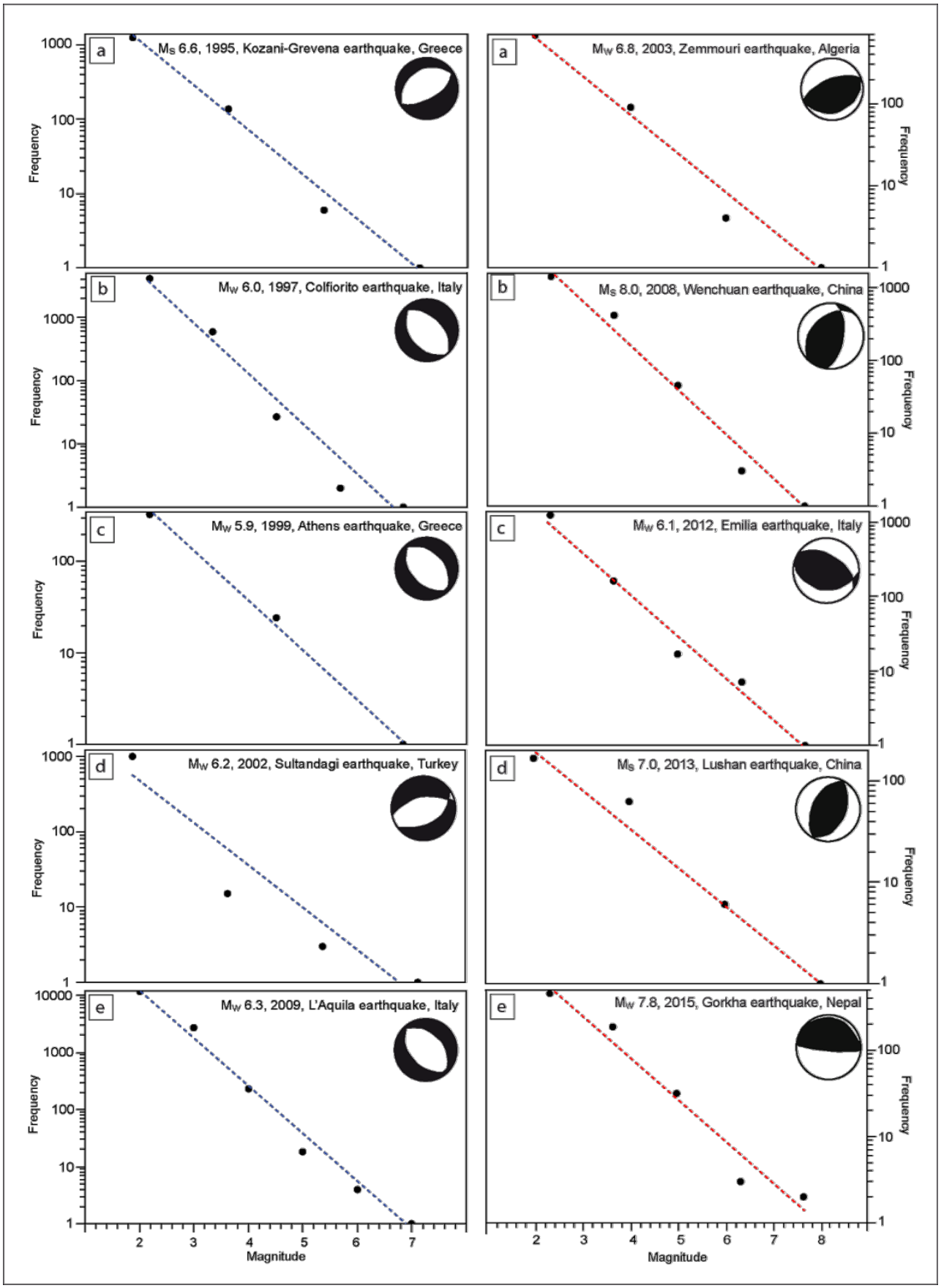

Figure A5. Number of earthquakes versus magnitude calculated for each seismic sequence in correspondence of the maximum R squared value. Extensional earthquakes are reported on the left part of the graph and compressional earthquakes on the right part. In both cases the dashed lines follow the equation that define a fractal set and represent the linear regression.

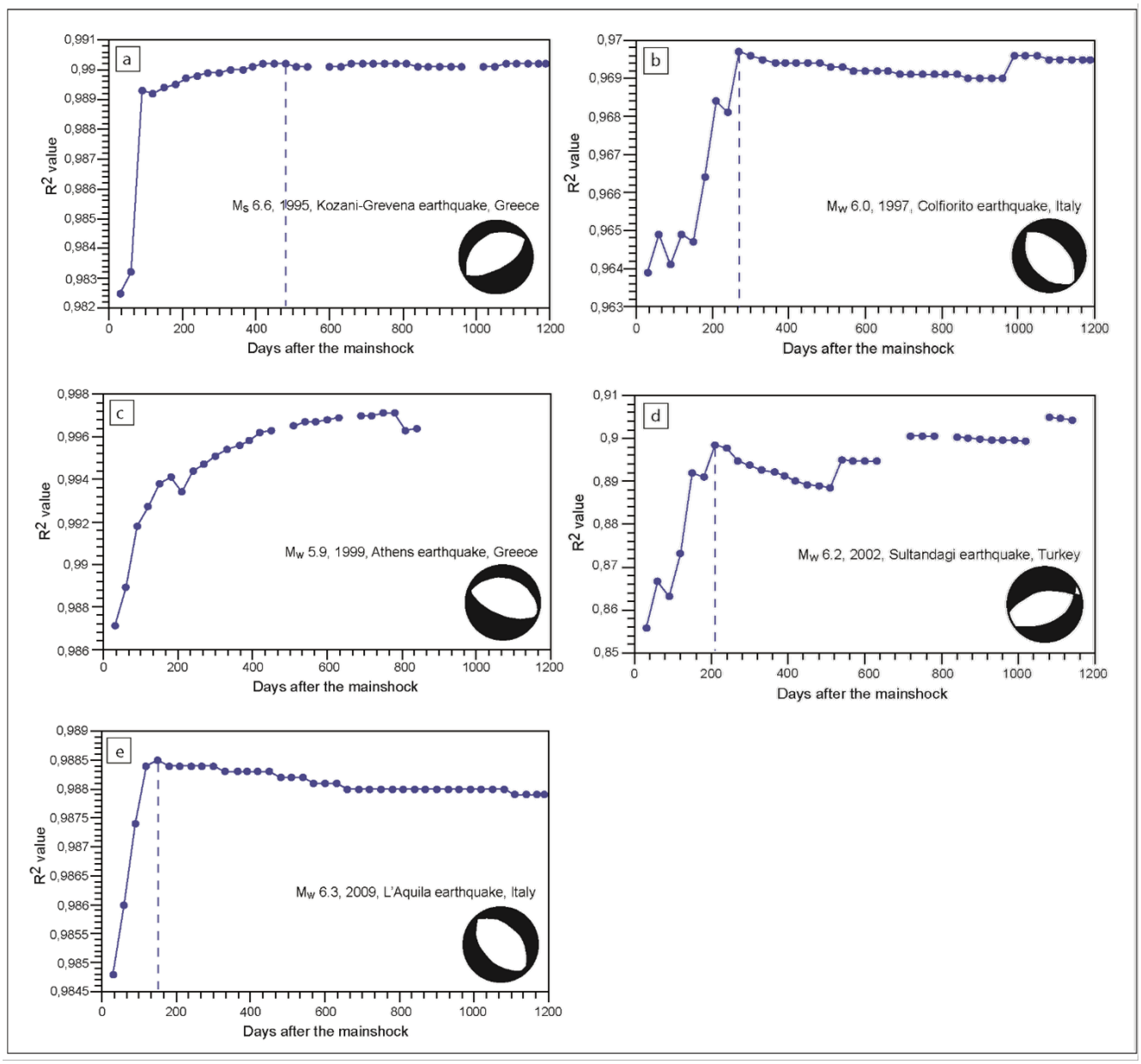

Figure A6. R squared value temporal evolution in case of five extensional earthquakes: a) the M_s 6.6 Kozani-Grevena earthquake (1995, Greece), b) the M_w 6.0 Colfiorito earthquake (1997, Central Italy), c) the M_w 5.9 Athens earthquake (1999, Greece), d) the M_w 6.2 Sultandagi earthquake (2002, Turkey), and e) the M_w 6.3 L'Aquila earthquake (2009, Central Italy). The days of the mainshock and after the mainshock are reported on the x-axis and R squared (R^2) values are shown on the *y*-axis.

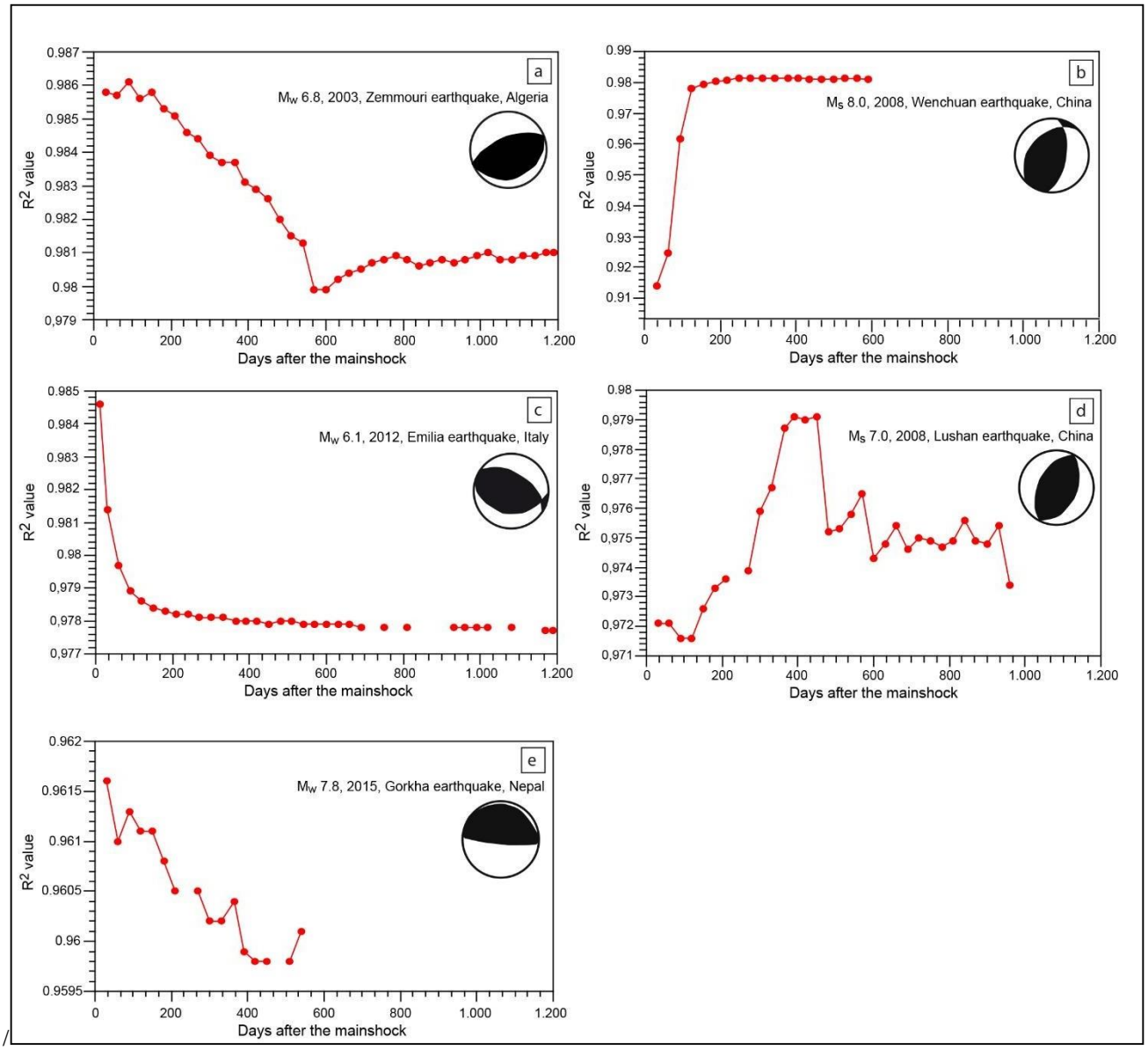

Figure A7. R squared value temporal evolution in case of five compressional earthquakes: a) the M_w 6.8 Zemmouri earthquake (2003, Algeria), b) the M_s 8.0 Wenchuan earthquake (2008, China), c) the M_w 6.1 Emilia earthquake (2012, Northern Italy), d) the M_s 7.0 Lushan earthquake (2013, China), and e) the M_w 7.8 Gorkha earthquake (2015, Nepal). The days from the mainshock on are shown on the x-axis and the R squared (R^2) values are shown on the *y*- axis.

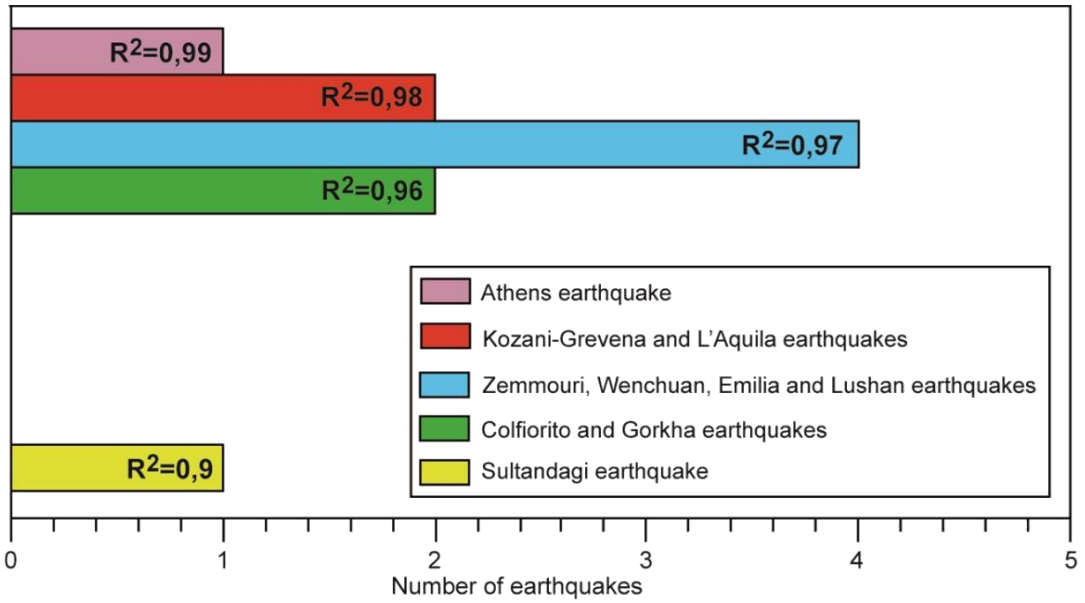

Figure A8. Histogram of the R squared values calculated for each seismic sequence. The number of events is shown on the *x*-axis versus the R squared values reported on the *y*-axis. All the seismic sequences are characterized by $R^2 \geq 0.90$.

A.4 Magnitude distribution vs. time

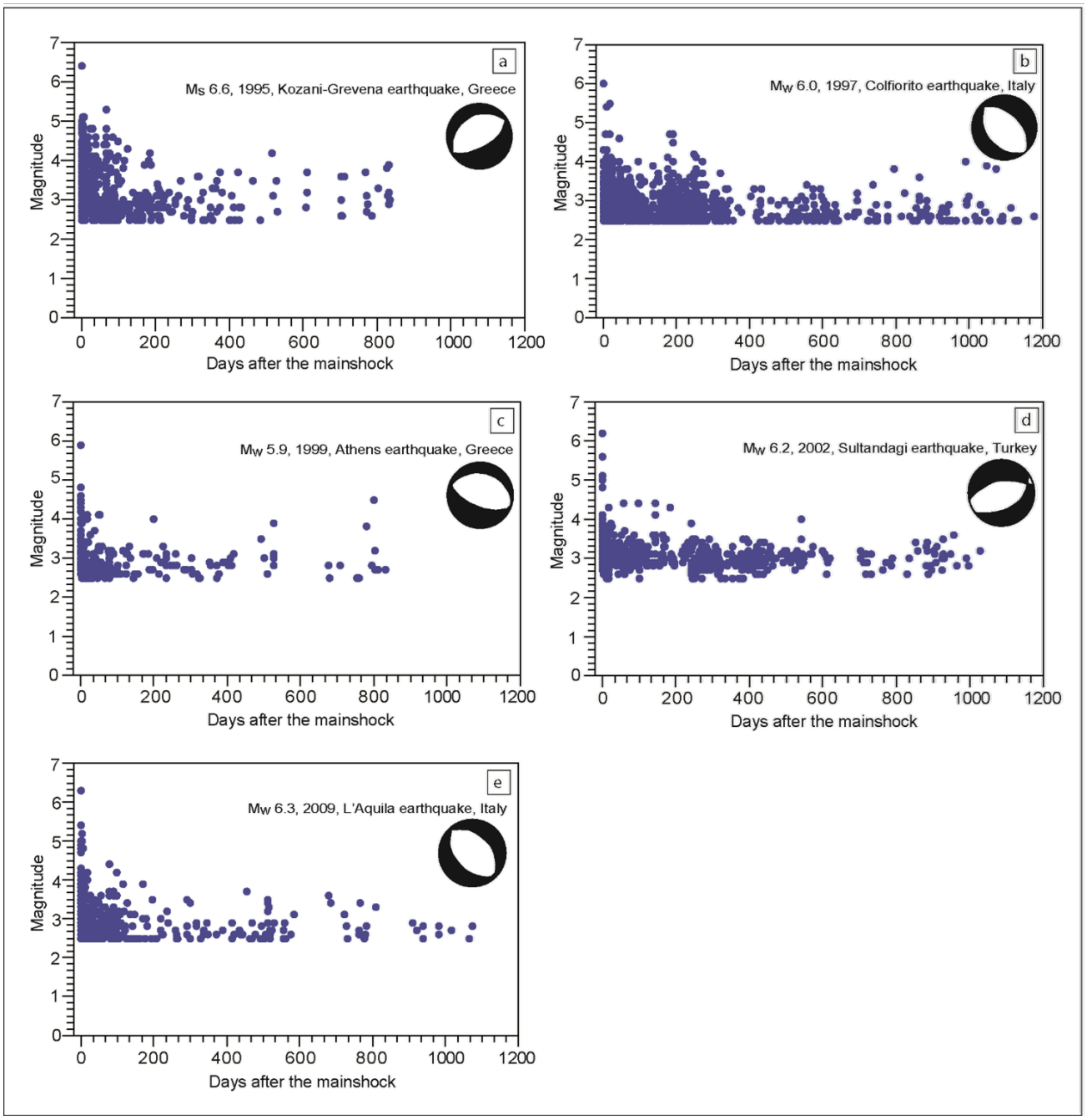

Figure A9. Magnitude distribution versus time in case of five extensional earthquakes: a) the M_s 6.6 Kozani-Grevena earthquake (1995, Greece), b) the M_w 6.0 Colfiorito earthquake (1997, Italy), c) the M_w 5.9 Athens earthquake (1999, Greece), d) the M_w 6.2 Sultandagi earthquake (2002, Turkey), and e) the M_w 6.3 L'Aquila earthquake (2009, Italy). The days from the mainshock on are shown on the *x*-axis and magnitude values are shown on the *y*-axis.

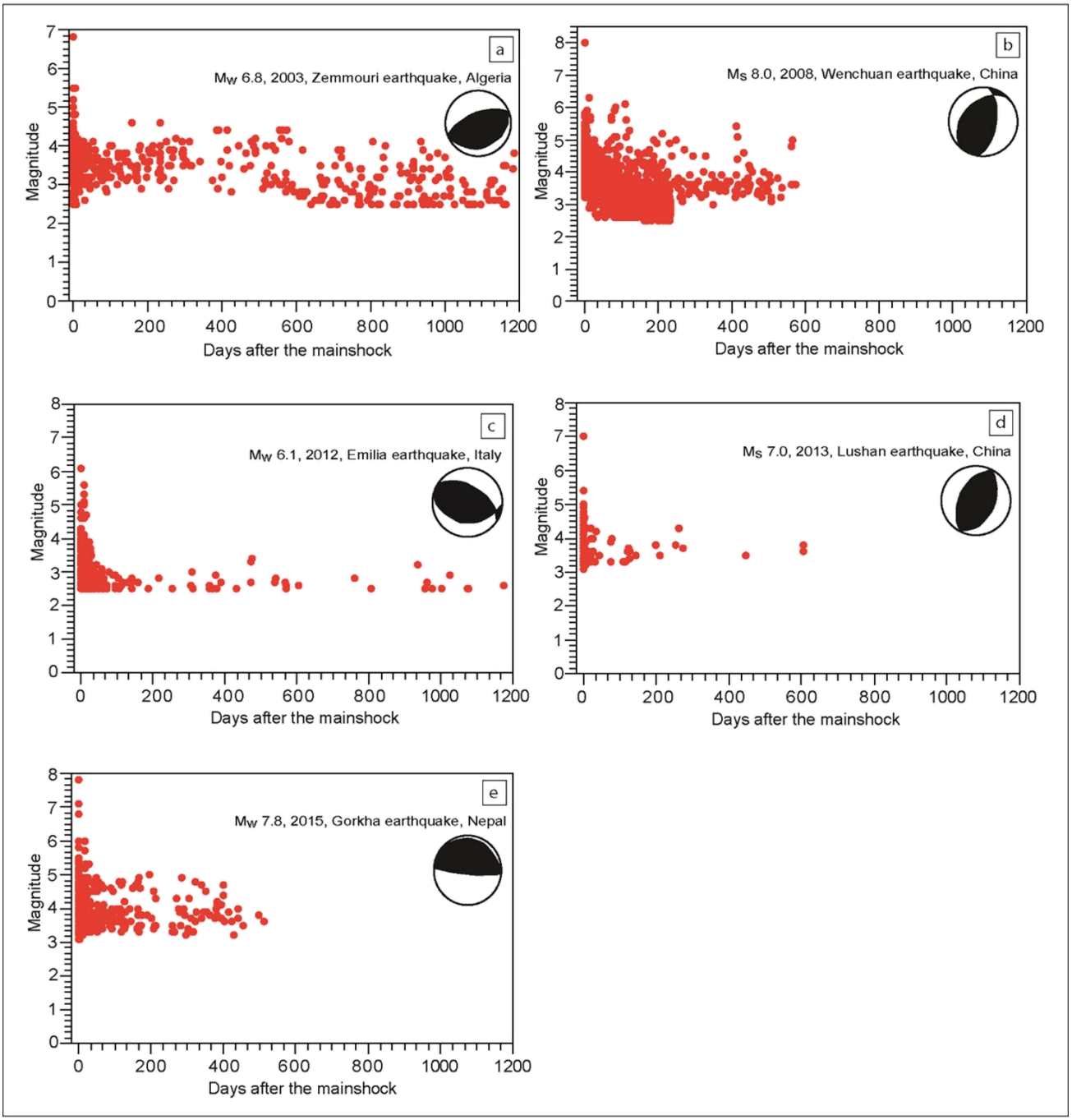

Figure A10. Magnitude distribution versus time in case of five compressional earthquakes: a) the M_w 6.8 Zemmouri earthquake (2003, Algeria), b) the M_s 8.0 Wenchuan earthquake (2008, China), c) the M_w 6.1 Emilia earthquake (2012, Italy), d) the M_s 7.0 Lushan earthquake (2013, China), and e) the M_w 7.8 Gorkha earthquake (2015, Nepal). The days from the mainshock on are shown on the *x*-axis and magnitude values are shown on the *y*-axis.

A.5 Areas evaluation: the Amatrice-Norcia extensional sequence vs. the Emilia compressional sequence

We considered two case-studies: the Amatrice-Norcia extensional seismic sequence and the Emilia compressional seismic sequence. Both seismic sequences are characterized by the nucleation of two strong earthquakes. In the first case, the M_w 6.0 Amatrice earthquake occurred on August 24th, 2016 and was followed by the M_w 6.5 Norcia event nucleated on October 30th. In the second case, the M_w 6.1 Emilia mainshock occurred on May 20th, 2012 and, after nine days (on May 29th, 2012), a M_w 6.0 earthquake nucleated along the consecutive thrust.

We calculated the areas involved in the earthquake nucleation processes and suggest that the detected ground deformation pattern represents the surficial signature of deformation that affects a broad rock volume during extensional earthquakes and mostly along a surface during the evolution of compressional earthquakes, as also indicated by the fractal dimension analysis (Figures 2.5 and 2.6). For this reason, we considered two images: the first one is the unwrapped interferogram of the Amatrice and Norcia extensional earthquake (Figure A11a; 2016-2017, Central Italy, M_w 6.0 and M_w 6.5) and the second one is the unwrapped interferogram of the Emilia compressional earthquake (Figure A11b; 2012, Northern Italy, M_w 6.1). We estimated the area included in the isolines -2 and +2 in case of the Amatrice-Norcia extensional sequence and of the Emilia compressional sequence, respectively. We obtained an area equal to ca. 350 km^2 for the Amatrice-Norcia case and equal to ca. 290 km^2 for the Emilia sequence.

The lateral extensions of the ground deformation pattern along the direction normal to the detected fault system show values included between 8-12 km and 5-7 km for the Amatrice-Norcia and the Emilia seismic sequences, respectively. Therefore, we argue that the subsidence volume involved in extensional earthquake nucleation processes is greater than the uplift volume involved in compressional nucleation processes.

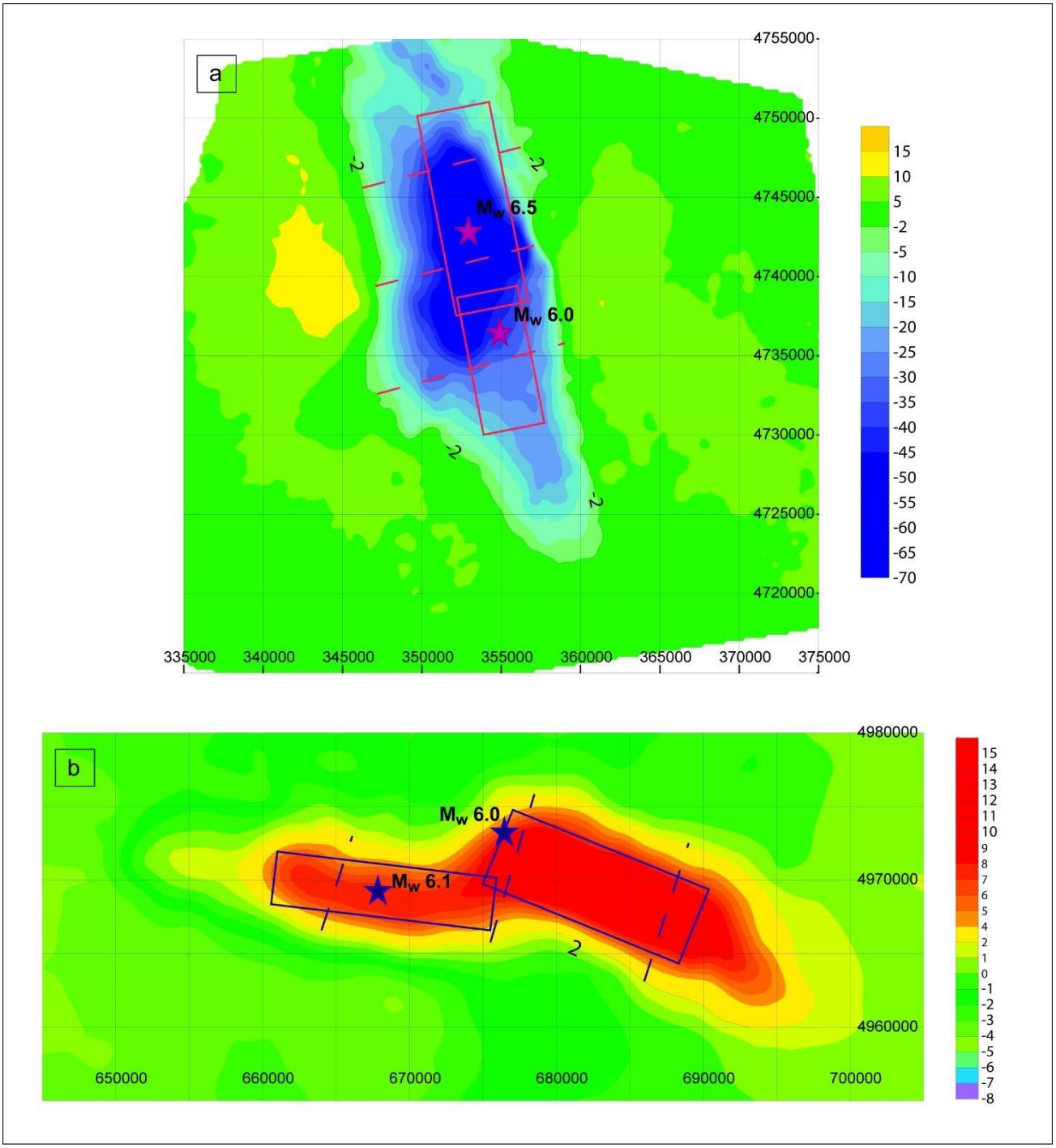

Figure A11. a) Unwrapped interferogram of the Amatrice and Norcia mainshocks (2016, Central Italy, M_w 6.0 and 6.5, respectively). The magenta rectangles represent the fault structures along which the mainshocks (magenta stars) nucleate (e.g., Cheloni et al., 2017); b) Unwrapped interferogram of the Emilia compressional mainshocks (2012, Northern Italy, M_w 6.1 and 6.0, respectively). The blue rectangles represent the fault structures along which the mainshocks (blue stars) nucleate (e.g. Tizzani et al., 2013).

References

Alavi, M. Structures of the Zagros fold-thrust belt in Iran. *Am. J. Sci.* **2007**, 307, 1064-1095, doi: 10.2475/09.2007.02.

Amato, A.; Azzara, R. ; Chiarabba, C. ; Cimini, G.B.; Cocco, M. ; Di Bona, M.; Margheriti, L.; Mazza, S.; Mele, F.; Selvaggi, G.; Basili, A.; Boschi, E.; Courboulex, F.; Deschamps, A.; Gaffet, S.; Bittarelli, G.; Chiaraluce, L.; Piccinini, D.; Ripepe, M. The 1997 Umbria-Marche, Italy, earthquake sequence: A first look at the main shocks and aftershocks. *Geophys. Res. Lett.* **1998**, 25, 2861–2864, doi: 10.1029/98GL51842.

Avallone, A.; Latorre, D.; Serpelloni, E.; Cavaliere, A.; Herrero, A.; Cecere, G.; D'Agostino, N.; D'Ambrosio, C.; Devoti, R.; Giuliani, R.; Mattone, M.; Calcaterra, S.; Gambino, P.; Abruzzese, L.; Cardinale, V.; Castagnozzi, A.; De Luca, G.; Falco, L.; Memmolo, A.; Migliari, F.; Minichiello, F.; Moschillo, R.; Massucci, A.; Zarrili, L.; Selvaggi, G. Coseismic displacement waveforms for the 2016 August 24 M_w 6.0 Amatrice earthquake (central Italy) carried out from High-Rate GPS data. *Ann. Geophys.* **2016**, 59, doi: 10.4401/ag-7275.

Barberio, M. D.; Barbieri, M.; Billi, A.; Doglioni, C.; Petitta, M. Hydrogeochemical changes before and during the 2016 Amatrice-Norcia seismic sequence (central Italy). *Sci. Rep.* **2017**, 7, doi:10.1038/s41598-017-11990-8.

Barchi, M.R.; Alvarez, W.; Shimabukuro, D.H. The Umbria-Marche Apennines as a Double Orogen: observations and hypotheses. *It. J. Geosci.* **2012**, 131, 258–271, doi:10.3301/IJG.2012.17.

Barnichon, J.D. Finite element modelling in structural and petroleum geology. Doctoral dissertation, Universitè de Liege **1998**.

Bath, M.; Duda, S. J. Earthquake volume, fault plane area, seismic energy, strain, deformation and related quantities. *Ann. Geophys.* **1964**, 17, 353–368.

Bath, M. Lateral inhomogeneities in the upper mantle. *Tectonophysics* **1965**, 2, 483–514, doi: 10.1016/0040-1951(65)90003-X.

Bath, M. Earthquake energy and magnitude. *Phys. Chem. Earth* **1966**, 7, 115–165.

Baumont, D., Scotti, O., Courboulex, F. & Melis, N. Complex kinematic rupture of the M_w 5.9, 1999 Athens earthquake as revealed by the joint inversion of regional seismological and SAR data. *Geophys. J. Int.* **2004**, 158, 1078–1087, doi: 10.1111/j.1365-246X.2004.02374.x.

Benioff, H. Earthquakes and rock creep. *Bull. Seism. Soc. Am.* **1951**, 41, 31–62.

Bernard, P.; Briole, P.; Meyer, B.; Lyon-Caen, H.; Gomez, J.M.; Tiberi, C.; Berge, C.; Cattin, R.; Hatzfeld, D.; Lachet, C.; Lebrun, B.; Deschamps, A.; Courboulex, F.; Larroque, C.; Rigo, A.; Massonnet, D.; Papadimitriou, P.; Kassaras, J.; Diagourtas, D.; Makropoulos, K.; Veis, G.; Papazisi, E.; Mitsakaki, C.; Karakostas, V.; Papadimitriou, E.; Papanastassiou, D.; Chouliaras, M.; Stavrakakis, G. The M_s= 6.2, June 15, 1995 Aigion earthquake (Greece): evidence for low angle normal faulting in the Corinth rift. *J. Seism.* **1997**, 1, 131-150, doi: 10.1023/A:1009795618839.

Beroza, G. C.. Near-source modeling of the Loma Prieta earthquake: evidence for heterogeneous slip and implications for earthquake hazard. *Bull. Seism. Soc. Am.* **1991**, 81, 1603–1621.

Bonatti, E.; Ligi, M.; Gasperini, L.; Peyve, A.; Raznitsin, Y. U.; Chen, Y. J. Transform migration and vertical tectonics at the Romanche fracture zone, equatorial Atlantic. *J. Geophys. Res.: Solid Earth* **1994**, 99, 21779-21802, doi: 10.1029/94JB01178.

Boncio, P.; Lavecchia, G.; Milana, G.; Rozzi, B. Seismogenesis in Central Apennines, Italy: An integrated analysis of minor earthquake sequences and structural data in the Amatrice-Campotosto area. *Ann. Geophys.* **2004**, 47, 1723–1742.

Bonini, L.; Toscani, G.; Seno, S. Three-dimensional segmentation and different rupture behavior during the 2012 Emilia seismic sequence (Northern Italy). *Tectonophysics* **2014**, 630, 33–42, doi: 10.1016/j.tecto.2014.05.006.

Bounif, A.; Dorbath, C.; Ayadi, A.; Meghraoui, M.; Beldjoudi, H.; Laouami, N.; Frogneux, M.; Slimani, A.; Alasset, P.J.; Kharroubi, A.; Ousadou, F.; Chikh, M.; Harbi, A.; Larbes, S.; Maouche, S. The 21 May 2003 Zemmouri (Algeria) earthquake M_w 6.8: relocation and aftershock sequence analysis. *Geophys. Res. Lett. 31* **2004**, 31, doi: 10.1029/2004GL020586.

Bullen, K. E.; Bolt, B. A. An Introduction to the Theory of Seismology. New York: Cambridge University Press **1947**.

Carminati, E.; Lustrino, M.; Doglioni, C. Geodynamic evolution of the central and western Mediterranean: Tectonics vs. igneous petrology constraints. *Tectonophysics* **2012**, 579, 173-192, doi:10.1016/j.tecto.2012.01.026.

Carro, M.; De Amicis, M.; Luzi, L. Hydrogeological changes related to the Umbria–Marche earthquake of 26 September 1997 (Central Italy). *Nat. haz.* **2005**, 34, 315-339.

Castaldo, R.; De Novellis, V.; Solaro, G.; Pepe, S.; Tizzani, P.; De Luca, C.; Bonano, M.; Manunta, M.; Casu, F.; Zinno, I.; Lanari, R. Finite element modelling of the 2015 Gorkha earthquake through the joint exploitation of DInSAR measurements and geologic-structural information. *Tectonophysics* **2017**, 714, 125-132, doi: 10.1016/j.tecto.2016.06.037.

Castaldo, R.; de Nardis, R.; DeNovellis, V.; Ferrarini, F.; Lanari, R.; Lavecchia, G.; Pepe, S.; Solaro, G.; Tizzani, P. Coseismic Stress and Strain Field Changes Investigation Through 3-D Finite Element Modeling of DInSAR and GPS Measurements and Geological/Seismological Data: The L'Aquila (Italy) 2009 Earthquake Case Study. *J. Geophys. Res.: Solid Earth* **2018**, 123, 4193–4222, doi: 10.1002/2017JB014453.

Cheloni, D.; D'Agostino, N.; D'Anastasio, E.; Avallone, A.; Mantenuto, S.; Giuliani, R.; Mattone, M.; Calcaterra, S.; Gambino, P.; Dominici, D.; Radicioni, F.; Fastellini, G. Coseismic and initial post-seismic slip of the 2009 M_w 6.3 L'Aquila earthquake, Italy, from GPS measurements. *Geophys. J. Int.* **2010**, 181, 1539–1546, doi: 10.1111/j.1365-246X.2010.04584.x.

Cheloni, D.; Serpelloni, E.; Devoti, R.; D'Agostino, N.; Pietrantonio, G.; Riguzzi, F.; Anzidei, M.; Avallone, A.; Cavaliere, A.; Cecere, G.; D'Ambrosio, C.; Esposito, A.; Falco, L.; Galvani, A.; Selvaggi, G.; Sepe, V.; Calcaterra, S.; Giuliani, R.; Mattone, M.; Gambino, P.; Abruzzese, L.; Cardinale, V.; Castagnozzi, A.; De Luca, G.; Massucci, A.; Memmolo, A.; Migliari, F.; Minichiello, F.; Zarrilli, L. GPS observations of coseismic deformation following the 2016, August 24, Mw 6 Amatrice earthquake (central Italy): Data, analysis and preliminary fault model, *Ann. Geophys.* **2016**, 59, doi:10.4401/ag-7269.

Cheloni, D.; De Novellis, V.; Antonioli, A.; Anzidei, M.; Atzori, S.; Avallone, A.; Bignami, C.; Bonano, M.; Calcaterra, S.; Castaldo, R.; Casu, F.; Cecere, G.; D'Agostino, N.; De Luca, C.; Devoti, R.; Di Bucci, D.; Esposito, A.; Galvani, A.; Gambino, P.; Giuliani, R.; Lanari, R.; Manunta, M.; Manzo, M.; Mattone, M.; Pepe, A.; Pepe, S.; Pezzo, G.; Pietrantonio, G.; Riguzzi, F.; Salvi, S.; Selvaggi, G.; Sepe, V.; Serpelloni, E.; Solaro, G.; Stramondo, S.; Tizzani, P.; Tolomei, C.; Trasatti, E.; Valerio, E.; Zinno, I.; Doglioni, C. Geodetic model of the 2016 Central Italy earthquake sequence inferred from InSAR and GPS data. *Geophys. Res. Lett.* **2017**, 44, 6778–6787, doi:10.1002/2017GL073580.

Chiarabba, C.; Selvaggi, G. Structural control on fault geometry: example of the Grevena M_s 6.6, normal faulting earthquake. *J. Geophys. Res*. **1997**, 102, 22445–22457.

Chiarabba, C.; Jovane, L.; Di Stefano, R. A new view of Italian seismicity using 20 years of instrumental recordings. *Tectonophysics* **2005**, 395, 251–268, doi: 10.1016/j.tecto.2004.09.013.

Chiaraluce, L.; Amato, A.; Cocco, M.; Chiarabba, C.; Selvaggi, G.; Di Bona, M.; Piccinini, D.; Deschamps, A.; Margheriti, L.; Courboulex, F.; Ripepe, M. Complex normal faulting in the Apennines thrust-and-fold belt: The 1997 seismic sequence in central Italy. *Bull. Seism. Soc. Am.* **2004**, 94, 99-116, doi: 10.1785/0120020052.

Chiaraluce, L.; Chiarabba, C.; De Gori, P.; Di Stefano, R.; Improta, L.; Piccinini, D.; Schlagenhauf, A.; Traversa, P.; Valoroso, L.; Voisin, C. The 2009 L'Aquila (Central Italy) Seismic Sequence. *Boll. Geofis. Teor. Appl.* **2010**, 52, 367-387, doi: 10.4430/bgta0019.

Chiaraluce, L.; Valoroso, L.; Piccinini, D.; Di Stefano, R.; De Gori, P. The anatomy of the 2009 L'Aquila norma fault system (central Italy) imaged by high resolution foreshock and aftershock locations. *J. Geophys. Res.* **2011**, 116, B12311, doi:10.1029/2011JB008352.

Chiaraluce, L. Unravelling the complexity of Apenninic extensional fault systems: A review of the 2009 L'Aquila earthquake (Central Apennines, Italy). *J. Struct. Geol.* **2012**, 42, 2-18, doi: 10.1016/j.jsg.2012.06.007.

Chiaraluce, L.; Di Stefano, R.; Tinti, E.; Scognamiglio, L.; Michele, M.; Casarotti, E.; Cattaneo, M.; De Gori, P.; Chiarabba, C.; Monachesi, G.; Lombardi, A.; Valoroso, L.; Latorre, D.; Marzorati, S. The 2016 Central Italy seismic sequence: A first look at the mainshocks, aftershocks and source models. *Seism. Res. Lett.* **2017**, 88, doi:10.1785/0220160221.

Chorowicz, J. The east African rift system. *J. Afr. Earth Sci.* **2005**, 43, 379-410, doi: 10.1016/j.jafrearsci.2005.07.019.

Cinti, F. R.; Pantosti, D.; De Martini, P.M.; Pucci, S.; Civico, R.; Pierdominici, S.; Cucci, L.; Brunori, C. A.; Pinzi, S.; Patera, A. Evidence for surface faulting events along the Paganica fault prior to the 6 April 2009 L'Aquila earthquake (central Italy). *J. Geophys. Res.* **2011**, 116, doi: 10.1029/2010JB007988.

Costantini, M. A novel phase unwrapping method based on network programming. *IEEE Trans. Geosci. Remote Sens.* **1998**, 36, 813-821, doi: 10.1109/36.673674.

Dahlen, F. A. The balance of energy in earthquake faulting. *Geophys. J. R. Astron. Soc.* **1977**, 48, 239–261, doi: 10.1111/j.1365-246X.1977.tb01298.x.

Delouis, B.; Vallée, M.; Meghraoui, M.; Calais, E.; Maouche, S.; Lammali, K.; Mahsas, A.; Briole, P.; Benhamouda, F.; Yelles, K. Slip distribution of the 2003 Boumerdes-Zemmouri earthquake, Algeria, from teleseismic, GPS, and coastal uplift data. *Geophys. Res. Lett.* **2004**, 31, doi: 10.1029/2004GL020687.

Déverchère, J.; Yelles, K.; Domzig, A.; Mercier de Lé pinay, B.; Bouillin, J.P.; Gaullier, V.; Bracène, R.; Calais, E.; Savoye, B.; Kherroubi, A.; Le Roy, P.; Pauc, H.; Dan, G. Active thrust faulting offshore Boumerdes, Algeria, and its relations to the 2003 M_w 6.9 earthquake. *Geophys. Res. Lett.* **2005**, 32, doi: 10.1029/2004GL021646.

Dieterich, J. Modeling of rock friction: 1. Experimental results and constitutive equations. *J. Geophys. Res.* **1979**, 84, 2161–2168, doi: 10.1029/JB084iB05p02161.

Dieterich, J., 1994. A constitutive law for rate of earthquake production and its application to earthquake clustering. *J. Geophys. Res.* **1994**, 99, 2601–2618, doi: 10.1029/93JB02581.

Di Luccio, F.; Ventura, G.; Di Giovambattista, R.; Piscini, A.; Cinti, F.R. Normal faults and thrusts re-activated by deep fluids: the 6 April 2009 M_w 6.3 L'Aquila earthquake, central Italy. *J. Geophys. Res.* **2010**, 115, B06315, 15, doi:10.1029/2009JB007190.

Doglioni, C. A proposal for the kinematic modelling of W-dipping subductions-possible applications to the Tyrrhenian-Apennines system. *Terra Nova* **1991**, 3, 423-434, doi: 10.1111/j.1365-3121.1991.tb00172.x.

Doglioni, C., Barba, S., Carminati, E. & Riguzzi, F. Role of the brittle–ductile transition on fault activation. *Phys. of the Earth Plan. Int.* **2011**, 184, 160–171, doi: doi.org/10.1016/j.pepi.2010.11.005.

Doglioni, C.; Barba, S.; Carminati, E.; Riguzzi, F. Fault on–off versus coseismic fluids reaction. *Geosci. Front.* **2014**, 5, 767–780, doi: 10.1016/j.gsf.2013.08.004.

Doglioni, C.; Carminati, E.; Petricca, P.; Riguzzi, F. Normal fault earthquakes or graviquakes. *Sci. Rep.* **2015a**, 5, doi:10.1038/srep12110.

Doglioni, C., Barba, S., Carminati, E. & Riguzzi, F. Fault on-off versus strain rate and earthquakes energy. *Geosci. Front.* **2015b**, 6, 265–276, doi: 10.1016/j.gsf.2013.12.007.

Dreger, D.S.; Oglesby, D.D.; Harris, R.; Ratchkovski, N.; Hansen, R. Kinematic and dynamic rupture models of the November 3, 2002 M_w 7.9 Denali, Alaska, earthquake. *Geophys. Res. Lett.* **2004**, 31, doi: 10.1029/2003GL018333.

Dziewonski, A. M.; Chou, T. A.; Woodhouse, J. H. Determination of earthquake source parameters from waveform data for studies of global and regional seismicity. *J. Geophys. Res.* **1981**, 86, 2825–2852, doi: 10.1029/JB086iB04p02825.

Ekström, G.; Morelli, A.; Boschi, E.; Dziewonski, A. M. Moment tensor analysis of the central Italy earthquake. *Geophys. Res. Lett.* **1997**, 1971–1974.

Ekström, G.; Nettles, M.; Dziewonski, A.M. The global CMT project 2004–2010: Centroid-moment tensors for 13,017 earthquakes. *Phys. Earth Planet. Inter.* **2012**, 200–201, 1–9, doi: 10.1016/j.pepi.2012.04.002.

Emre, Ö.; Duman, T.Y.; Dogan, A.; Özalp, S.; Tokay, F.; Kuscu, I. Surface faulting associated with the Sultandağı earthquake (M_w 6.5) of 3 February 2002, southwestern Turkey. *Seism. Res. Lett.* **2003**, 74, 382–392.

Ergin, M.; Aktar, M.; Özalaybey, S.; Tapirdamaz, M.C.; Selvi, O.; Tarancioglu, A. A high-resolution aftershock seismicity image of the 2002 Sultandağı-Çay earthquake (M_w=6.2), Turkey. *J. Seism.* **2009**, 13, 633–646, doi: 10.1007/s10950-009-9155-1.

Fagan, M.J. Finite Elements Analysis: Theory and Practice, Prentice Hall., **1992**, 1–311.

Falcucci, E.; Gori, S.; Galadini, F.; Fubelli, G.; Moro, M.; Saroli, M. Active faults in the epicentral and mesoseismal M_l 6.0 24, 2016 Amatrice earthquake region, central Italy. Methodological and seismotectonic issues. *Ann. Geophys.* **2016**, 59, doi:10.4401/ag-7266.

Falcucci, E.; Gori, S.; Bignami, C.; Pietrantonio, G.; Melini, D.; Moro, M.; Saroli, M.; Galadini, F. The Campotosto Seismic Gap in Between the 2009 and 2016–2017 Seismic Sequences of Central Italy and the Role of Inherited Lithospheric Faults in Regional Seismotectonic Settings. *Tectonics* **2018**, 37, doi: 10.1029/2017TC004844.

Fang, L.H.; Wu, J.P.; Wang, W.L.; Lu, Z.Y.; Wang, C.Z.; Yang, T.; Cai, Y. Relocation of the mainshock and aftershock sequences of M_s 7.0 Sichuan Lushan earthquake. *Chin. Sci. Bull.* **2013**, 58, 3451–3459, doi: 10.1007/s11434-013-6000-2.

Feng, G.; Li, Z.; Shan, X.; Zhang, L.; Zhang, G.; Zhu, J. Geodetic model of the 2015 April 25 Mw 7.8 Gorkha Nepal Earthquake and M_w 7.3 aftershock estimated from InSAR and GPS data. *Geophys. J. Int.* **2015**, 203, 896–900, doi: 10.1093/gji/ggv335.

Ferrarini, F.; Lavecchia, G.; de Nardis, R.; Brozzetti, F. Fault Geometry and Active Stress from Earthquakes and Field Geology Data Analysis. The Colfiorito 1997 and L'Aquila 2009 Cases (Central Italy). *Pure Appl. Geophys.* **2015**, 172, 1079–1103, doi: 10.1007/s00024-014-0931-7.

Fialko, Y. Probing the mechanical properties of seismically active crust with space geodesy: Study of the coseismic deformation due to the 1992 M_w 7.3 Landers (southern California) earthquake. *J. Geophys. Res.: Solid Earth* **2004**, 109, doi: 10.1029/2003JB002756. Galadini, F.; Galli, P. Paleoseismology of silent faults in the Central Apennines (Italy): the Mt. Vettore and Laga Mts. Faults. *Ann. Geophys.* **2003**, 46, 815–836.

Fialko, Y. Interseismic strain accumulation and the earthquake potential on the southern San Andreas fault system. *Nature* **2006**, 441, 968-971, doi: 10.1038/nature04797.

Galadini, F.; Falcucci, E.; Gori, S.; Kayen, R.E.; Lingwall, B.; Pizzi, A.; Di Domenica, A.; Zimmaro, P.; Stewart, J.P. Chapter 2: Seismic source and surface rupture, in Engineering Reconnaissance Following the 2016 central Italy earthquakes - Version 2, edited by P. Zimmaro and J. P. Stewart, Geotechnical Extreme Events Reconnaissance Association Report No. GEER-050D **2017**, 33–50, doi:10.18118/G6HS39.

Galli, P.; Galadini, F.; Pantosti, D. Twenty years of paleoseismology in Italy. *Earth Sci. Rev.* **2008**, 88, 89–117, doi: 10.1016/j.earscirev.2008.01.001.

Galvani A.; Anzidei, M.; Devoti, R.; Esposito, A.; Pietrantonio, G.; Pisani, A.R.; Riguzzi, F.; Serpelloni, E. The interseismic velocity field of the central Apennines from a dense GPS network. *Ann. Geophys.* **2012**, 55, doi:10.4401/ag-6168.

Ganas, A.; Pavlides, S.B.; Sboras, S.; Valkaniotis, S.; Papaioannou, S.; Alexandrisb, G.A.; Plessa, A.; Papadopoulos, G.A. Active fault geometry and kinematics in Parnitha Mountain, Attica, Greece. *J. Struct. Geol.* **2004**, 26, 2103–2118, doi: 10.1016/j.jsg.2004.02.015.

Gentili, S.; Di Giovambattista, R. Pattern recognition approach to the subsequent event of damaging earthquakes in Italy. *Phys. Earth Planet. Inter.* **2017**, 266, 1–17, doi: 10.1016/j.pepi.2017.02.011.

Girdler, R.W. The Dead Sea transform fault system. *Tectonophysics* **1990**, 180, 1-13, doi: 10.1016/0040-1951(90)90367-H.

Gomberg, J.; Johnson, P. Seismology: dynamic triggering of earthquakes. *Nature* **2005**, 437, 830, doi: 10.1038/437830a.

Gratier, J. P.; Thouvenot, F.; Jenatton, L.; Tourette, A.; Doan, M. L.; Renard, F. Geological control of the partitioning between seismic and aseismic sliding behaviours in active faults: Evidence from the Western Alps, France. *Tectonophysics* **2013**, 600, 226-242, doi:10.1016/j.tecto.2013.02.013.

Gutenberg, B.; Richter, C. F. Seismicity of the Earth and Associated Phenomena. Princeton: Princeton University Press **1954**.

Hatzfeld, D.; Karakostas, V.; Ziazia, M.; Selvaggi, G.; Leborgne, S.; Berge, C.; Guiguet, R.; Paul, A.; Voidomatis, P.; Diagourtas, D.; Kassaras, I.; Koutsikos, I.; Makropoulos, K.; Azzara, R.; Di Bona, M.; Baccheschi, S.; Bernard, P.; Papaioannou, C. The Kozani-Grevena (Greece) earthquake of 13 May 1995 revisited from a detailed seismological study. *Bull. Seismol. Soc. Am.* **1997**, 87, 463–473.

Hu, Y.; Wang, K.; He, J.; Klotz, J.; Khazaradze, G. Three-dimensional viscoelastic finite element model for postseismic deformation of the great 1960 Chile earthquake. *J. Geophys. Res.: Solid Earth* **2004**, 109, doi: 10.1029/2004JB003163.

Huang, M.H.; Fielding, E.J.; Liang, C.; Milillo, P.; Bekaert, D.; Dreger, D.; Salzer, J. Coseismic deformation and triggered landslides of the M_w 6.2 Amatrice earthquake in Italy. *Geophys. Res. Lett.* **2017**, 44, 1266–1274, doi:10.1002/2016GL071687.

Hubbert, M. K. Theory of scale models as applied to the study of geologic structures. *Bull. Geol. Soc. Am.* **1937**, 48, 1459-1520, doi:10.1130/GSAB-48-1459.

International Seismological Centre, On-line Bulletin, http://www.isc.ac.uk Internatl. Seismol. Cent., Thatcham, United Kingdom, 2014.

Ismail-Zadeh, A.; Tackley, P. Computational methods for geodynamics. Cambridge University Press **2010**.

Jackson, J.A. Active normal faulting and crustal extension. In Continental Extensional Tectonics, eds. M. Coward, J. Dewey, and P. Hancock. London: Blackwell **1997**, 3–18.

Kanamori, H.; Brodsky, E. E. The physics of earthquakes. Reports on Progress in Physics **2004**, 67, 1429-1496, doi: 10.1088/0034-4885/67/8/R03.

Kanamori, H.; Rivera, L. Energy partitioning during an earthquake. In Earthquakes: Radiated Energy and the Physics of Faulting. Geophysical Monograph Series **2006**, 170, 3-13.

Lavecchia, G.; Castaldo, R.; de Nardis, R.; De Novellis, V.; Ferrarini, F.; Pepe, S.; Brozzetti, F.; Solaro, G.; Cirillo, D.; Bonano, M.; Boncio, P.; Casu, F.; De Luca, C.; Lanari, R.; Manunta, M.; Manzo, M.; Pepe, A.; Zinno, I.; Tizzani, P. Ground deformation and source geometry of the 24 August 2016 Amatrice earthquake (Central Italy) investigated through analytical and numerical modeling of DInSAR measurements and structural-geological data. *Geophys. Res. Let.* **2016**, 43, 389–12,398, doi:10.1002/2016GL071723.

Lay, T.; Wallace, T.C. Modern global seismology. Elsevier **1995**.

Leitner, B.; Eberhart-Phillips, D.; Anderson, H.; Nabelek, J. L. A focused look at the Alpine fault, New Zealand: Seismicity, focal mechanisms, and stress observations. *J. Geophys. Res.: Solid Earth* **2001**, 106, 2193-2220, doi: 10.1029/2000JB900303.

Lieber, P.; Braslau, D. On an earthquake and aftershock mechanism relating to a model of the crust and mantle. Report Am-65-8. Office of Research Services, University of California, Berkeley **1965**.

Liu, C.; Zheng, Y.; Ge, C.; Xiong, X.; Hsu, H. Rupture process of the M_s 7.0 Lushan earthquake, 2013. *Sci. China Earth Sci.* **2013** 56, 1187–1192, doi: 10.1007/s11430-013-4639-9.

Liu, C.; Zheng Y.; Xie Z.; Xiong X. Rupture features of the 2016 M_w 6.2 Norcia earthquake and its possible relationship with strong seismic hazards. *Geophys. Res. Lett.* **2017**, 44, 1320–1328, doi:10.1002/2016GL071958.

Louvari, E.; Kiratzi, A. Source parameters of the 7 September 1999 Athens (Greece) earthquake based on teleseismic data. *J. Balkan Geophys. Soc.* **2001**, 4, 51–60.

Mandelbrot, B. B. Fractal geometry: what is it, and what does it do? In Proceedings of the Royal Society of London A: Mathematical, Physical and Engineering Sciences **1989**, 423, 3–16.

Manzo, M.; Ricciardi, G. P.; Casu, F.; Ventura, G.; Zeni, G.; Borgström, S.; Berardino, P.; Del Gaudio, C.; Lanari, R. Surface deformation analysis in the Ischia Island (Italy) based on spaceborne radar interferometry. *J. Volc. Geoth. Res.* **2006**, 151, 399-416, doi:10.1016/j.jvolgeores.2005.09.010.

Massonnet, D.; Rossi, M.; Carmona, C.; Adragna, F.; Peltzer, G.; Feigl, K.; Rabaute, T. The displacement field of the Landers earthquake mapped by radar interferometry. *Nature* **1993**, 364, 138-142, doi: 10.1038/364138a0.

Meghraoui, M.; Maouche, S.; Chemaa, B.; Cakir, Z.; Aoudia, A.; Harbi, A.; Alasset, P.J.; Ayadi, A.; Bouhadad, Y.; Benhamouda, F. Coastal uplift and thrust faulting associated with the M_w=6.8 Zemmouri (Algeria) earthquake of 21 May, 2003. *Geophys. Res. Lett.* **2004**, 31, doi:10.1029/2004GL020466.

Meyer, B.; Armijo, R.; Massonnet, D.; de Chabalier, C.; Delacourt, C.; Ruegg, J.C.; Achache, J.; Briole, P.; Papanastassiou, D. The1995 Grevena (Northern Greece) earthquake: fault model constrained with tectonic observations and SAR interferometry. *Geophys. Res. Lett.* **1996**, 23, 2677-2680.

Miller, S. A.; Collettini, C.; Chiaraluce, L.; Cocco, M.; Barchi, M.; Kaus, B. J. P. Aftershocks driven by a high-pressure CO2 source at depth. *Nature* **2004**, 427, 724–727, doi: 10.1038/nature02251.

Nieuwland, D.A.; Walters, J.V. Geomechanics of the South Furious field. An integrated approach towards solving complex structural geological problems, including analogue and finite-element modelling. *Tectonophysics* **1993**, 226, 143-166, doi:10.1016/0040-1951(93)90115-Z.

Nur, A.; Booker, J. R. Aftershocks caused by pore fluid flow? *Science* **1972**, 175, 885–887, doi: 10.1126/science.175.4024.885.

Omori, F. On the after-shocks of earthquakes (Vol. 7). The University **1894**.

Ozawa, S.; Nishimura, T.; Suito, H.; Kobayashi, T.; Tobita, M.; Imakiire, T. Coseismic and postseismic slip of the 2011 magnitude-9 Tohoku-Oki earthquake. *Nature* **2011**, 475, 373-376, doi: 10.1038/nature10227.

Ozer, N.; Altinok, Y; Ceylan, S. Properties of the aftershocks sequences of the 2000 and 2002 earthquakes in Aksehir-Afyon graben, west-central Anatolia, Turkey. *Nat. Haz.* **2007**, 40, 553–562, doi: 10.1007/s11069-006-9019-8.

Papadimitiou, P.; Voulgaris, N.; Kassaras, I.; Kaviris, G.; Delibasis, N.; Makropoulos, N. The M_w=6.0, 7 September 1999 Athens earthquake. *Nat. Haz.* **2002**, 27, 15–33, doi: 10.1023/A:1019914915693.

Parameswaran, R.M.; Natarajan, T.; Rajendran, K; Rajendran, C.P.; Mallick, R.;Wood, M.; Lekhak, H.C. Seismotectonics of the April–May 2015 Nepal earthquakes: An assessment based on the aftershock patterns, surface effects and deformational characteristics. *J. Asian Earth Sci.* **2015**, 111, 161–174, doi: 10.1016/j.jseaes.2015.07.030.

Parrish, D.K.; Krivz, A.L.; Carter, N.L. Finite-element folds of similar geometry. *Tectonophysics* **1976**, 32, 183-207, doi:10.1016/0040-1951(76)90062-7.

Parsons, T. Global Omori law decay of triggered earthquakes: Large aftershocks outside the classical aftershock zone. *J. Geophys. Res.* **2002**, 107, 2199, doi:10.1029/2001JB000646.

Parsons, T. The basin and range province. In Developments in Geotectonics, Elsevier **2006**.

Pavlides, S.B.; Zouros, N.C.; Chatzipetros, A.A.; Kostopoulos, D.S.; Mountrakis, D.M. The 13 May 1995 western Macedonia, Greece (Kozani Grevena) earthquake; preliminary results. *Terra Nova* **1995**, 7, 544–549, doi: 10.1111/j.1365-3121.1995.tb00556.x.

Petricca, P.; Barba, S.; Carminati, E.; Doglioni, C.; Riguzzi, F. Graviquakes in Italy. *Tectonophysics* **2015**, 656, 202–214, doi:10.1016/j.tecto.2015.07.001.

Pizzi, A.; Di Domenica, A.; Gallovič, F.; Luzi, L.; Puglia, R. Fault segmentation as constraint to the occurrence of the main shocks of the 2016 Central Italy seismic sequence. *Tectonics* **2017**, 36, 2370-2387, doi:10.1002/2017TC004652.

Pondrelli, S.; Salimbeni, S.; Perfetti, P.; Danecek, P. Quick regional centroid moment tensor solutions for the Emilia 2012 (northern Italy) seismic sequence. *Ann. Geophys.* **2012**, 55, doi: 10.4401/ag-6146.

Porreca, M.; Minelli, G.; Ercoli, M.; Brobia, A.; Mancinelli, P.; Cruciani, F.; Giorgetti, C.; Carbomi, F.; Mirabella., F.; Cavinato, G.; Cannata, A.; Pauselli, C.; Barvhi, M.R. Seismic Reflection Profiles and Subsurface Geology of the Area Interested by the 2016–2017 Earthquake Sequence (Central Italy). *Tectonics* **2018**, 37, 1116-1137, doi: 10.1002/2017TC004915.

Prakash, R.; Singh, R. K.; Srivastava, H.N. Nepal earthquake 25 April 2015: source parameters, precursory pattern and hazard assessment. *Geomatics, Natural Hazards and Risk* **2016**, 7, 1769-1784, doi: 10.1080/19475705.2016.1155504.

Press, W.H.; Flannery, B.P.; Teukolsky, S.A.; Vetterling, W.T. Numerical Recipes in C. Cambridge University Press, **1988**.

Quattrocchi, F.; Pik, R.; Pizzino, L.; Guerra, M.; Scarlato, P.; Angelone, M.; Barbieri, M.; Conti, A.; Marty, B.; Sacchi, E.; Zuppi, G.M.; Lombardi, S. Geochemical changes at the Bagni di Triponzo thermal spring during the Umbria-Marche 1997–1998 seismic sequence. *J. Seism.* **2000**, 4, 567-587.

Quigley, M.; Van Dissen, R.; Litchfield, N.; Villamor, P.; Duffy, B.; Barrell, D.; Furlong, K.; Stahl, T.; Bilderback, E.; Noble, D. Surface rupture during the 2010 M_w 7.1 Darfield (Canterbury) earthquake: Implications for fault rupture dynamics and seismic-hazard analysis. *Geology* **2012**, 40, 55-58, doi: 10.1130/G32528.1.

Reilinger, R.E.; Ergintav, S.; Bürgmann, R.; McClusky, S.; Lenk, O.; Barka, A.; Gurkan, O.; Hearn, L.; Feigl, K.L.; Cakmak, R.; Aktug, B.; Ozener, H.; Töksoz, M.N. Coseismic and postseismic fault slip for the 17 August 1999, M=7.5, Izmit, Turkey earthquake. *Science* **2000**, 289, 1519-1524, doi: 10.1126/science.289.5484.1519.

Resor, P.G.; Pollard, D.D.; Wright, T.J.; Beroza, G.C. Integrating high-precision aftershock locations and geodetic observations to model coseismic deformation associated with the 1995 Kozani-Grevena earthquake, Greece. *J. Geophys. Res.* **2005**, 110, doi: 10.1029/2004JB003263.

Richter, C. F. Elementary Seismology. San Francisco: W. H. Freeman **1958**.

Ripepe, M.; Piccinini, D.; Chiaraluce, L. Foreshock sequence of September 26th, 1997 Umbria-Marche earthquakes. *J. Seism.* **2000**, 4, 387–399, doi: 10.1023/A:1026508425230.

Rowland, J.V.; Sibson, R.H. Extensional fault kinematics within the Taupo Volcanic Zone, New Zealand: soft-linked segmentation of a continental rift system. *New Zealand J. Geol. Geophys.* **2001**, 44, 271-283, doi: 10.1080/00288306.2001.9514938.

Ruff, L.; Kanamori, H. Seismicity and the subduction process. *Phys. Earth Plan. Int.* **1980**, 23, 240-252, doi: 10.1016/0031-9201(80)90117-X.

Ruina, A. Slip instability and state variable friction laws. *J. Geophys. Res.* **1983**, 88, 10359–10370, doi: 10.1029/JB088iB12p10359.

Ryan, W. B. F. et al. Global Multi-Resolution Topography synthesis. *Geochem. Geophys. Geosyst.* **2009**, 10, Q03014, https://doi. org/10.1029/2008GC002332.

Savage, J. C. A dislocation model of strain accumulation and release at a subduction zone. *J. Geophys. Res.* **1983**, 88, 4984–4996, doi: 10.1029/JB088iB06p04984.

Savage, J. C. A dislocation model of strain accumulation and release at a subduction zone. *J. Geophys. Res.* **1983**, 88, 4984–4996, doi: 10.1029/JB088iB06p04984.

Scholz, C. H. The mechanics of earthquakes and faulting. Cambridge university press **2002**.

Schön, J. H. Physical properties of rocks: Fundamentals and principles of petrophysics. Elsevier **2015**, 65.

Schorlemmer, D.; Wiemer, S.; Wyss, M. Variations in earthquake-size distribution across different stress regimes. *Nature* **2005**, 437, 539–542, doi: 10.1038/nature04094.

Scognamiglio L.; Tinti E.; Casarotti E.; Pucci S.; Villani F.; Cocco M.; Magnoni F.; Michelini A.; Dreger D. Complex fault geometry and rupture dynamics of the M_w 6.5, 2016, October 30th central Italy earthquake. *J. Geophys. Res. Solid Earth* **2018**, doi: 10.1002/2018JB015603.

Scrocca, D.; Carminati, E.; Doglioni, C.; Marcantoni, D. Slab retreat and active shortening along the central-northern Apennines. *Thrust Belts and Foreland Basins* **2007**, 471–487.

Şengör, A.M.C.; Tüysüz, O.; Imren, C.; Sakınç, M.; Eyidoğan, H.; Görür, N.; Le Pichon, X.; Rangin, C. The North Anatolian fault: A new look. *Annu. Rev. Earth Planet. Sci.* **2005**, 33, 37-112, doi: 10.1146/annurev.earth.32.101802.120415.

Shaw, B. E. Generalized Omori law for aftershocks and foreshocks from a simple dynamics. *Geophys. Res. Lett.* **1993**, 20, 907–910, doi: 10.1029/93GL01058.

Shcherbakov, R.; Turcotte, D.L.; Rundle, J. B. A generalized Omori's law for earthquake aftershock decay. *Geophys. Res. Lett.* **2004**, 31, doi: 10.1029/2004GL019808.

Shearer, P. M. Introduction to seismology. Cambridge University Press **2009**.

Sibuet, J.C.; Hsu, S.K. Geodynamics of the Taiwan arc-arc collision. *Tectonophysics* **1997**, 274, 221-251, doi: 10.1016/S0040-1951(96)00305-8.

Simpson, G. Practical Finite Element Modeling in Earth Science Using Matlab. John Wiley & Sons **2017**.

Smeraglia, L.; Billi, A.; Carminati, E.; Cavallo, A.; Doglioni, C. Field-to nano-scale evidence for weakening mechanisms along the fault of the 2016 Amatrice and Norcia earthquakes, Italy. *Tectonophysics* **2017**, 712–713, 156-169, doi:10.1016/j.tecto.2017.05.014.

Smith, W. H. F.; Wessel, P. Gridding with continuous curvature splines in tension. *Geophysics* **1990**, 55, 293-305, doi:10.1190/1.1442837.

Stein, R. S. The role of stress transfer in earthquake occurrence. *Nature* **1999**, 402, 605–609, doi: 10.1038/45144.

Stein, S.; Okal, E.A. Seismology: Speed and size of the Sumatra earthquake. *Nature* **2005**, 434, 581-582, doi: 10.1038/434581a.

Stein, S.; Liu, M. Long aftershock sequences within continents and implications for earthquake hazard assessment. Nature 2009, 462, 87–89, doi: 10.1038/nature08502.

Stein, S.; Wysession, M. An introduction to seismology, earthquakes, and earth structure. John Wiley & Sons **2009**.

Sugan, M.; Kato, A.; Miyake, H.; Nakagawa, S.; Vuan, A. The preparatory phase of the 2009 M_w 6.3 L'Aquila earthquake by improving the detection capability of low-magnitude foreshocks. *Geophys. Res. Lett.* **2014**, 41, 6137-6144, doi: 10.1002/2014GL061199.

Tarantola, A. Inverse Problem Theory and Methods for Model Parameter Estimation, SIAM Society for Industrial and Applied Mathematics, Philadelphia, **2005**, ISBN 0-89871-572-5.

Taylor, B.; Weiss, J.R.; Goodliffe, A.M.; Sachpazi, M.; Laigle, M.; Hirn, A. The structures, stratigraphy and evolution of the Gulf of Corinth rift, Greece. Geophys. J. Int. 2011, 185, 1189-1219, doi: 10.1111/j.1365-246X.2011.05014.x.

Terakawa, T.; Zoporowski, A.; Galvan, B.; Miller, S.A. High-pressure fluid at hypocentral depths in the L'Aquila region inferred from earthquake focal mechanisms. *Geology* **2010**, 38, 995-998, doi:10.1130/G31457.1.

Tesei, T.; Collettini, C.; Barchi, M. R.; Carpenter, B. M.; Di Stefano, G. Heterogeneous strength and fault zone complexity of carbonate-bearing thrusts with possible implications for seismicity. *Earth Plan. Sci. Lett.* **2014**, 408, 307-318, doi: 10.1016/j.epsl.2014.10.021.

Thompson, G. A.; Parsons, T. Vertical deformation associated with normal fault systems evolved over coseismic, postseismic, and multiseismic periods. *J. Geophys. Res. Solid Earth* **2016**, 121, 2153-2173, doi: 10.1002/2015JB012240.

Thompson, G. A.; Parsons, T. From coseismic offsets to fault-block mountains. *Proceed. Nat. Acad. Sci.* **2017**, 114, 9820-9825, doi: 10.1073/pnas.1711203114.

Tizzani, P.; Castaldo, R.; Solaro, G.; Pepe, S.; Bonano, M.; Casu, F.; Manunta, M.; Manzo, M.; Pepe, A.; Samsonov, S.; Lanari, R.; Sansosti, E. New insights into the 2012 Emilia (Italy) seismic sequence through advanced numerical modeling of ground deformation InSAR measurements. *Geophys. Res. Lett.* **2013**, 40, 1971-1977, doi: 10.1002/grl.50290.

Tselentis, G. A.; Zahradnik, J. The Athens earthquake of 7 September 1999. *Bull. Seismol. Soc. Am.* **2000**, 90, 1143–1160, doi: 10.1785/0119990168.

Turcotte, D. L. Fractals and fragmentation. *J. Geophys. Res.* **1986**, 91, 1921–1926.

Turcotte, D. L. Fractals and chaos in geology and geophysics. Cambridge university press **1997**.

Turcotte, D.; Schubert, G. Geodynamics. Cambridge University Press **2014**.

Utsu, T. A statistical study of the occurrence of aftershocks. *Geophys. Magazine* **1961**, 30, 521–605.

Utsu, T.; Ogata, Y. The centenary of the Omori formula for a decay law of aftershock activity. *J. Phys. Earth* **1995**, 43, 1–33.

Uyeda, S., & Kanamori, H. Back-arc opening and the mode of subduction. *J. Geophys. Res.: Solid Earth* **1979**, 84, 1049-1061, doi: 10.1029/JB084iB03p01049.

Valerio, E.; Tizzani, P.; Carminati, E.; Doglioni, C. Longer aftershocks duration in extensional tectonic settings. *Sci. Rep.* **2017**, 7, doi: 10.1038/s41598-017-14550-2.

Valerio, E.; Tizzani, P.; Carminati, E.; Doglioni, C.; Pepe, S.; Petricca, P.; De Luca, C.; Bignami, C.; Solaro, G.; Castaldo, R.; De Novellis, V.; Lanari, R. Ground deformation and source geometry of the 30 October 2016 Mw 6.5 Norcia earthquake (Central Italy) investigated through seismological data, DInSAR measurements and numerical modelling. *Remote Sens.* **2018**, 10, doi: 10.3390/rs10121901.

Valoroso, L.; Chiaraluce, L.; Piccinini, D.; Di Stefano, R.; Schaff, D.; Waldhauser, F. Radiography of a normal fault system by 64,000 high-precision earthquake locations: The 2009 L'Aquila (central Italy) case study. *J. Geophys. Res. Solid Earth* **2013**, 118, 1156-1176, doi:10.1002/jgrb.50130.

Velleman, D. J. The generalized Simpson's rule. The American Mathematical Monthly **2005**, 112, 342-350.

Wedmore, L. N. J.; Faure Walker, J. P.; Roberts, G. P.; Sammonds, P. R.; McCaffrey, K. J. W.; Cowie, P.A. A 667 year record of coseismic and interseismic Coulomb stress changes in central Italy reveals the role of fault interaction in controlling irregular earthquake recurrence intervals. *J. Geophys. Res. Solid Earth* **2017**, 122, 5691–5711, doi:10.1002/2017JB014054.

Wessel, P.; Smith, W. H. F.; Scharroo, R.; Luis, J. F.; Wobbe, F. Generic Mapping Tools: Improved version released. *EOS Trans. AGU* **2013**, 94, 409-410, doi:10.1002/2013EO450001.

Wiemer, S. A software package to analyze seismicity: ZMAP. *Seism. Res. Lett.* **2001**, 72, 373-382, doi: 10.1785/gssrl.72.3.373.

Xu, X.W.; Wen, X.Z.; Ye, J.Q. The M_s 8.0 Wenchuan earthquake surface ruptures and its seismogenic structure. *Seism. Geology* **2008**, 30, 597–629.

Xu, G.; Xu, C.; Wen, Y.; Jiang, G. Source Parameters of the 2016–2017 Central Italy Earthquake Sequence from the Sentinel-1, ALOS-2 and GPS Data. *Rem. Sens.* **2017**, 9, doi:10.3390/rs9111182.

Yin, A.; Harrison, T.M. Geologic evolution of the Himalayan-Tibetan orogen. *Ann. Rev. Earth Plan. Sci.* **2000**, 28, 211-280, doi: 10.1146/annurev.earth.28.1.211.

Zhang, Y.; Feng, W.; Xu, L.; Zhou, C.; Chen, Y. Spatio-temporal rupture process of the 2008 great Wenchuan earthquake. *Sci. China Series* **2009**, 52, 145–154, doi: 10.1007/s11430-008-0148-7.

Zhang, P.Z.; Wen, X.Z.; Shen, Z.K.; Chen, J.H. Oblique, high-angle, listric-reverse faulting and associated development of strain: The Wenchuan earthquake of May 12, 2008, Sichuan, China. *Ann. Rev. Earth Plan. Sci.* **2010**, 38, 353–382, doi: 10.1146/annurev-earth-040809-152602.

Zhao, D.; Lei, J.; Inoue, T.; Yamada, A.; Gao, S.S. Deep structure and origin of the Baikal rift zone. *Earth Plan. Sci. Lett.* **2006**, 243, 681-691, doi: 10.1016/j.epsl.2.

Acknowledgements

Vorrei ringraziare i miei tutor, il Prof. Carlo Doglioni e il Prof. Carminati, per avermi seguita durante questi tre anni di dottorato e per avermi permesso di scoprire il mondo della ricerca e le sue bellezze.

Vorrei ringraziare tutti i ricercatori dell'Istituto per il Rilevamento Elettromagnetico dell'Ambiente di Napoli per avermi fatta sentire a casa fin dal primo giorno. Un ringraziamento speciale va al Direttore dell'IREA Ing. Riccardo Lanari per il tempo dedicatomi e per aver mostrato sempre fiducia nelle mie capacità. Inoltre, un ringraziamento molto sentito va al Dott. Pietro Tizzani, al Dott. Raffaele Castaldo, al Dott. Vincenzo De Novellis, alla Dott.ssa Susi Pepe, al Dott. Giuseppe Solaro e al Dott. Claudio De Luca per avermi accompagnata in questo percorso scientifico, per avermi sostenuta moralmente e per non aver mai fatto mancare un sorriso anche nelle giornate più estenuanti.

Ringrazio anche i revisori della tesi, il Dott. Marco Moro e l'Ing. Riccardo Lanari, per i preziosi consigli e suggerimenti.

Un ringraziamento va al Dott. Marco Cuffaro e al Dott. Patrizio Petricca per il loro interessamento alle mie attività di ricerca.

Un ringraziamento speciale va ad Eleonora, non solo una collega di dottorato ma anche una cara amica.

Vorrei ringraziare tutti i miei amici con i quali ho iniziato ben otto fa questo percorso all'insegna della scoperta delle bellezze della Terra: grazie a Danilo, Roberta, Stefano ed Eugenio.

Un ringraziamento molto sentito va ai miei genitori: mi avete insegnato cos'è la vita e come affrontarla in ogni momento, non mi avete mai fatta sentire sola e non c'è stato giorno in cui non mi avete dimostrato il vostro amore.

Un ringraziamento immenso va ad Enzo, che ha stravolto la mia vita con il suo amore, il suo entusiasmo e la sua allegria. Non mi hai mai fatto mancare il tuo sostegno, neanche quando ne avresti avuto più bisogno tu. Sei un punto di riferimento e so di poter sempre contare su di te.

Questo dottorato di ricerca mi ha dato conferma che niente è impossibile e che con tanta forza di volontà e tanta passione si possono raggiungere tutti gli obiettivi che ci poniamo, anche quelli che all'inizio possono sembrare più difficili. Per questo, alla fine di questo percorso, voglio ringraziare me stessa, per non aver mai fatto mancare entusiasmo e forza di volontà, per non essermi arresa di fronte ad ostacoli che mi sembravano insormontabili e per aver creduto fino alla fine che potevo farcela.

Emanuela